DATA DRIVEN TECHNIQUES FOR MODELING COUPLED DYNAMICS IN TRANSIENT PROCESSES

A Dissertation

by

HOANG MINH TRAN

Submitted to the Office of Graduate and Professional Studies of
Texas A&M University
in partial fulfillment of the requirements for the degree of

DOCTOR OF PHILOSOPHY

Chair of Committee,	Satish T.S. Bukkapatnam
Committee Members,	Yu Ding
	Sergiy Butenko
	Jianhua Huang
Head of Department,	Mark Lawley

August 2017

Major Subject: Industrial Engineering

ABSTRACT

We study the problem of modeling coupled dynamics in transient processes that happen in a network. The problem is considered at two levels. At the node level, the coupling between underlying sub-processes of a node in a network is considered. At the network level, the direct influence among the nodes is considered. After the model is constructed, we develop a network-based approach for change detection in high dimension transient processes. The overall contribution of our work is a more accurate model to describe the underlying transient dynamics either for each individual node or for the whole network and a new statistic for change detection in multi-dimensional time series. Specifically, at the node level, we developed a model to represent the coupled dynamics between the two processes. We provide closed form formulas on the conditions for the existence of periodic trajectory and the stability of solutions. Numerical studies suggest that our model can capture the nonlinear characteristics of empirical data while reducing computation time by about 25% on average, compared to a benchmark modeling approach. In the last two problems, we provide a closed form formula for the bound in the sparse regression formulation, which helps to reduce the effort of trial and error to find an appropriate bound. Compared to other benchmark methods in inferring network structure from time series, our method reduces inference error by up to 5 orders of magnitudes and maintain better sparsity. We also develop a new method to infer dynamic network structure from a single time series. This method is the basis for introducing a new spectral graph statistic for change detection. This statistic can detect changes in simulation scenario with modified area under curve (mAUC) of 0.96. When applying to the problem of detecting seizure from EEG signal, our statistic can capture the physiology of the process while maintaining a detection rate of 40% by itself. Therefore, it can serve as an effective feature to detect

change and can be added to the current set of features for detecting seizures from EEG signal.

DEDICATION

To my mum and dad

ACKNOWLEDGMENTS

I acknowledge my advisor, Dr. Satish Bukkapatnam, for the guidance, support and encouragement he has provided. This dissertation would not have been possible without his support. I remain deeply indebted to him.

I also thank my committee members, Dr. Yu Ding, Dr. Sergiy Butenko and Dr. Jianhua Huang. All of you have devoted valuable time to give me support and advice in writing this dissertation and developing my career.

I acknowlege my past and current lab mates and friends at Texas A&M and Oklahoma State University.

Last but not least, I owe my deepest gratitude to my family. My sincere thanks goes to my wife, my sisters and brothers in-law for constant support and encouragement. I thank my mum and dad for unconditional love, and always being my greatest source of strength and inspiration.

CONTRIBUTORS AND FUNDING SOURCES

Contributors

This work was supervised by a dissertation committee consisting of Professor Satish Bukkapatnam [advisor] of the Department of Industrial and Systems Engineering.

The algorithm for change detection in chapter 4 was implemented by Mridul Garg of the Department of Industrial and Systems Engineering.

All other work conducted for the thesis (or) dissertation was completed by the student independently.

Funding sources

This graduate study was supported by National Science Foundation grants CMMI - 1432914, IIP - 1355765, ECCS - 1547075, CMMI - 1538501, and the Graduate Teaching fellowship from Texas A&M University.

NOMENCLATURE

$-\alpha_3$	Maximum relaxing velocity of the recovery process
$-K_2$	Maximum effective degradation rate
$-K_3$	Maximum relaxation acceleration of the recovery process
α_1	Maximum working performance of the machine
α_2	Minimum working performance of the machine
α_4	The machine condition at which the recovery effort is relaxed
α_5	The machine condition at which the recovery effort is started
α_6	Maximum velocity the recovery process
β	Machine degradation condition
$\boldsymbol{g}_i$	column i of matrix G^T
$\boldsymbol{s}_i$	column i of matrix S^T
$\boldsymbol{s}_i^{(K)}$	a vector formed by taking K highest magnitude coefficients of $\boldsymbol{s}_i^0$
$\boldsymbol{s}_i^*$	solution of the l_1-min problem
ΔG	noise/approximation error incurred when estimate G^0 from data
ΔS	error when computing S^0 from G
δ_K	the restricted isometry constant [1] of a matrix Φ, the smallest number such that $(1-\delta_K)\left\|\boldsymbol{x}\right\|_2^2 \leq \left\|\Phi\boldsymbol{x}\right\|_2^2 \leq (1+\delta_K)\left\|\boldsymbol{x}\right\|_2^2$, for all vector $\boldsymbol{x}$ that has at most K nonzero coordinates

$\|S\|_1$ sum of absolute values of all elements of S

$\|Y\|_2$ spectral norm of matrix Y

$\|Y\|_2^{(K)}$ maximal spectral norm of all K - column sub-matrices of Y

$\mathbb{T}_{block}^k$ Set of machine blocking times

$\mathbb{T}_{repair}^k$ Set of machine breakdown and repair times

$\mathbb{T}_{starve}^k$ Set of machine starving times

$\mu_k(t)$ Processing rate during uptime of machine k

ν Perturbation parameter

Φ $= G^T + I$

Φ^0 $= (G^0)^T + I$

ρ Restoration effort

$\varepsilon_{\Phi^0}^{(K)}$ smallest number that is greater than $\frac{\|\Delta G\|_2^{(K)}}{\|\Phi^0\|_2^{(K)}}$

ε_i general constraint bound of l_1-min problem in vector form for computing row i of S

$\varepsilon_i^{(0)}$ bound of the l_1-min problem in vector form for computing row i of S^0, assume S^0 is given

$\varepsilon_i^{(1)}$ bound of the l_1-min problem in vector form for computing row i of S^0, using our formula

G observed total influence matrix

G^0 total influence matrix in noiseless condition

I identity matrix

K_1 Maximum effective recovery rate

K_4 Maximum acceleration of the recovery process

L_k, L_k^{max} Instantaneous and maximum buffer inventory level of machine k

S^0 Direct influence matrix in noiseless condition

u_k Throughput/processing velocity of machine k

HistTBF Histograms of TBF from the model

HistTBFa Histograms of TBF from the actual data

HistTTR Histograms of TTR from the model

HistTTRa Histograms of TTR from the actual data

TABLE OF CONTENTS

Page

LIST OF FIGURES

LIST OF TABLES

1. INTRODUCTION

1.1 Dynamics of complex systems and coupled dynamic modeling challenges

Real-world systems exhibit coupled dynamics. On large-scale, a process is directed by other processes. On small-scale, a process is directed by many subprocesses, such as regeneration and regeneration [3–5]. The coupled dynamics exists if the states of a process and a subprocess affect the time-evolution of the others.

As the structure of the interconnection in a system defines its dynamics [6], the dynamic of a system could not be understood by superposing the decoupled dynamics of the individuals or subsets of state variables [7]. To understand the evolution of such systems, it is necessary to identify the existence or absence of a direct dynamic coupling among the subsystems and among the involving sub-processes. This problem has been noted to be a standing challenge of modern science [8] due to the following issues:

- **High dimensionality**: Real-world system such as a human brain contains millions of neurons [9], thus require up to millions of variables to represent the system dynamics, causing computational issues.

- **Interconnectivity:** Most real-world systems exist in complicated interconnected structures. In brain network, for example, each neuron has on average 7,000 synaptic connections to other neurons, and the number of connections in the brain of a three-year-old child is about 10^{15} [9].

- **Transience:** The structure of interconnectivity and the strength of couplings vary over time, i.e., the coupling among the system state variables are not constant. In general, it is associated with the transient property of a process. As an illustration, the structure of a human brain network depends on the stage of human body. Ac-

cording to [10], brain connectivity is strong during resting wakefulness, decreases during stage N2 of NREM sleep, further decreases during stage N3 of NREM sleep and possible increases during REM sleep.

- **Nonlinear dynamics:** The value of a state variable depends nonlinearly on the values of other state variables [11]. For example, in brain network, the response of a given neuron to presynaptic input from a second neuron depends on multiplicative interactions among the synaptic inputs from other neurons. This type of modulation mechanism raises issues of how to define couplings locally in the state space, and compactly captures the underlying relationships [12, 13].

Finding coupling structure in real world system is an important problem because solutions to this problem are the foundation for other research. The temporal underlying coupling structure if employed will improve available approaches for high dimension time series analysis. The coupling structure might also help to find a better diagnostic strategy for real-world applications such as detecting abnormalies in manufacturing and disease onset detection in human health or developing effective system control mechanisms to maintain desired system trajectory.

In this dissertation, the problem of modeling the coupled dynamics in transient process is considered in the following perspectives (Fig. 1.1):

- At node level: modeling the coupled dynamics between underlying sub-processes of a node in a network. The method is applied to model the dynamics of a manufacturing machine.

- At network level: modeling the direct influence among the nodes. For illustration, we consider apply the method to infer genetic regulatory network from gene expression data.

- Application of the inferred direct influence network in the problem of change detection. To solve this problem, we develop a spectral graph and apply it to detect seizure using EEG signals.

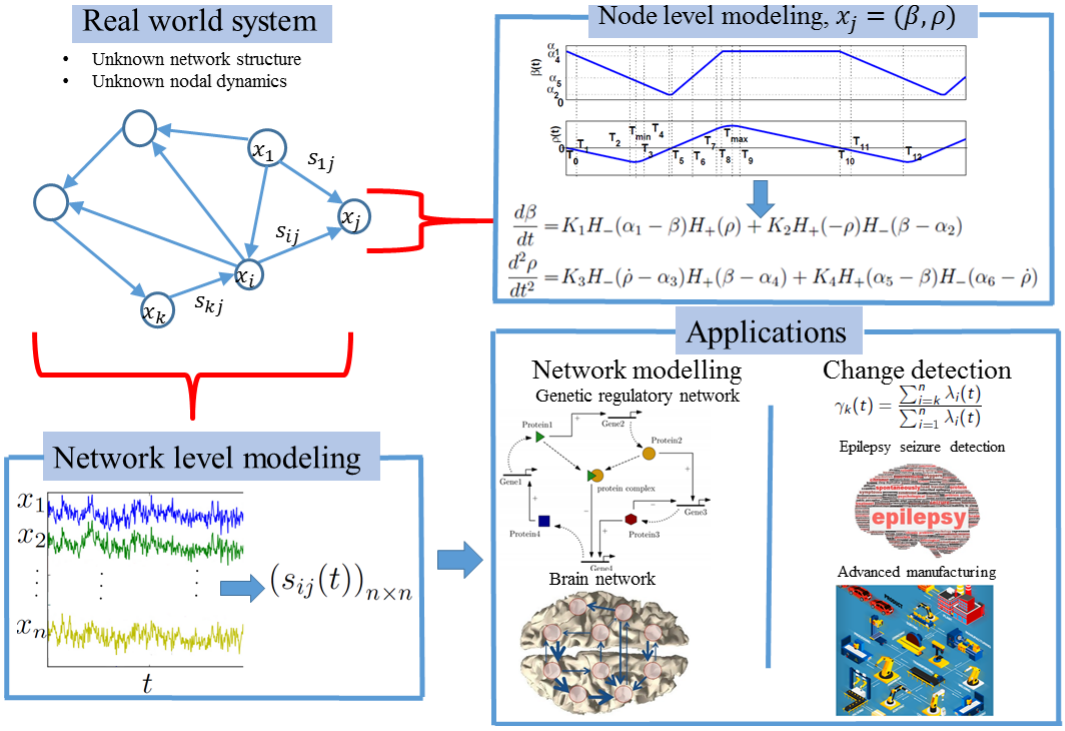

Figure 1.1: Overall framework

1.2 Research Objectives

This study addresses the following three problems:

Problem 1. Modeling the coupled dynamics at the node/subsystem level: modeling the coupled dynamics between underlying sub-processes. For application, we considered modeling the coupled dynamics of degradation and repair processes. We also found the constraints on system parameters to guarantee the system trajectory exhibits expected be-

havior such as periodic orbit and stability. Finally, the model was estimated using data on time between failures and time to repair

Problem 2. Modeling coupled dynamics at the network/system level: developing a network to model the interaction between identities based on their transient time series data. This problem was formulated as an ℓ_1-min problem. Our main contributions were an analytical form for the bounds on the parameters, an averaging procedure, and a perturbation procedure to improve estimation accuracy.

Problem 3. Developing a spectral graph statistic for detecting change in multivariate time series. In this problem, the method developed in problem 2 was extended to apply to the case when only one transient time series is available. The inferred network structure was employed to propose a change detection statistic.

1.3 Organization of Dissertation

The remainder of this dissertation was organized as follows. Section 2 described the first problem: modeling the coupled dynamics on small-scale which involves two processes degeneration and regeneration. Here, we introduced a method to build a model in form of stochastic piecewise differential equations for the breakdown and repair processes of a manufacturing machine using the time between failures and time to repair. We also proposed closed form formulas on system parameters for the stability and existence of periodic solution, an expected behavior of manufacturing machines. Numerical study on estimating system parameters from the observed time between failures and time to repair shows that compared to exponential model, our method is faster while achieving better prediction accuracy.

Section 3 described the second problem: inferring dynamic network model from multivariate transient time series. We proposed a closed form formula for the sparse regression

model for inferring network structure. We tested the method on both simulation data and three benchmark empirical data sets on gene expression.

Section 4 described the third problem: detecting changes in transient complex systems via dynamic network inference. In this section, we introduced a new method to infer direct influence network structure from single multivariate time series. Then we formulated a spectral statistic to detect change in system dynamic based on the inferred network structure. We also provided results on the distribution of the statistic. Numerical simulation on data generated from a picewise linear system and empirical study on EEG signals shows that our statistic can detect the changes while capturing the physiology of the underlying process.

Section 5 summarized our findings and suggests future research directions.

2. COUPLED DYNAMICS MODELING AT NODE LEVEL: MODELING AND ANALYSIS OF THE COUPLED DYNAMICS OF MACHINE DEGRADATION AND REPAIR PROCESSES USING PIECEWISE AFFINE STOCHASTIC DIFFERENTIAL EQUATIONS[1]

In this chapter, we presented that the model with at most cubic constraint set on the parameters can yield (steady state) periodic solutions that can mimic a source of large time-scale breakdown and repair (equivalently, large TBF and TTR) processes (see Theorem 1 in Section 2.2), and closed form expressions for such large time-scale TBF and TTR can be derived in terms of the model parameters (see Theorem 2 in Section 2.2). This ability to capture dynamic behaviors allows the nature of the couplings between TTR and TBF to be quantified. Short time-scale, frequent breakdown and repair processes can be captured by introducing a class of stochastic extension (see Theorem 6) to model parameters. We also investigate the local stability and the basin of attraction of these periodic orbits (Theorems 3-5). The theoretical results are validated using real-world data sets on TBF and TTR acquired from an automotive manufacturing assembly line [14]. The result suggested that the model can capture certain dynamical aspects of empirical data.

2.1 System description and problem formulation

The dynamic system considered for the present investigation is an assembly line segment from a leading automotive manufacturer. It consisted of 18 stations of which 16 are located in tandem. One pair of stations is located in a parallel arrangement in the assembly line. This system is a type of simple N-stage manufacturing system and is de-

[1]Reprinted with permission from "Modeling and analysis of the coupled dynamics of machine degradation and repair processes using piecewise affine stochastic differential equaitons" by Tran, Hoang M and Bukkapatnam, Satish TS, 2015, *International Journal of Non-Linear Mechanics* 76, pp 87-99, Copyright [2015] by Elsevier.

scribed as follows. First, the change in the length of the buffer at the downstream of the k^{th} machine/operation is given by $dL_k/dt = u_{k-1}(t)$–$u_k(t)$ where $u_k(t)$ is the throughput velocity of machine k and L_k is the buffer inventory level at time t. Conventionally, $u_k(t)$ is modeled using random processes $\mu_k(t)$ and $\nu_k(t)$ as

$$u_k(t) = \mu_k(t) - \nu_k(t)$$

where $\mu_k(t)$ is the processing rate (during the up time), $\nu_k(t)$ is the throughput rate loss due to degradation/ breakdown and, typically, $u_k(t) = 0$ during downtime. Downtime in many manufacturing system operations may be attributed to the following three causes:

1. Machine breakdown and repair that takes place during times $t \in \mathbb{T}^k_{repair}$,
2. Starving (upstream buffer is empty) that takes place during times $t \in \mathbb{T}^k_{starve}$ and/or
3. Blocking (downstream buffer is full) that takes place during times $t \in \mathbb{T}^k_{block}$, i.e.,

$$u_k(t) = 0 \text{ if } (L_k(t) = 0 \text{ or } L_{k+1} = L^{\max}_{k+1} \text{ or } t \in \mathbb{T}^k_{repair})$$

Our problem of interest is to model the operational dynamics of the status of each single machine. This model is then integrated to the whole assembly line described above to analyze the whole system. For a single manufacturing machine, there are two underlying processes involve. The first process, the degradation process, in most of the automated assembly systems manifests as long time-scale, fairly regular process (occurring as a result of repeated, "cyclic" loading), as well as short time-scale degradations that occur in components that have steep degradation and restoration rates (short degradation and restoration cycles, such as human attention span, and component misfeeds). The second process, the restoration process, can also be decomposed into a deterministic trend of regular check

up or maintenance and random process involving factors such as irregular fixing when random breakdown occurs. We noted that the deterministic breakdown and maintenance often take much longer TBF and TTR than the random ones.

2.2 Deterministic model for coupled dynamics between degradation and restoration processes of a manufacturing machine

2.2.1 Model description

To build the model for a single machine, we look at a sample path as shown in Fig. 2.1, which captures a representative long time-scale degradation-repair cycles of a manufacturing machine. Here, the restoration rate $\dot{\rho}$ to improve the machine fluctuates around a "nominal" baseline which specifies an average effort (e.g., workforce size) employed for restoration. For simplicity of manipulation and without loss of generality, we choose that "nominal" baseline for $\dot{\rho}$ to be 0 and adjust cumulative restoration ρ as a fluctuation about the linear trend determined by this average. The physical connotation of negative ρ and $\dot{\rho}$ is that their values before adjustment are below the "nominal" baseline linear trend and that set level. The downtime due to machine breakdowns is simulated as resulting from a dynamic interplay between the machine degradation condition β and the cumulative restoration. We note that a degradation process is often attributed to certain natural laws that have been commonly modeled as piecewise constant rate processes [15]. Real-world repair processes tend to be governed by several human-machine-interaction considerations [16–20]. For instance, as the condition starts to deteriorate, some attention and resources are expended towards maintaining and repairing the machine. The efforts are significantly ramped up as the machine condition deteriorates further and are phased out as the machine is restored (see Fig. 2.1). Specifically, upon restoration of machine condition to $\beta(t) = \alpha_1$ at $t = T_0$, where the machine condition is considered to have reached its peak level, the machine gradually degrades at a constant rate of K_2. As the

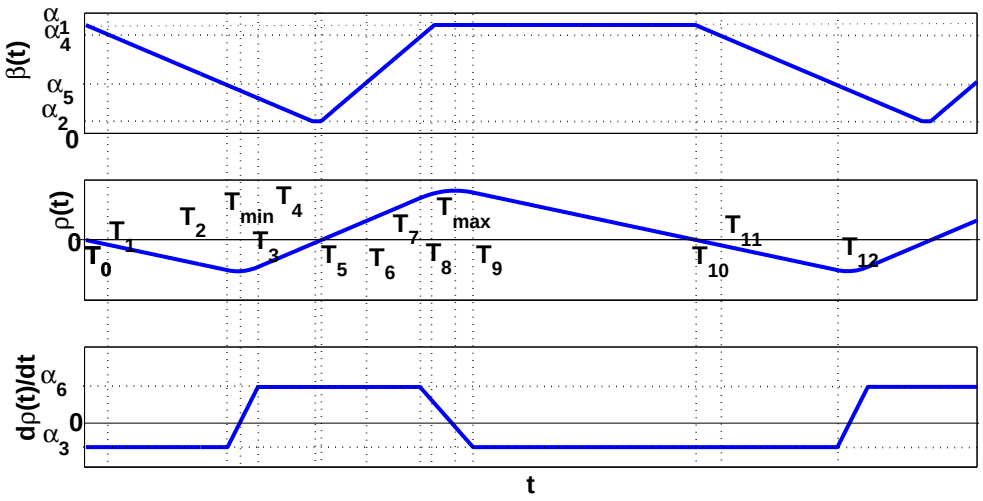

(a)

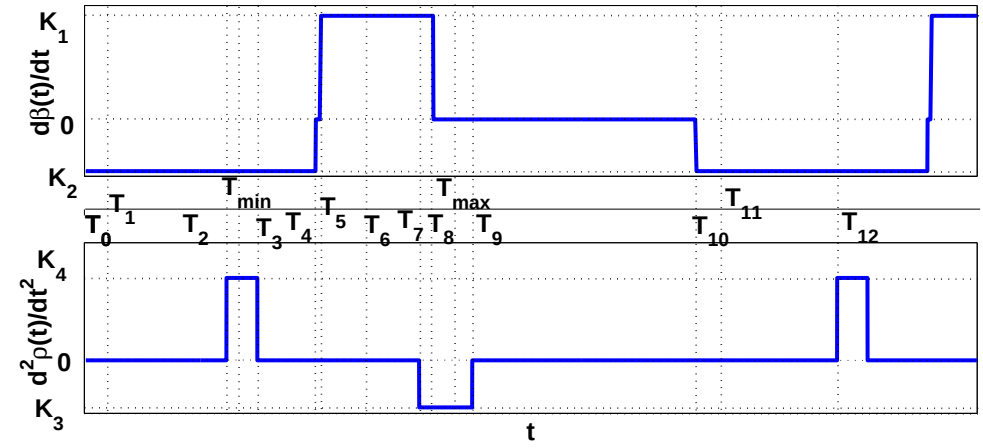

(b)

Figure 2.1: Illustrative diagram of degradation and restoration variable dynamics

condition degrades to $\beta(t) = \alpha_5$ at $t = T_2$, the restoration rate increases. When $t < T_4$, the restoration is not enough to overcome the natural degradation effects, therefore the machine condition continues to decrease and bottoms out to $\beta(t) = \alpha_2$. Thereafter, the machine condition starts to improve gradually at a rate of K_1 at $t = T_5$. The restoration rate reaches the maximum level $\dot{\rho}(t) = \alpha_6$ at $t = T_3$ and retains this value until the machine condition improves to α_4 at $t = T_7$. At $t = T_7$, the restoration rate is reduced at a rate of K_3 until the restoration rate reaches its lowest level of $a_3 < 0$ at $t = T_9$. As the restoration rates are phased out at $t = T_7$, at first the machine condition continues to increase to reach its peak level at $t = T_8$ and retains that value till $t = T_{10}$ when degradation sets in to begin the next such cycle. This dynamic interplay can be captured in its simplest form using the following piecewise constant (nonlinear) differential equations of the form:

$$\frac{d\beta}{dt} = K_1 H_-(\alpha_1 - \beta) H_+(\rho) + K_2 H_+(-\rho) H_-(\beta - \alpha_2) \tag{2.1}$$

$$\frac{d^2\rho}{dt^2} = K_3 H_-(\dot{\rho} - \alpha_3) H_+(\beta - \alpha_4) + K_4 H_+(\alpha_5 - \beta) H_-(\alpha_6 - \dot{\rho}) \tag{2.2}$$

where α_{1-6} are the threshold values of the respective state variables that switch between different regimes, K_{1-4} denote the rates of degradation and restoration as stated in the foregoing, and $H_{-,+}(.)$ represent the switching dynamics, which are defined as follows:

$$H_-(x) = \begin{cases} 0 & x \leq 0 \\ & \\ 1 & x > 0 \end{cases}, \qquad H_+(x) = \begin{cases} 0 & x < 0 \\ & \\ 1 & x \geq 0 \end{cases}.$$

It may be noted that parameters such as $K_1, K_2, \alpha_{1,2}$ have a specific physical connotation in terms of defining the degradation and restoration rates; the peak and breakdown (degraded) conditions, which may be estimated from shop floor PFS data; and the specifications of a machine operating range. For example, K_2 is synonymous with the average

rate of a specific (here, the long time-scale) degradation mode. It may also be noted that higher order differential equations with more complex forms of non-linearity may be used if the present model structures are found to be inadequate to capture the underlying dynamics. Pertinently, the foregoing affine differential equations (2.1,2.2) admit a periodic solution as stated in the following theorem. That periodic solution can capture a recurring, major (large time-scale) mode of breakdown-restoration cycles of real-world manufacturing machine operations.

Theorem 1. If the following conditions hold:

$$K_4(\alpha_5 - \alpha_2) + K_2(\alpha_6 - \alpha_3) \geq 0, \tag{2.3a}$$

$$\alpha_3(\alpha_1 - \alpha_5) + \alpha_6(\alpha_5 - \alpha_2) \leq 0, \tag{2.3b}$$

$$K_3(\alpha_1 - \alpha_4) + K_1(\alpha_6 - \alpha_3) \geq 0, \tag{2.3c}$$

$$2K_3\alpha_6(\alpha_2 - \alpha_4) + K_1(\alpha_6^2 - \alpha_3^2) \geq 0, \tag{2.3d}$$

$$2K_1(-\alpha_1 + \alpha_2)\alpha_6 - K_3(\alpha_1 - \alpha_4)^2 < 0, \tag{2.3e}$$

$$2\,K_4K_1(\alpha_1 - \alpha_5) + K_2(\alpha_6^2 - \alpha_3^2) \geq 0, \tag{2.3f}$$

$$\alpha_3 < 0 < \alpha_2 < \alpha_6 < \alpha_5 < \alpha_4 < \alpha_1, \tag{2.3g}$$

$$K_1 > K_4 > 0 > K_2 > K_3, \alpha_3 = -K_1 \tag{2.3h}$$

then the set of affine equations (2.1,2.2) allows a periodic solution denoted by $x^*(t)$ composed of $I = 10$ segments, with the period given by

$$\begin{aligned} T = (\alpha_6 - \alpha_3)\left(\frac{\alpha_6 - \alpha_3}{2K_4\alpha_6} + \frac{\alpha_6 - \alpha_3}{2(-K_3)(-\alpha_3)}\right) \\ + (\alpha_6 - \alpha_3)\left(\frac{\alpha_1 - \alpha_5}{\alpha_6(-K_2)} + \frac{\alpha_4 - \alpha_2}{K_1(-\alpha_3)}\right) \end{aligned} \tag{2.4}$$

Proof. The constraints in Theorem 1 are proposed to sufficiently guarantee that the system

follows the expected trajectory.

The transition state between consecutive segments $j-1$ and j, $j \in 1, 2, ..., 11$ meets at least one of the following eight switching conditions:

$$\begin{aligned} &\beta_{j-1}(t) = \alpha_1, \quad \rho_{j-1}(t) = 0, \quad -\rho_{j-1}(t) = 0, \quad \beta_{j-1}(t) = \alpha_2, \\ &\dot{\rho}_{j-1}(t) = \alpha_3, \quad \beta_{j-1}(t) = \alpha_4, \quad \beta_{j-1}(t) = \alpha_5, \quad \dot{\rho}_{j-1}(t) = \alpha_6. \end{aligned} \tag{2.5}$$

The times associated with those switching conditions are denoted by $t_j^{(i)}, i \in \{1, 2, ..., 8\}$, $j \in 1, 2, ..., 11$. The switching time (time at which dynamics switches) from segment $j-1$ to j is given by

$$T_j = \min_{k \in I_j} \{t_j^{(k)}\}$$

where

$$I_j = \{k : t_j^{(k)} > T_{j-1}\}.$$

The constraints stated in (2.3) are deemed to enforce a particular switching sequence as detailed in the following exposition. Here, we detail the determination of T_j's and the resulting constraints at segments $j = 1$, and outline the procedure with which other constraints were obtained.

Segment 1: The trajectories in this segment follow transient dynamics until the next switching condition is met. The trajectories are chosen to originate from the following initial condition:

$$\beta(0) = \alpha_1, \rho(0) = 0, \dot{\rho}(0) = -K_1. \tag{2.6}$$

Under these conditions, (2.1,2.2) reduce to

$$\dot{\beta}(t) = K_2, \ddot{\rho}(t) = 0. \tag{2.7}$$

And the system trajectories are defined by

$$\beta_0(t) = \alpha_1 + K_2 t, \rho_0(t) = K_1(-t). \tag{2.8}$$

Segment 2: Solving for t's in (2.5) we have the following candidates for switching time T_1:

$$t_1^{(1)} = t_1^{(2)} = t_1^{(3)} = 0,$$

$$t_1^{(4)} = \frac{-\alpha_1 + \alpha_2}{K_2}, t_1^{(6)} = \frac{-\alpha_1 + \alpha_4}{K_2}, t_1^{(7)} = \frac{-\alpha_1 + \alpha_5}{K_2}. \tag{2.9}$$

Also, $t_1^{(5)}, t_1^{(8)}$ are not admissible, as the corresponding switching conditions violate the dynamics at the boundary as specified in (2.12).

Segment 2 models the degradation of the machine from its peak condition, where when $\beta(t)$ decreases to a certain level α_5, the restoration must increase. Therefore, we want the event associated with $t_1^{(6)}$ precedes other $t_1^{(i)}$'s, i.e., $T_1 = \min\{t_1^{(4)}, t_1^{(6)}, t_1^{(7)}\} = t_1^{(6)} = \frac{\alpha_4 - \alpha_1}{K_2}$. This condition could hold if (2.3g,2.3h) are met.

Consequently, the dynamics Eqs. (2.1,2.2) reduces to:

$$\dot{\beta}(t) = K_2, \tag{2.10}$$

$$\ddot{\rho}(t) = 0. \tag{2.11}$$

Also, for the trajectory within segment 2, the initial conditions are given by:

$$\begin{aligned}
\beta(T_1) &= \alpha_4, \\
\rho(T_1) &= \frac{K_1}{K_2}(\alpha_1 - \alpha_4), \\
\dot{\rho}(T_1) &= -K_1.
\end{aligned}$$

and the trajectory within this segment is given by:

$$\beta_1(t) = \alpha_1 + K_2 t, \tag{2.13a}$$

$$\rho_1(t) = K_1(-t). \tag{2.13b}$$

Applying this procedure to all subsequent segments, the constraints in (2.3) sufficiently allow a periodic solution with 10 switches. □

Remark 1. All the constraints are applied to guarantee the solution follows the desired path, which is popular in practical manufacturing machine.

The constraints 2.3(a-d) may be interpreted as follows: Eqn. (2.3a) reduces to $\frac{(\alpha_6-\alpha_3)}{K_4} \leq \frac{(\alpha_5-\alpha_2)}{-K_2}$. This means that the time it takes restoration rate $\dot{\rho}$ to reach its maximum value must be smaller than the time for the system state β to degrade from its peak to the lowest state. Similarly, Eqn. (2.3c) implies that the time it takes $\dot{\rho}$ to relax to its lowest value from its peak value should be longer than the time for the system state β to reach the maximum state from the restoration relaxing state.

From (2.3b) it follows that the state at which the acceleration of the cumulative restoration $\rho(t)$ should be initiated is bounded as: $\alpha_5 \leq \frac{\alpha_6\alpha_2-\alpha_3\alpha_1}{\alpha_6-\alpha_3}$, from (2.3d) it follows that the state at which the restoration should be reduced is bounded as $\alpha_4 \geq \frac{K_1(\alpha_6^2-\alpha_3^2)}{2(-K_3)\alpha_6} + \alpha_2$, and Eqn. (2.3h) defines the highest rate for relaxing the restoration rate $\dot{\rho}(t)$ in terms of the highest effective restoration rate $\dot{\beta}(t)$.

Theorem 2. When the antecedents of Theorem 1 hold, time to failure (TTF), TTR, and availability (**A**) are given by the following expressions:

$$TTF = \frac{\alpha_2 - \alpha_1}{K_2} + (1 - \frac{\alpha_6}{\alpha_3})(\frac{\alpha_4 - \alpha_2}{K_1} - \frac{\alpha_6 - \alpha_3}{2K_3}) \tag{2.14}$$

$$TTR = \frac{(\alpha_6 - \alpha_3)^2}{2K_4\alpha_6} + \frac{\alpha_5 - \alpha_2}{K_2} + \frac{\alpha_3(\alpha_1 - \alpha_5)}{K_2\alpha_6} \tag{2.15}$$

$$\mathbf{A} = [K_4(K_1\left(2K_3\left(\alpha_2-\alpha_1\right)\alpha_3 + K_2\left(\alpha_3-\alpha_6\right)^2\right)$$
$$-2K_2K_3\left(\alpha_2-\alpha_4\right)\left(\alpha_3-\alpha_6\right))\alpha_6]$$
$$[K_1^3K_2K_3\alpha_3 - 2K_2K_3K_4\left(\alpha_2-\alpha_4\right)\left(\alpha_3-\alpha_6\right)\alpha_6$$
$$+2K_1^2K_3\alpha_3\left(K_4\left(\alpha_5-\alpha_1\right)+K_2\alpha_6\right)$$
$$+K_1\alpha_6(K_2K_4\left(\alpha_3-\alpha_6\right)^2$$
$$+K_3\alpha_3\left(2K_4\left(\alpha_5-\alpha_1\right)+K_2\alpha_6\right))]^{-1}. \tag{2.16}$$

Proof. Following Theorem 1, the time between failure (the period of the solution to (2.1,2.2)), time to repair, time to failure and availability are given by: TBF=$TBF = T_{11}-T_1, TTR = T_5 - T_4, TTF = TBF - TTR, \Lambda = \frac{TTF}{TBF}$. By substituting formulas for T_1, T_4, T_5, T_{11} derived from the proof of Theorem 1 we have (2.14,2.15,2.16). □

Remark 2. The following interpretations may be forwarded on how the model parameters influence machine performance characteristics: From (2.15) it follows that TTR will decrease if $-\alpha_3$, the limiting value of $\dot{\rho}$, decreases (which causes $\frac{(\alpha_6-\alpha_3)^2}{2K_4\alpha_6}$ and $\frac{-\alpha_3(\alpha_1-\alpha_5)}{-K_2\alpha_6}$ to decrease), or $\alpha_5 - \alpha_2$ increases (which causes $\frac{\alpha_5-\alpha_2}{-K_2}$ to increase). Note that $\alpha_5 - \alpha_2$ increases if α_5 increases (i.e, we start the restoration process sooner relative to the most degraded state α_2) or α_2 decreases (i.e., the machine has a very low degraded state).

From (2.14) it follows that TTF will increase if any of the following conditions hold: (i) the range of operating states of a machine $\alpha_1 - \alpha_2$ increases or the effective degradation rate $-K_2$ decreases; (ii) the state of the machine at which the restoration rate reduces, α_4 increases or the maximum effective restoration rate, K_1, decreases; (iii) the range of restoration rate $\alpha_6 - \alpha_3$ increases, and the maximum restoration rateα_6 and the peak restoration reducing rate $-\alpha_3$ increases. Note that the last two situations imply that $(\frac{\alpha_6}{-\alpha_3}+1)(\frac{\alpha_4-\alpha_2}{K_1}+\frac{\alpha_6-\alpha_3}{2(-K_3)})$ increases.

The availability, $\mathbf{A}$, increases if TTR does not increase as TTF increases. For example,

when $-K_3$, the restoration acceleration decreases (with other parameters unchanged), and TTF increases, with TTR remaining unchanged. This leads to an increase in $\mathbf{A}$.

2.2.2 Stability characteristic

This section is devoted to studying the dynamics behavior including basin of attraction and the stability condition of the solution [21]. Here, the stability of the periodic orbits of such piecewise affine models is defined in terms of the eigenvalues of the Jacobian matrix of a Poincare's map, referred to as a *trajectory sensitivity matrix* [22]. Stability, at least local, of the periodic solutions is necessary to ensure that the numerical solutions converge over time, at a well-defined mixing rate, with the theoretical steady state periodic orbits. We also provide an expression for the basin of attraction, which can help quantify the robustness of the periodic solution to finite perturbations. The larger the basin of attraction, the more robust are the steady simulation outputs to numerical imprecision and other perturbations. To simplify the model and put it into the general setting of the control theory, (2.1,2.2) can be written in the following piecewise affine form

$$\dot{x} = A_i x + B_i \tag{2.17}$$

where $x \triangleq (\beta, \rho, \dot{\rho})^T$, $A_i = A = (a_{mn})_{3\times 3}, i \in \{1, ..., 10\}$ such that

$$a_{mn} = \begin{cases} 1 & \text{if } (m,n) = (2,3), \\ 0 & \text{otherwise} \end{cases}$$

and $B_i = (b_{1i}, 0, b_{3i})^T$, with $b_{1i} \in \{K_1, K_2, K_1 + K_2, 0\}, b_{3i} \in \{K_3, K_4, K_3 + K_4, 0\}$. The switching surfaces are 2-dimensional hyperplanes of the form $\mathcal{S}_i = \{x | C_i x = d_i\}$,

$i \in \{1, ..., 10\}$ with C_i's given by

$$C_1 = C_2 = C_4 = C_6 = C_7 = C_8 = (1\ 0\ 0), \tag{2.18a}$$

$$C_3 = C_9 = (0\ 0\ 1), C_5 = C_{10} = (0\ 1\ 0). \tag{2.18b}$$

The switching dynamics of the periodic solution (dotted line) stated in Theorem 1 is

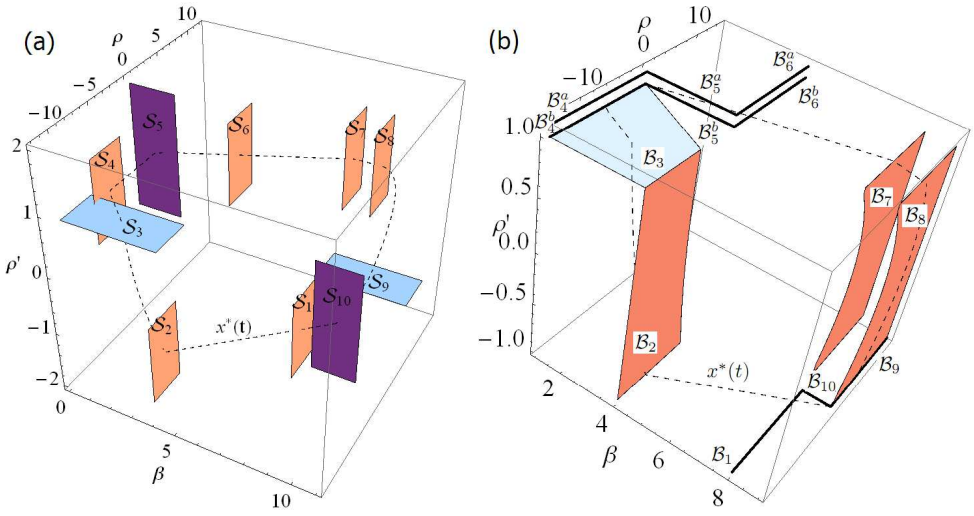

Figure 2.2: (a) Switching dynamics of a periodic solution (b) Basin of attraction of a periodic trajectory.

depicted in Fig. 2.2a. Let us denote by $x_i^*(t),\ i = 1..10$, the segments of a periodic trajectory that starts at $x_i^*(T_i) \in \mathcal{S}_i$ and ends at $x_{i+1}^*(T_{i+1}) \in \mathcal{S}_{i+1},\ i = 1..9$. Let us denote by Λ the Poincare map of points in a small neighborhood $\mathscr{B}(x_1^*)$ of $x_1^*(T_1)$ in $\mathcal{S}_1$, i.e., $\Lambda : \mathscr{B}(x_1^*) \to \mathcal{S}_1$. For such a class of hybrid systems, the Lyapunov theory or Poincare maps [23] are the chief means to investigate stability. The following sufficient condition for the local stability of the periodic solution (limit cycle) follows from this construct.

Proposition 1. [22] The Jacobian W of the Poincare map Λ is given by

$$W = W_{10}W_9..W_2W_1,$$

where

$$W_i = \left(E - \frac{v_i C_{i+1}}{C_{i+1} v_i}\right) e^{A_i t_i^*} \tag{2.19}$$

with $v_i = A_i x_{i+1}^* + B_i, i \in \{1, 2, 3, ..., 10\}$ and E is the identity matrix. The periodic solution of the system is (a) locally stable if all eigenvalues λ_j^w of W lie strictly within the unit disk, i.e., $|\lambda_j^w| < 1, j = 1..3$, and (b) unstable if at least one of the eigenvalues of W lies outside the unit disk.

Here W is referred to as the trajectory sensitivity matrix. Proposition 1 leads to the following result for the stability of periodic solution $x^*(t)$ of (2.17).

Theorem 3. The periodic solution $x^*(t)$ of (2.17) is locally stable.

Proof. We prove this Theorem based on Proposition 1. Here, $A_i = \begin{pmatrix} 0 & 0 & 0 \\ 0 & 0 & 1 \\ 0 & 0 & 0 \end{pmatrix} = 0,$ and $A_i^2 = 0$.Therefore,

$$e^{A_i t_i^*} = \sum_{k=0}^{\infty} \frac{1}{k!} (A_i t_i^*)^k = E + A_i t_i^* \tag{2.20}$$

where E is the identity matrix and $t_i^* = T_{i+1} - T_i$

Combining (2.19) and (2.20) we have $W_i = \left(E - \frac{v_i C_{i+1}}{C_{i+1} v_i}\right)(E + A_i t_i^*)$, and

$$W = \Pi_{i \in I} W_i, \; I = \{1, ..., 10\} - \{6\}. \tag{2.21}$$

Note that matrix W_6 is not included in (2.21), as the system dynamics does not change

when the trajectory cuts plane $\mathcal{S}_6$.

From (2.18) and (2.21), it follows that $W = 0$, and all eigenvalues λ_j^w are zero and thus lie within the unit circle. Consequently, the periodic solution $x^*(t)$ of (2.17) is locally stable. □

The basin of attraction of the locally stable periodic solutions emerging from an initial condition $x^*(0) = (\beta_0, \rho_0, \dot{\rho}_0)$ may be gathered from the following sufficient condition.

Theorem 4. The solution of (2.1,2.2) will converge to the periodic solution $x^*(t)$ given in Theorem 1 if

$$\begin{aligned} \alpha_5 \leq \beta_0 \leq \alpha_4, \rho_0 \leq 0, \alpha_3 \leq \dot{\rho}_0 \quad &< \quad 0, && \text{(2.22a)} \\ K_2 \left(-2\rho_0 K_4 + \left(\dot{\rho}_0 - \alpha_6\right)^2\right) + & \\ 2K_4 \left(\beta_0 \dot{\rho}_0 - \alpha_2 \alpha_6 + \alpha_5 \left(-\dot{\rho}_0 + \alpha_6\right)\right) \quad &\leq \quad 0 && \text{(2.22b)} \end{aligned}$$

and the inequalities specified in (2.3) hold for the model parameters.

Proof. Similar to the method presented in Theorem 1, the constraints (2.23) are proposed to sufficiently guarantee that the system follows the expected trajectory.

$$\begin{aligned} \alpha_2 \leq \beta_0 \leq \alpha_4, \rho_0 < 0, \dot{\rho}_0 \geq \alpha_6 \text{ or } \beta_0 \geq \alpha_5, && \text{(2.23a)} \\ \beta_0 \leq \alpha_1, -\frac{\rho_0}{\dot{\rho}_0} \leq 0, && \text{(2.23b)} \\ \dot{\rho}_0 K_2^2 + \sqrt{K_2^3 \left(K_2 \left({\dot{\rho}_0}^2 - 2\rho_0 K_4\right) + 2\dot{\rho}_0 K_4 \left(\beta_0 - \alpha_5\right)\right)} \geq 0, && \text{(2.23c)} \\ \alpha_3 \leq \dot{\rho}_0, K_4 \left(\alpha_2 - \alpha_5\right) + K_2 \left(\dot{\rho}_0 - \alpha_6\right) \leq 0, && \text{(2.23d)} \\ K_2 \left(-2\rho_0 K_4 + \left(\dot{\rho}_0 - \alpha_6\right)^2\right) & \\ +2K_4 \left(\beta_0 \dot{\rho}_0 - \alpha_2 \alpha_6 + \alpha_5 \left(\alpha_6 - \dot{\rho}_0\right)\right) \leq 0. && \text{(2.23e)} \end{aligned}$$

Because of (2.23a), (2.23b) is reduced to $\dot{\rho}_0 < 0$. As a consequence, ($\dot{\rho}_0 \geq \alpha_6$ or $\beta_0 \geq \alpha_5$)

in (2.23a) is reduced to $\beta_0 \geq \alpha_5$. Als

$$K_4\left(\alpha_2-\alpha_5\right)+K_2\left(\dot{\rho}_0-\alpha_6\right)\leq 0 \Leftrightarrow \dot{\rho}_0 \geq \frac{-K_4\left(\alpha_2-\alpha_5\right)}{K_2}+\alpha_6$$

On the other hand,

$\frac{-K_4(\alpha_2-\alpha_5)}{K_2}+\alpha_6-\alpha_3=\frac{K_4(\alpha_5-\alpha_2)+K_2(\alpha_6-\alpha_3)}{K_2}\leq 0$

because of (2.3a,2.3h). Therefore, $\frac{-K_4(\alpha_2-\alpha_5)}{K_2}+\alpha_6 \leq \alpha_3$. It follows that (2.23d) is satisfied if $\alpha_3 \leq \dot{\rho}_0$.

(2.23c) is equivalent to

$$\begin{aligned}\sqrt{K_2^3\left(K_2\left(\dot{\rho_0}^2-2\rho_0 K_4\right)+2\dot{\rho}_0 K_4\left(\beta_0-\alpha_5\right)\right)} &\geq -\dot{\rho}_0 K_2^2 \\ \Leftrightarrow \left(-\rho_0 K_2+\dot{\rho}_0\left(\beta_0-\alpha_5\right)\right) &\leq 0. \end{aligned} \tag{2.24}$$

(2.24) is satisfied as $\rho_0, \dot{\rho}_0 \leq 0, K_2 \leq 0, \beta_0 \geq \alpha_5$. Therefore, (2.23) is equivalent to (2.22). □

From the above proof, the constraints specified in (2.22) ensure that the system evolution patterns shadow the periodic solution $x^*(t)$; specifically, the system state converges to (actually merges with) $x_5^*(T_5)$, the initial state of the 5^{th} segment on the trajectory of $x^*(t)$.

Remark 3. Eqn. (2.22) implies that initial degradation state β_0 is bounded between starting restoration state α_5 and relaxing restoration state α_4; the initial cumulative restoration ρ_0 and the restoration rate $\dot{\rho}_0$ are negative, and ρ_0 and $\dot{\rho}_0$ must fulfill the quadratic constraint (2.22b).

The basin of attraction may also be derived from combining basins of attraction on all switching surfaces [22]. The basin of attraction (composed of the 4 shaded regions and the bold lines) specified in the following Theorem are depicted in Fig. 2.2b.

Theorem 5. The trajectories that start from the following specified regions on the switching surfaces converge to the limit cycle $x^*(t)$ defined in Theorem 1

On $\mathcal{S}_1$: $\dot{\rho}_0 = \alpha_3, \rho_0 \leq \max\{0, \frac{(\alpha_3(\alpha_4-\alpha_5)+(-\alpha_2+\alpha_5)\alpha_6)}{K_2} + \frac{(\alpha_3-\alpha_6)^2}{2K_4}\}$.

On $\mathcal{S}_2$: $\max\{-\frac{K_4(\alpha_2-\alpha_5)}{K_2} + \alpha_6, \alpha_3\} \leq \dot{\rho}_0 < \alpha_6, \dot{\rho}_0^2 \geq \alpha_6^2 + 2K_4\rho_0, \rho_0 \leq 0, 2K_4(\alpha_2 - \alpha_5)\alpha_6 > K_2((\dot{\rho}_0 - \alpha_6)^2 - 2K_4\rho_0)$.

On $\mathcal{S}_3$: $\alpha_2 < \beta_0 \leq \alpha_5, \alpha_6\,(-\alpha_2 + \beta_0) < K_2\rho_0$.

On $\mathcal{S}_4$: $\{\rho_0 < 0, \dot{\rho}_0 = \alpha_6\}$ or $\{\rho_0 < 0, \dot{\rho}_0 = -\frac{K_3(\alpha_1-\alpha_4)}{K_1} + \alpha_6\}$.

On $\mathcal{S}_5$: $\{\dot{\rho}_0 = \alpha_6, \min\{\alpha_5, \frac{K_3(\alpha_1-\alpha_4)^2}{2K_1\alpha_6} + \alpha_1, \frac{K_1\left(\alpha_3^2-\alpha_6^2\right)}{2K_3\alpha_6} + \alpha_4\} \geq \beta_0 \geq \alpha_2\}$ or $\{\dot{\rho}_0 = -\frac{K_3(\alpha_1-\alpha_4)}{K_1} + \alpha_6,$
$\min\{\alpha_5, \frac{K_3(\alpha_1-\alpha_4)^2}{2K_1\alpha_6} + \alpha_1, \frac{K_1\left(\alpha_3^2-\alpha_6^2\right)}{2K_3\alpha_6} + \alpha_4\} \geq \beta_0 \geq \alpha_2\}$.

On $\mathcal{S}_6$: $\{\dot{\rho}_0 \geq \frac{-K_3(\alpha_1-\alpha_4)}{K_1} + \alpha_6, \rho_0 \geq 0, K_3\,(\alpha_1 - \alpha_4)^{\,2} + 2\dot{\rho}_0 K_1\,(\alpha_1 - \alpha_5) + 2K_1^2\rho_0 > 0,$
$2\dot{\rho}_0 K_3\,(\alpha_4 - \alpha_5) + K_1\,(-\dot{\rho}_0^2 + \alpha_3^2 + 2K_3\rho_0) < 0\}$.

On $\mathcal{S}_7$: $\{\rho_0 \geq 0, \dot{\rho}_0 = \alpha_6\}$ or $\{\rho_0 \geq 0, \dot{\rho}_0 = -\frac{K_3(\alpha_1-\alpha_4)}{K_1} + \alpha_6\}$.

On $\mathcal{S}_8$: $\{\rho_0 > 0, \alpha_3 < \dot{\rho}_0 \leq \alpha_6, \alpha_3^2 + 2K_3\rho_0 < \dot{\rho}_0^2\}$.

On $\mathcal{S}_9$: $\{\beta_0 = \alpha_1, \rho_0 > 0\}$.

On $\mathcal{S}_{10}$: $\{\rho_0 > 0, \dot{\rho}_0 = \alpha_3, \alpha_1 \geq \beta_0 > \max\{\alpha_4, -\frac{K_2}{2K_4\alpha_3}\,(\alpha_3 - \alpha_6)^{\,2} + \frac{1}{\alpha_3}(\alpha_2\alpha_6 + \alpha_5(\alpha_3 - \alpha_6)), \frac{K_2\left(-{\alpha_3}^2+\alpha_6^2\right)+2\alpha_3K_4\alpha_5}{2\alpha_3K_4}\}\}$.

Proof. The regions defined in Theorem 5 are the basin of attraction on each of the surfaces and are similar for each surface. The idea is to propose the constraints in the form of sufficient conditions such that the system follows the expected trajectory. The method to construct such conditions are similar to the ones presented in Theorem 1.

Let us consider the impact map from surface 6 to 7, the Lipschitz constant k, if it exists,

is the smallest number k such that

$$\left(\sqrt{1 + \frac{\left(\frac{\Delta(\dot{\rho_0})(\alpha_4 - \alpha_5)}{K_1}\right)^2 + 2\frac{\Delta(\dot{\rho_0})(\alpha_4 - \alpha_5)}{K_1}\Delta\rho_0}{\Delta\left(\dot{\rho_0}\right)^2 + \Delta\rho_0^2}} \right) \leq k. \tag{2.25}$$

However, when $\Delta\left(\dot{\rho_0}\right) = \Delta\rho_0$, the left hand side of (2.25) is reduced to

$$\sqrt{1 + \frac{(\frac{\alpha_4 - \alpha_5}{K_1})^2 + 2\frac{(\alpha_4 - \alpha_5)}{K_1})}{2}} > 1.$$

Therefore, the impact map is not contracting. As a consequence, the basin of attraction formulated in Theorem 5 contain the basin of attraction derived using the method in [22].

□

Remark 4. Note that all the constraints used to bound the basin of attraction on each switching surface are added to sufficiently guarantee that the switching order of the periodic solution of Eqs. (2.1,2.2) is maintained. As a consequence, the system returns to a point on $x^*(t)$. Thus, the system is stable.

Remark 5. The basin of attraction formulated using the earlier method in [22] is constructed in 2 steps. The first step bounds a set in form of ellipsoids from which the impact maps [22] are contracted. This set is then shrunk to maintain the switching order. For the present system, some impact maps are not contracting. This leads to the following result.

Proposition 2. The basin of attraction formulated in Theorem 5 contains the basin of attraction derived using the method in [22].

This result is part of the proof represented in 5.

2.3 Stochastic model for modeling short time breakdown and repair of a single machine and the multimodal distribution

In this Section, we will extend the model in (2.1,2.2) to include the effects of minor breakdowns that happen in short time scale by introducing a stochastic form of α_2 and K_2. As shown in Fig. 2.4b, data collected in this study exhibits a multimodal distribution. The right mode presents major breakdowns that happen in long time-scale and can be modeled by the deterministic model in Section 2.2. The left mode presents minor breakdowns happen randomly in short time scale and will be considered in this Section.

Lemma 1: *If $\gamma(t)$ is mean square (ms) continuous process with $|\gamma(t)| > a > 0$ a.e. (almost everywhere), then the integral*

$$\int_{T_4+(tdivTBF)\times TBF}^{t} K_2 H_+(\gamma(\tau))d\tau \tag{2.26}$$

exists and is differentiable.

Proof. Proof: Let us define $\Delta(x) = \text{sgm}(x,k) - H_+(x)$, where $\text{sgm}(x,k) = \frac{1}{1+e^{-kx}}$. It may be noted that

$$\forall x \in \mathbb{R}, \text{and} |x| > a > 0, \text{ we have } |\Delta(x)| \to 0 \text{ uniformly as } k \to \infty \tag{2.27}$$

This is because

$\forall x > a, |\Delta(x)| = |\frac{1}{1+e^{-kx}} - 1| = |\frac{-e^{-kx}}{1+e^{-kx}}| < e^{-kx} < e^{-ka} \to 0$ as $k \to \infty$.

$\forall x < -a, |\Delta(x)| = |\frac{1}{1+e^{-kx}} - 0| < |\frac{1}{1+e^{ka}}| \to 0$ as $k \to \infty$.

Now, substituting x with $\gamma(t)$ for some $|\gamma(t)| > a > 0$, a.e., in (2.27), it follows that $\forall \varepsilon > 0, \exists K \in \mathbb{N}$ such that $|\Delta(\gamma(t))| < \varepsilon$, $\forall t > 0$ and $k > K$. Consequently, $E[|\Delta(\gamma(t))|^2] < E[\varepsilon^2] = \varepsilon^2$ as $k > K, \forall t > 0$, or $\forall t > 0$, $\text{sgm}(\gamma, k)$ converges uniformly in the ms sense to $H(\gamma)$ as $k \to \infty$. Furthermore, $\text{sgm}(\gamma, k)$ is ms continuous because

sgm(.) is continuous, and $\gamma(t)$ is ms continuous. Therefore, it follows that $H(\gamma)$ is ms continuous [24] (Theorem 3.3 p. 62). Consequently, the integral (2.26) exists and is differentiable [24] (Corollary 2 p. 67). □

For the following Theorem, we consider the system in one period, i.e., $0 \leq t \leq T$.

Theorem 6. If antecedents of Theorem 1 hold and α_2 and K_2 are as follows:

$$\alpha_2(t) = \begin{cases} \alpha_2^0 - \gamma(t) + \int_{T_4}^{t} K_2^0 H_+(\gamma(\tau))d\tau & \text{if } T_4 \leq t < T_5 - \epsilon \quad (2.28a) \\ \alpha_2^0 - \varepsilon\tilde{K_2} & \text{if } T_5 - \epsilon \leq t \leq T_5 \quad (2.28b) \\ \alpha_2^0 & \text{otherwise} \quad (2.28c) \end{cases}$$

$$\tilde{K_2} = -\frac{1}{\varepsilon}\int_{T_4}^{T_5-\epsilon} K_2^0 H_+(\gamma(\tau))d\tau. \quad (2.29)$$

$$K_2(t) = \begin{cases} \tilde{K_2} & \text{if } T_5 - \varepsilon \leq t < T_5 \quad (2.30a) \\ K_2^0 & \text{otherwise} \quad (2.30b) \end{cases}$$

where $0 < \varepsilon < T_5 - T_4$, then TBF and TTR in this period exhibit right skewed distributions with skewness in the range of 1.4–2. Here, $\gamma(t)$ is a random process whose time intervals between successive zero-crossings follow exponential distribution with rate ν; α_2^0, K_2^0 are the values, respectively, of α_2, and K_2 in the deterministic model (2.1,2.2); and $T_4 = (\frac{\alpha_1-\alpha_2}{-K_2}), T_5 = \frac{(K_1+\alpha_6)(2K_4(\alpha_5-\alpha_1)+K_2(K_1+\alpha_6))}{2K_2K_4\alpha_6}$.

Proof. First, consider the random process $\gamma(t) = (-1)^{N(t)}$ [25] (p. 379), where $N(t)$ is a Poisson process with parameter λ, and $N(0)$ is a Bernoulli binary random variable with equal probability for outcomes 0,1. Evidently, $R_{\gamma\gamma}(t_1, t_2) = e^{-2\lambda|t_1-t_2|}(t_1, t_2 \geq 0)$ is continuous at (t, t). Therefore, it follows from [24] (Theorem 3.2 p. 61) that $\gamma(t)$ is an ms

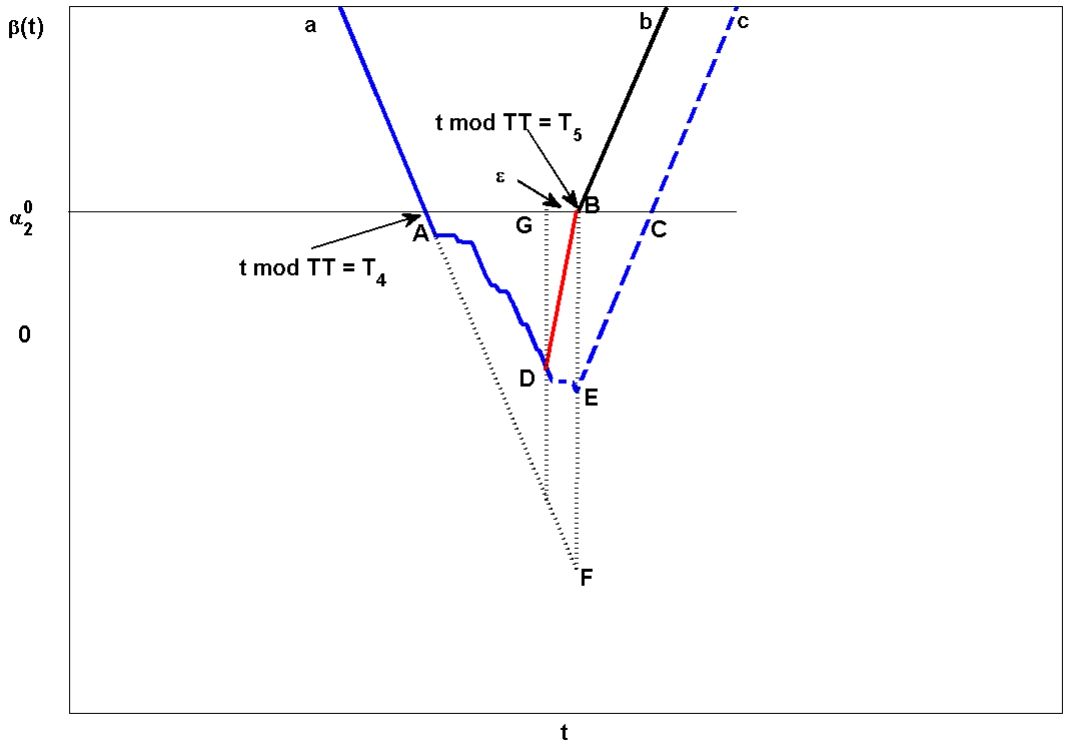

Figure 2.3: Diagram of proof of Theorem 6. Without any perturbation, the system evolves as aAGBb. With perturbation to α_2 and $\epsilon = 0$, the system evolves as aADECc. With perturbation to both α_2 and K_2, the system evolves as aADBb.

continuous process. Also, the time intervals between successive zero crossings of $\gamma(t)$ are the same as those between consecutive events of the Poisson process $N(t)$, and hence they follow an exponential distribution.

Without loss of generality, let us consider the perturbation for the first period, $T_1 \leq t \leq T + T_1$ of the periodic solution in Fig. 2.1 as in (2.28,2.29). Note that similar constructions

follow for other periods. Let us consider $\beta(t)$ defined as:

$$\beta(t) = \begin{cases} \alpha_2^0 + \int_{T_4}^{t} K_2^0 H(\gamma(\tau))d\tau & \text{if } T_4 \leq t < T_5 - \varepsilon \quad (2.31a) \\ \alpha_2^0 + \tilde{K}_2[t - T_5] & \text{if } T_5 - \varepsilon \leq t < T_5 \quad (2.31b) \\ \beta^0(t) & \text{otherwise,} \quad (2.31c) \end{cases}$$

where $\beta^0(t)$ is the solution of the unperturbed deterministic model in the corresponding region, $\tilde{K}_2$ is defined in Eqn. (2.29).

To show that $\rho(t)$ satisfies (2.2), we note from (2.31) that $\beta(t) \leq \alpha_2^0$ as $K_2^0 \leq 0$ when $T_4 \leq t < T_5 - \varepsilon$ in (2.31a) and $K_2[t - T_5] \leq 0$ when $T_5 - \varepsilon \leq t < T_5$ in (2.31b). Therefore, when $T_4 \leq t \leq T_5$, $\beta(t) \leq \alpha_2^0 < \alpha_5 < \alpha_4$, i.e., $\rho(t)$ satisfies (2.2). Outside this region, $\rho(t)$ automatically satisfies (2.2) because of its definition.

Let us now verify that $\beta(t)$ defined in (2.31) satisfies (2.1). From (2.31a) and (2.28a) we have

$$\beta(t) - \alpha_2(t) = \gamma(t). \quad (2.32)$$

Applying Lemma 1 to (2.31a), we have:

$$\frac{d\beta(t)}{dt} = K_2^0 H(\gamma(t)). \quad (2.33)$$

It follows from (2.32) and (2.33) that $\frac{d\beta(t)}{dt} = K_2^0 H(\beta(t) - \alpha_2(t))$ or $\beta(t)$ satisfies (2.1).

Similarly, from (2.31b) and (2.28b) we have

$$\beta(t) - \alpha_2(t) = \tilde{K}_2[t - (T_5 - \varepsilon)] \geq 0$$

and

$$\frac{d\beta(t)}{dt} = \tilde{K}_2 = \tilde{K}_2 H(\beta(t) - \alpha_2(t))$$

or $\beta(t)$ satisfies (2.1).

At $t = T_5$, $\alpha_2(T_5) = \alpha_2^0$, $\beta(T_5) = \alpha_2^0, \rho(T_5) = \rho_5(T_5), \rho^{'}(T_5) = \rho_5^{'}(T_5)$. When $t \to T_5^+$, $\beta^{'}(t) = \beta_5^{'}(t)$ and $\rho^{''}(t) = \rho_5^{''}(t)$. Therefore, the system dynamics does not change outside $[T_4, T_5)$.

Furthermore, as $\beta(t) - \alpha_2(t) = \gamma(t)$ for $T_4 \leq t < T_5 - \varepsilon$, it may be noted that the zero crossing time-points of $\gamma(t)$ and $\beta(t) - \alpha_2(t)$ are identical. As as result, the interval between the i^{th} and $(i+1)^{th}$ zero crossing of $\beta(t) - \alpha_2(t)$ denoted by τ_i are independent and follows exponential distribution with mean interval length of $\frac{1}{\lambda}$.

Case 1: the first zero results from a down crossing and TTRs: $\tau_1, \tau_3, \ldots$ follow exponential distribution.

Case 2: the first zero results from an up crossing and TTRs: $\tau_2, \tau_4, \ldots$ follow exponential distribution.

In both cases, TBF: $\tau_1 + \tau_2, \tau_3 + \tau_4, \ldots$ follow Erlang distribution with parameters (2,λ) [26]. Thus, TTRs follow the exponential distribution with skewness of 2, and TBFs follow the Erlang(2) distribution with skewness of $2^{1/2}$. □

Note that in this case, TTR is the time interval between a zero up-crossing and the next zero down-crossing, and TBF is the time interval between 2 consecutive zero down crossings of $\beta(t) - \alpha_2(t)$. The following result shows that our model can capture the multimodal characteristic of TBF.

Corollary 1. *Model (2.1,2.2) with α_2, K_2 as proposed in (2.28,2.30) when $t \leq T$ and $\alpha_2(t) = \alpha_2(t \bmod T)$ when $t \geq T$ can generate TBF that exhibit a multimodal distribution.*

Proof. Note that the result in Theorem 6 is applied for each period of the periodical solution in Theorem 1. In each period, by replacing α_2, K_2 in the deterministic model (2.1,2.2) with (2.28,2.30), there are multiple short TBF which exhibit right skewed distribution as

shown in the Theorem 6. Together with long TBF from the deterministic model (2.1,2.2), we have a multimodal distribution. □

2.4 Numerical validation

In this section, we report 2 case studies. The data sets employed in these case studies contain TBFs and TTRs collected from manufacturing machines of an assembly line of a leading automobile manufacturer. The first study assesses how well the model parameters estimated based on the foregoing theoretical results can capture the distribution of TBF and TTR of each machine in an assembly line. The second case study evaluates the extent to which the model, with parameters "optimally" estimated using a genetic algorithm [27], can be used to simulate the dynamics of the whole assembly line**.**

2.4.1 Performance of the model when applying to a single machine

First, we investigated the distributions of TBF from real world data over short time scales, i.e, TBF<10 min. As shown in Fig. 2.4a, the data exhibit a highly right skewed distribution over the short time-scales. The estimated parameters ($\hat{\nu_l}$) of the exponential distribution models of the short time-scale TBF distribution of various manufacturing machines $l = 1, 2, ..., 14$, (see Table 1) suggest that for most machines, the R^2 for the exponential fit is high, around 90%, and the standard deviation is about 10% of the estimates in many cases. This result implies that $\ln(1 - \widetilde{F(TBF)})$ trends linearly with TBF values, and short-term TBF and TTR can therefore be approximated using an exponential distribution.

Second, we compared the distributions of short time-scale TBF and TTR from the data vs. those generated from the model for the 14 machines of the assembly line. For each machine, the model (2.1,2.2) was parametrized with the value estimated in Table 1, and those values that meet the antecedents of Theorem 3 and the perturbations specified in (2.28,2.29) to mimic the degradation dynamics (e.g., $\hat{\nu} = 0.276$ for Machine 6) and

Table 2.1: Summary of exponential fitting of short-term TBF samples from a real-world manufacturing system.

MC	$\hat{\nu}$	R^2	$\sigma(\%\hat{\nu})$	MC	$\hat{\nu}$	R^2	$\sigma(\%\hat{\nu})$
1	0.23	0.93	12.68	8	0.26	0.89	17.19
2	0.30	0.95	9.79	9	0.32	0.83	18.86
3	0.28	0.97	8.24	10	0.31	0.95	10.43
4	0.29	0.89	16.15	11	0.16	0.93	18.56
5	0.22	0.84	24.70	12	0.34	0.88	17.03
6	0.30	0.88	19.34	13	0.28	0.97	8.24
7	0.25	0.70	27.23	14	0.32	0.88	15.95

$\varepsilon \approx 0.001$. The model with these parameter settings was used to simulate a 600 min long operation of an assembly segment with step size set at 0.01 min. The simulations were replicated 20 times. The closeness of the distributions of model-derived successive zero-crossing (α_2-crossing) intervals (mimicking TTR) to exponential distribution, $\exp(\hat{\nu}_l)$, for each machine was assessed using a Kolmogorov-Smirnov (KS) test. Parenthetically, the KS statistic, κ, is the maximum difference between empirical cdf $\widetilde{F(TBF)}$ and the cdf of $\exp(\hat{\nu})$. The results suggest that the short time-scale TTR from simulations for Machine k are statistically indistinguishable from an exponential distribution $\exp(\hat{\nu}_k)$ (median p-value of about 0.6).

Third, we ran simulations to verify the similarity of overall distributions of simulated vs. actual TBF and TTR. We set the simulation time span to 6000 min and the step size to 0.001 min. As evident from Fig. 2.4 and statistical tests, the histograms of model-generated TBF and TTR for a machine hold a distinct similarity to those from real-world data in that (a) both show a very similar right skewed distribution over short times and (b) the second mode occurs in the same vicinity (here, TBF=1800 min), but the real-world data shows larger dispersion compared to the model-derived distribution.

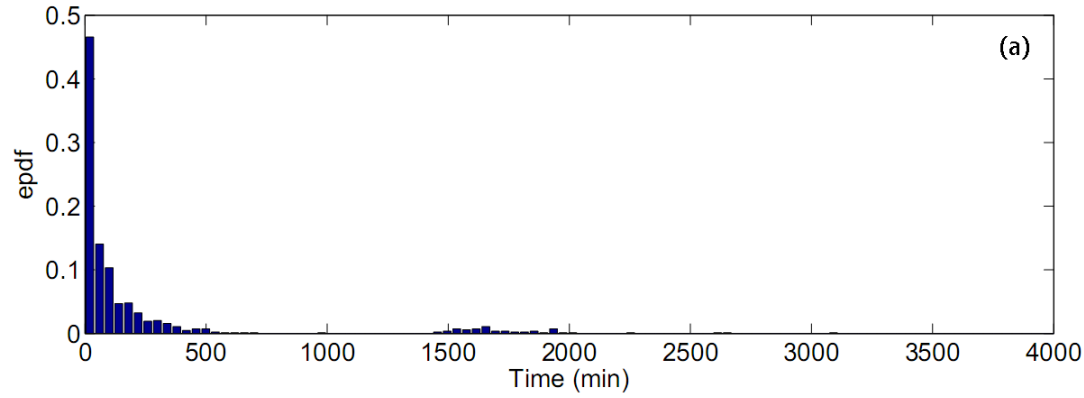

(a)

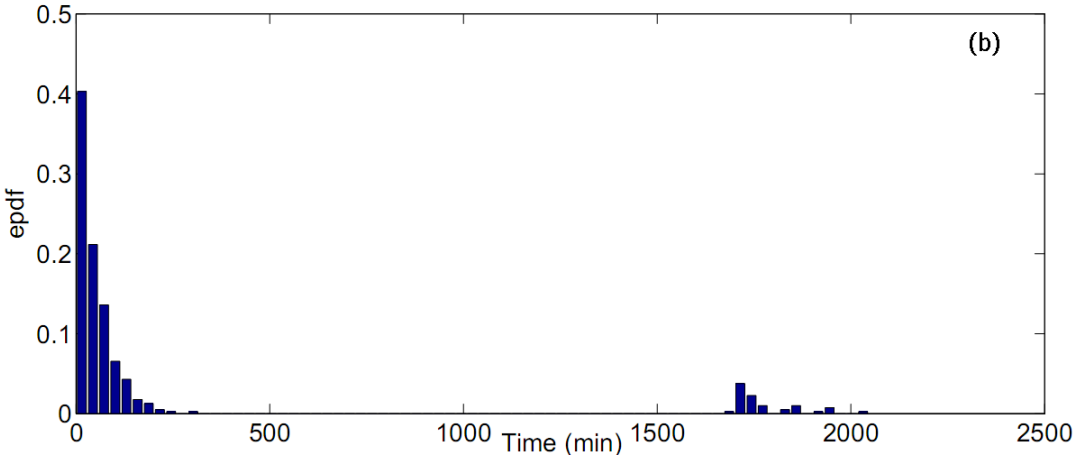

(b)

Figure 2.4: Comparison of histograms of TBF data from a real-world manufacturing assembly machine (station) (a) with that from simulations (b).

2.4.2 Performance of the model when integrating to whole assembly line

In this case study, we applied the foregoing modeling approach to capture the dynamics of machine breakdowns as well as their effect on the throughput in an automotive manufacturing assembly line segment.

As mentioned above, flow modeling approaches have traditionally been used for qualitative analysis of system dynamics and not for real-time performance estimation. Discon-

tinuities in flow caused by blocking, starving, and breakdown events adversely affect the performance of integration routines used to solve the model, and often cause the numerical solution procedures to become unstable. To overcome this drawback, the Heaviside function was replaced by sigmoid function theory [28, 29]. Note that the rationale for this replacement is that sigmoidal functions $\text{sgm}(wx) = \frac{1}{1+e^{-wx}}$ can approximate the Heaviside functions $H_{-,+}(x)$ and improve the efficiency of numerical simulation. It may also be noted that when w gets large enough, we have

$$\lim_{w\to\infty} \text{sgm}(wx) = H_{+,-}(x)$$

Therefore, we can derive approximated vector flow fields that pose fewer numerical instability issues and to facilitate faster simulation of system dynamics. For example, the time taken to generate the solutions shown in Fig. 2.1 for degradation dynamics decreased 2146 times with the use of sigmoidal functions. By using the sigmoidal function of the form $\text{sgm}(x) = (1+e^{-x})^{-1}$, the coupled dynamics of degradation and restoration (2.1,2.2) may be rewritten as:

$$\begin{aligned} d\beta/dt &= K_1\text{sgm}(w_1(\alpha_1-\beta))\text{sgm}(w_2\rho) \\ &\quad + K_2\text{sgm}(-w_3\rho)\text{sgm}(w_4(\beta-\alpha_2)) \\ (d^2\rho)/(dt^2) &= K_3\text{sgm}(w_5(\dot{\rho}-\alpha_3))\text{sgm}(w_6(\beta-\alpha_4)) \\ &\quad + K_4\text{sgm}(w_7(\alpha_5-\beta))\text{sgm}(w_8(\alpha_6-\dot{\rho})) \end{aligned}$$

and the throughput rate is adjusted to account for degradation and starve/block conditions in each machine as

$$u_k(t) = \mu_k(t)\text{sgm}(L_k(t))\text{sgm}(L_{k+1}^{\max} - L_{k+1}(t))\text{sgm}(\beta_k(t)-\beta_k^0) \tag{2.34}$$

As noted earlier, parametrization of the model using historical fault realizations, such as historical records of TBF and TTR, can be significantly challenging. Instead of using a feasible set based on theoretical results, we used a genetic algorithm (GA) to "optimally" select the n-SDE models for each station (labeled Machine 1 through Machine 18) in the real-world manufacturing assembly line segment. In essence, GA performs a stochastic search to determine the model parameters so that the marginal distribution (histogram) of TBF and TTR estimated from the simulation closely match with those from actual data. Notably, the parameters are tuned to capture only the marginal distributions of TTR and TBF. The structure of the differential equations essentially accounts for the TBF-TTR dependencies. The fitness (or the objective) function, Op, of the GA is expressed in terms of the empirical marginal distributions of TTR and TBF as follows

$$
\begin{aligned}
Op = \omega_1 \Bigg(& \frac{\sum_{j=1}^{N_0} (HistTBF(j) - HistTBFa(j))^2}{N_0} \\
& + \frac{\sum_{j=1}^{N_1} (HistTTR(j) - HistTTRa(j))^2}{N_1} \Bigg) \\
& + \omega_2 \Bigg(\frac{\sum_{j=N_0+1}^{N_0+N_2} (HistTBF(j) - HistTBFa(j))^2}{N_2} \\
& + \frac{\sum_{j=N_1+1}^{N_1+N_3} (HistTTR(j) - HistTTRa(j))^2}{N_3} \Bigg) \\
& + \omega_3 \Bigg(\frac{\sum_{j=N_0+N_2+1}^{N_0+N_2+N_4} (HistTBF(j) - HistTBFa(j))^2}{N_4} \\
& + \frac{\sum_{j=N_1+N_3+1}^{N_1+N_3+N_5} (HistTTR(j) - HistTTRa(j))^2}{N_5} \Bigg)
\end{aligned}
$$

Here, the distributions of TBF and TTR estimated from the histogram transformations (HistTBF and HistTTR) of the model solutions were compared with those from the actual fault data (HistTBFa and HistTTRa), and j is the histogram bin index. The histogram bins of TBF from the model (HistTBF) and the actual data (HistTBFa) were partitioned

into the same three groups, each with N_0, N_2, N_4 bins. The first N_0 bins capture the near-exponential distribution of the short TBFs, the next N_2 bins capture the steady non-exponential distribution of the intermediate values of TBF, and the last N_4 bins capture the second mode and beyond of the (large) TBF distribution. Similarly, N_1, N_3, N_5 are the corresponding bins used to compare histogram transformations of TTR distribution from the model (HistTTR) with actual historic data (HistTTRa). The weights for the three areas of the histogram, $\omega_1, \omega_2, \omega_3$, were assigned to be 100, 10, and 1, respectively, to represent their relative importance from an operational standpoint. The simulated as well as the actual TBF and TTR data were gathered over a two-month period. The decision variables for GA optimization include the structural parameters of the model, namely, $\alpha_{1-6}, K_{1-4}, w_{1,4,5,8}, w_2(= w_3)$, and $w_6(= w_7)$, and perturbation parameter ν. The GA essentially tuned these 17 model parameters to reduce Op below a threshold (stopping criterion). Each parameter was modeled as a 35-bit long string. Stochastic optimization methods, such as GAs are known to locate the basin (trough/crest) of the global optimum with a very high probability [30]. For the cases examined, the GA was found to converge to a near-plateau in at most 50 iterations. A Nelder-Mead simplex (NM) method was used to refine the fitness of the solutions because, once the fitness improvement rate drops below a threshold, it is assumed that the parameter values lie in the basin of the global minimum. The resulting GA-parametrized model appears to adequately capture the dynamics of machine degradation, as well as the distributions of TBF and TTR, better than conventional exponential distribution models parametrized from actual data. For instance, Fig. 2.5 shows the marginal PDFs of TTR for a representative assembly station (Machine 2) obtained from the actual historical data (solid blue line) vs. the distribution obtained from the model (red dashed line) vs. the one obtained using the best fit exponential distribution (green dashed dotted line).

It may be noted that the pattern observed for Machine 2 is representative of those from

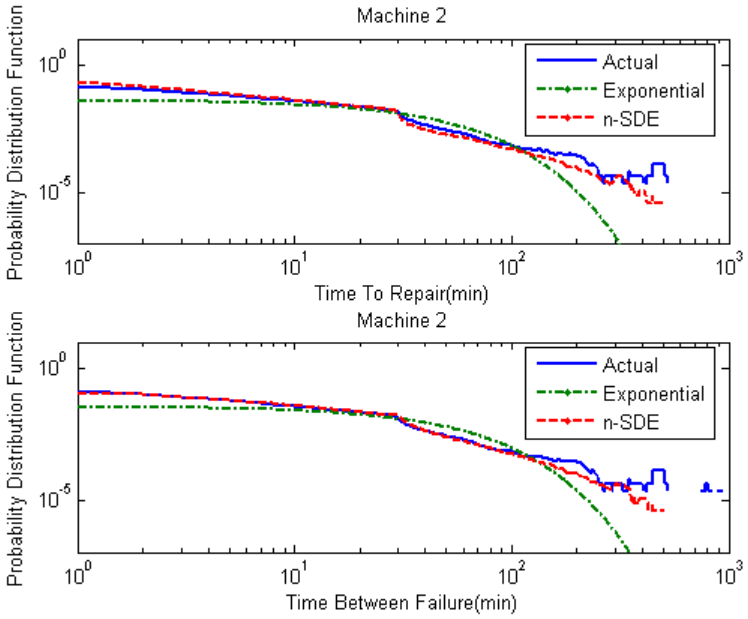

Figure 2.5: Comparison of marginal pdfs of TTR and TBF obtained from actual data (blue), n-SDE model (red), and exponential distribution model (green) for the representative case of Machine 2

most of the other assembly stations barring the ones at either end and the parallel stations. The results suggest that the exponential model underestimates the left tails of TBF and TTR densities by one order of magnitude compared to the actual for all 18 machines. More specifically, the mean square error (MSE) of the distributions from the model is one order in magnitude lower than those from the exponential model. This is likely because the parametrized model can capture the distributions of TBF and TTR much better than the exponential models for short times (i.e., the first minute) as shown in Fig. 2.5, as well as times beyond 100 minutes. Pertinently, Inman's work [31] suggests that exponential distribution may be adequate to capture TTR and TBF distributions in many cases. Consequently, the industry has been using exponential distribution in many of its simulations. The current assembly line segment appears to be an exception to this earlier finding. For example, we noticed significant cross-correlation (0.25-0.55 for large samples) between

Table 2.2: Comparison of mean, standard deviation of TTR and TBF for Machine 2 estimated from n-SDE model vs. actual data

Mean TTR		Std Dev TTR		Mean TBF		Std Dev TBF	
Actual	Model	Actual	Model	Actual	Model	Actual	Model
9.41	9.24	13.59	15.11	27.35	24.71	29.42	25.28
% dev		% dev		% dev		% dev	
1.81%		10.1%		9.67%		14.05%	

TTR and TBF for 6 out of 18 machines. TTR and TBF sequences also exhibited significant auto-correlations and/or nonlinear dependencies [32]. The proposed modeling approach may be a suitable means to capture the variations of TTR and TBF more accurately and to model manufacturing systems with more generic failure distributions and coupled dynamics. The improved model parametrization mentioned above leads to fairly close estimation of the mean (i.e., MTBF, MTTR) and standard deviations of the respective distributions, as shown in Table 2 for Machine 2.

Figs. 2.6a and 2.6b provide a comparison of MTBF and MTTR, respectively, for the 18 machines from the model vs. the actual data. The actual statistics are shown in light green bars (lighter shade) and the model outputs are shown in dark brown (darker shade). The results suggest that MTBF computed from the model lies within 3-10% of that computed from the actual data for 10 of the 18 machines. The model-estimated MTBF values for the remaining 8 machines vary on an average by 24% relative to those computed from actual data. Such large discrepancies may be caused by the inadequacy of the model structure, despite improvements over a simple exponential distribution model, to capture all the salient features of the real-world TBF data. Similarly, the model-estimated MTTR values for 10 machines vary between 2-10% of those computed from the actual data, and vary by an average of 28% from those computed from the actual data for the remaining 8 machines. These results indicate that for 10 out of the 18 machines the parametrized

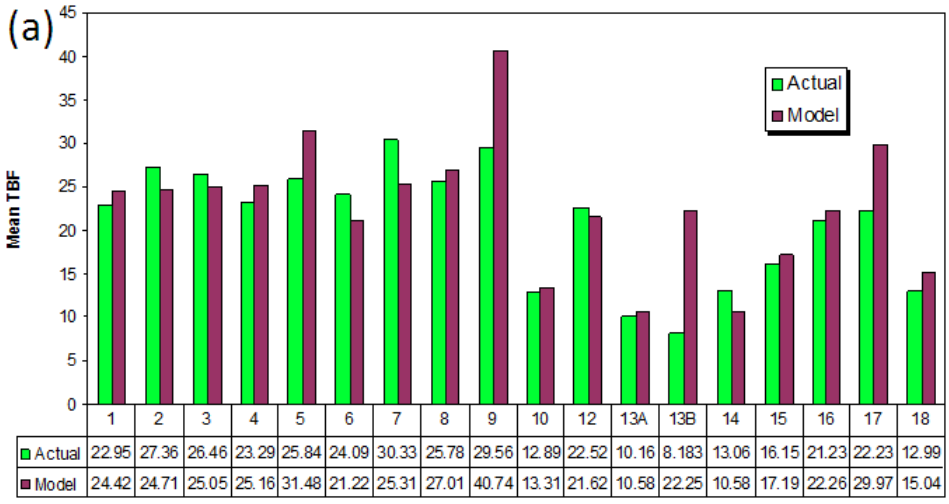

	1	2	3	4	5	6	7	8	9	10	12	13A	13B	14	15	16	17	18
Actual	22.95	27.36	26.46	23.29	25.84	24.09	30.33	25.78	29.56	12.89	22.52	10.16	8.183	13.06	16.15	21.23	22.23	12.99
Model	24.42	24.71	25.05	25.16	31.48	21.22	25.31	27.01	40.74	13.31	21.62	10.58	22.25	10.58	17.19	22.26	29.97	15.04

(a)

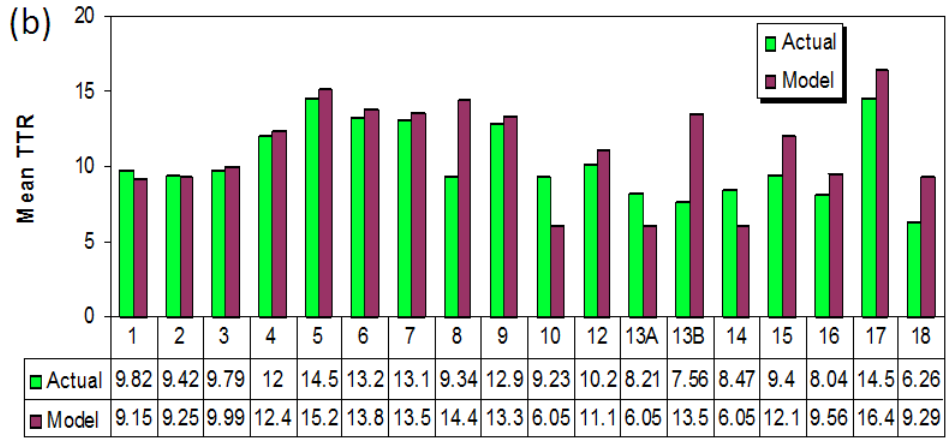

	1	2	3	4	5	6	7	8	9	10	12	13A	13B	14	15	16	17	18
Actual	9.82	9.42	9.79	12	14.5	13.2	13.1	9.34	12.9	9.23	10.2	8.21	7.56	8.47	9.4	8.04	14.5	6.26
Model	9.15	9.25	9.99	12.4	15.2	13.8	13.5	14.4	13.3	6.05	11.1	6.05	13.5	6.05	12.1	9.56	16.4	9.29

(b)

Figure 2.6: Comparison of (a) mean TBF and (b) mean TTR from the n-SDE model with those realized for various machines in an actual manufacturing system scenario

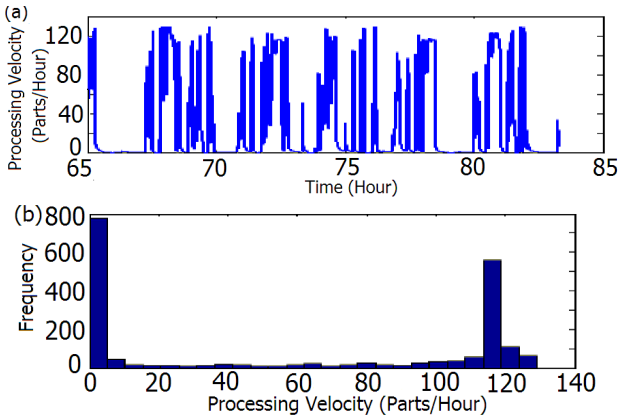

Figure 2.7: (a) Time-Portrait of processing velocity for Machine 2. (b) Histogram of the processing velocity for Machine 2

n-SDE model captures the traditional statistical quantifiers TBF and TTR. Interestingly, the exponential model was also found to capture the means, but the errors in capturing the standard deviations were $> 50\%$. Although an average of 24% and 28% deviations may appear high in comparison to the close agreement found for the other 10 machines, it may be noted that the traditional statistical metrics alone are not sufficient to capture the entire spectrum of dynamic behaviors; i.e., the effect of some of these deviations may not be high in terms of affecting the dynamics of throughputs.

Next, we investigated the extent to which this improvement in capturing the distributions of TTR and TBF translates into capturing the throughputs (or processing velocity in the case of fluid models). Fig. 2.7a shows the variations of processing velocity with time for Machine 2. It indicates that the model is able to capture the aperiodic nature (see Fig. 2.7a), and multimodal distributions (see Fig. 2.7b) of the processing velocities. These observations, shown in the context of Machine 2, are consistent across all the machines in the investigated assembly line segment. The maximum processing velocity or throughput rate for Machine 2 (obtained from the actual data) is 129 jobs/hr. This value is likely to occur, as is evident from Eqn. (2.34), whenever the upstream buffer is stocked, the down-

stream buffer is near-empty and the machine is up. Also, the machine was operating near its peak velocity of 129 jobs/hr for $< 2.5\%$ of the two-month-long observation period and at zero for roughly 28% of the time. The average jobs/hour (processing velocity) from the actual and the model are 37.29 jobs/hour and 39.50 jobs/hour, respectively. The deviation between the model and the actual is 5.59%, which makes them quite comparable. In contrast, the deviations with DES models that employ exponential TBF and TTR distributions exceeded 20% for most machines.

We also compared the n-SDE model simulation time with that of a DES model with exponential TBF and TTR distributions. Essentially, there is not much difference in computational effort between DES and n-SDE for simulating short time-scale TBF and TTR. However, for simulating large time-scale TBF and TTR, the fluid flow approximation of parts movement can significantly reduce computation time. Although the coupled dynamics of TTR and TBF considered in the n-SDE model can affect computation time, the simulations are initiated with "good" initial conditions that are in the basin of attraction (i.e., close to the steady state). The total computation time was reduced on average by about 25% with the use of the sigmoidal function per simulation of 100 time units using MATLAB-Simulink for every run over the simplest of DES simulation conducted in an efficient simulation environment (ARENA), with an added advantage of capturing the dependencies and multimodal distributions. Also, many of the simulations happen near the steady state, and the short-time events are separated out from the large time-scale, steady state, near-periodic breakdowns and repairs. Therefore, the almost ergodicity of the process was used to avoid a large number of replications.

Table 2.3: Comparison of recurrence quantifiers of TBF time-series realized in actual PFS data loggers with that from n-SDE and exponential models, respectively

Metric	TTR			TTR Error %	
	Actual	Model	Exp	Model	Exp
Recrate	39.94	24.7	0.04	38%	100%
Determinism	97.48	96.94	25.32	1%	74%
Laminarity	115	82	8	29%	90%
Entropy	5.55	4.89	1.84	12%	62%
Trend	0.04	0.02	0.01	50%	50%
Linemax	90.7	91.25	0	-1%	100%
Trap. time	30.72	25.73	NaN	16%	$\gg$100%

Table 2.4: Comparison of Recurrence Quantifiers of TTR time-series realized actual PFS data loggers with n-SDE and exponential models, respectively

Metric	TTR			TTR Error %	
	Actual	Model	Exp	Model	Exp
Recrate	43.24	21.78	0.13	50%	99%
Determinism	97.84	97.9	51.31	0%	48%
Laminarity	115	102	30	11%	71%
Entropy	5.71	4.65	2.38	19%	49%
Trend	0.04	0.04	0.01	0%	75%
Linemax	92.08	95.32	0	-4%	100%
Trap. time	33.01	29.1	NaN	12%	$\gg$100%

Additionally, the n-SDE model is more likely to capture the underlying nonlinear dynamic patterns such as recurrence [33] of actual operations. Tables 3 and 4 suggest that most of the recurrence quantifiers [33], that measure the extent of dependencies among TBF and TTR processes, estimated from n-SDE model are much closer to those estimated from actual data compared to those from an exponential model. Further investigations are

necessary to develop this approach for effective (faster and more accurate) fitting of the downtime distributions and their interrelationships.

2.5 Concluding remarks

In this chapter, we have investigated the application of piecewise affine (constant) differential equation models to capture the coupled dynamics of degradation and restoration processes inherent to industrial machines and other real-world mechanical systems. The piecewise affine structure and the order of the differential equations provide one of the simplest means to capture the salient dynamic behaviors. The model admits a solution that mimics the fairly regular (periodic) long-term breakdown and repair intervals and the highly right skewed short-term breakdown repair intervals. We have provided results on the local stability and the basin of attraction for a solution of this class of piecewise-affine differential equation models. Under the conditions where periodic solutions are locally stable, the trajectories are found to merge with the periodic orbits within five crossings across the switching surfaces. Furthermore, the existence of a fairly broad basin of attraction enhances the tolerance for lower precision in numerical solvers used for integrating affine equations, i.e., numerical solutions are less prone to finite precision errors and are robust to the tolerance specifications used in the integration routines, the specification of the initial conditions, and finite perturbations to the model parameters. The numerical studies conducted to verify these theoretical results indicate that the model, parametrized to meet the stability and the perturbation criteria specified in the theoretical results, can capture the multimodal behavior of data from a real-world manufacturing system. The short-time TBF and TTR distributions exhibit right-skewed exponential-like characteristics with ν values fairly consistent with theoretical results.

We have also conducted a case study to integrate the above model into an assembly line segment. Sigmoidal function theory is used to remove discontinuities resulting from

the onset and offset of breakdown-restored states. These discontinuities are known to introduce instabilities in the numerical integration routines used to solve the model. The n-SDE modeling approach was tested on an 18 station assembly line segment in Matlab's Simulink environment. The results were compared with those from a real-world production line observed during a one-year period. The results indicate that the n-SDE model can capture the marginal distributions of TBF and TTR better than commonly used exponential distribution models. More pertinently, the model is also able to capture the salient trends in the assembly line dynamics, including the relative throughput losses due to blocking, starving, and machine breakdown, as well as TBF-TTR interactions. An extensive set of metrics was used to compare the statistical and nonlinear dynamical behaviors gathered from the models vs. actual assembly line data. Collectively, these results allude to a straightforward approach to parametrize piecewise affine differential equation models with random perturbations to capture the complex degradation and repair dynamics of real-world engineering systems. Our ongoing work is focused on deriving similar results as in Theorems 1-6 for sigmoidal functions and using piecewise nonlinear models with polynomial structures to capture additional nuances of degradation and restoration dynamics in engineering systems.

3. COUPLED DYNAMICS MODELING AT NETWORK LEVEL: INFERRING SPARSE NETWORKS FOR NOISY TRANSIENT PROCESSES[1]

In this chapter, we are interested in modeling the coupled dynamics among different processes using network representation. Our approach is based on modifying ND, silencing, and MRA methods to account for sparsity, transients, noise, and high dimensionality issues. Specifically, we have investigated a sparse regression (henceforth referred to as the ℓ_1-min) formulation to recover the structure of dynamic networks from noisy data gathered under transient conditions. Our main contribution is in providing a theoretical bound on the constraints of the ℓ_1-min formulation and providing stable numerical procedures that overcome effects of nonlinear couplings in large interconnected processes, availability of only a small sample of short time series ensembles, and inaccuracies in estimating noise levels. These bounds mitigate tedious trial and error procedures employed customarily as part of ℓ_1-min implementations [34–37]. The theoretical results and subsequent experimental studies suggest that the present ℓ_1-min approach is more robust to noise compared to the contemporary dynamic Bayesian network [38–43] as well as NDs [44–46]. It is shown that up to 5 orders of magnitude reduction in the inference error are possible from the present approach, leading to a more accurate inference of the network structure for complex real world networks.

[1]Reprinted with permission "Inferring sparse networks for noisy transient processes" by Tran, Hoang M and Bukkapatnam, Satish TS, 2016, *Scientific Reports* 6 (2016), pp. 21963, Copyright [2016] by Macmillan Publishers Limited.

3.1 Backgrounds

Towards a more formal treatment, we define a real world system as high dimensional coupled differential equation of the form

$$\frac{d\boldsymbol{x}}{dt} = \boldsymbol{f}(\boldsymbol{x}, \boldsymbol{p}), \tag{3.1}$$

or

$$\boldsymbol{x}(t) = \boldsymbol{\Phi}(t, \boldsymbol{x}(\tau)), \tag{3.2}$$

where $\boldsymbol{x} \in M \subset \mathbb{R}^n$ is a state vector, $\boldsymbol{p}$ is the parameter vector, $\boldsymbol{x}(\tau)$ is an initial condition. As noted in the foregoing, such dynamics can also be represented in form of a network [47] shown in Fig. 3.1a, where the node i represents the state variable x_i and a directed arc represents the existence and the strength of the coupling (direct influence) s_{ij} between node i and node j. In this context, the direct influence $s_{ij}(t)$ of node j on node i around a certain point $\boldsymbol{x}$ in the state space defined in Eq. (3.1) can be expressed as

$$s_{ij}(t) \triangleq \frac{\partial x_i}{\partial x_j(\tau)} = \frac{\partial \Phi_i(t, \boldsymbol{x}(\tau))}{\partial x_j(\tau)}. \tag{3.3}$$

It may be noted that, a node j is connected to a node i at time t if $s_{ij}(t) \neq 0$. Hence,

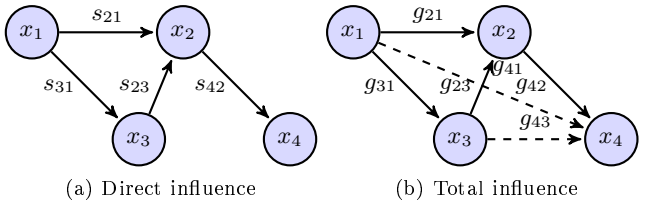

(a) Direct influence (b) Total influence

Figure 3.1: Illustration of direct and total influence. The total influences in b) are the accumulation of the influences transited through all paths in a)

$S(t) = (s_{ij}(t))$ captures the physical structure of the dynamical system (3.1) at time t. In practice, $S(t)$ needs to be inferred from the measurements of the total influence $g_{ij}(t)$ between every pair of nodes [44, 45] or estimated from time series outputs of the dynamic system gathered under transient conditions [2]. The total influence $g_{ij}(t)$ is the sum of the direct influence of node j on node i and all indirect influences from node j to node i through other nodes connecting to both of them (see Fig. 3.1b). For example, total influence from $1 \to 4$, $g_{41}(t)$ is the sum of indirect influences along the paths $1 \to 3 \to 2 \to 4$ and $1 \to 2 \to 4$, or $g_{41}(t) = s_{31}(t)s_{23}(t)s_{42}(t) + s_{21}(t)s_{42}(t)$. In other words, the total influence that node j has on node i around a certain point $\boldsymbol{x}$ on the state space defined in Eq. (3.1) is defined recursively as

$$g_{ij}(t) \triangleq \frac{dx_i(t)}{dx_j(\tau)} = \frac{d\Phi_i(t, \boldsymbol{x}(\tau))}{dx_j(\tau)} \tag{3.4}$$

$$= \frac{\partial \Phi_i(t, \boldsymbol{x}(\tau))}{\partial x_j(\tau)} + \sum_{k \neq j} \frac{\partial \Phi_i(t, \boldsymbol{x}(\tau))}{\partial x_k(\tau)} \frac{dx_k(t)}{dx_j(\tau)} \tag{3.5}$$

$$= s_{ij}(t) + \sum_{k \neq j} s_{ik}(t) g_{kj}(t), \tag{3.6}$$

which is similar to the expression noted in in Barzel and Barabási [45]. Conventionally, under stationarity assumptions, $g_{ij}(t)$ can be approximated using similarity measures, such as correlation and mutual information [8] estimated from raw samples of time series. The direct and total influence matrices are related at every time t by the following equation:

$$S(t)B(t) - C(t) = 0, \tag{3.7}$$

where $B(t)$ and $C(t)$ are functions (defined depending on the context) of $S(t)$ and $G(t)$, respectively. Pertinently, when the underlying dynamical system is linear and time-invariant, $S(t)$ and $G(t)$ do not depend on time. Eq. (3.7) generalizes previous network deconvo-

lution formulations as follows: for Feizi *et al.* [44], $B(t) = (I + G), C(t) = G$, for Barzel and Barabási [45] $B(t) = G, C(t) = G - I + \mathscr{D}(SG)$, and for Sontag *et al.* [2], $B(t) = R(t), C(t) = \Gamma(t)$, where $R_{ij}(t) = \partial x_i(t, \boldsymbol{p})/\partial p_j; \Gamma_{ij}(t) = \partial R_{ij}(t)/\partial t$. For simplicity of expressions, we use henceforth S, B and C instead of $S(t), B(t)$ and $C(t)$ in this subsection. The "true" network structure S^0 can be estimated by solving the following ℓ_1-min formulation:

$$S^* = \arg\min_S \|S\|_1 \text{ s.t. } \|SB - C\|_F \leq \mathcal{E}, \tag{3.8}$$

where $\|S\|_1 = \sum_{i,j} |s_{ij}|$, and $\mathcal{E}$ is the allowable perturbation that captures the effects of noise in the measured data. We note that in the absence of noise, this formulation is equivalent to ND and MRA. In the following sections we present two alternative ℓ_1-min formulations for direct influence inference. The first formulation presented in Eqs. (3.9, 3.10) addresses the estimation of s_{ij} for real world scenarios when the total influence g_{ij} is directly measurable (e.g., based on the strengths of co-excitations), and the second formulation Eqs. (3.33, 3.34) addresses the inference of the network structure (i.e., determine all node pairs where $s_{ij}(t) = 0 \; \forall t$) under one of the most generic scenarios of using multiple ensembles of time series realizations of the state variables, collected under noisy and transient conditions with different parameter settings. It may be noted that inferring the network structure under such generic conditions has not been investigated to date.

3.2 Network inference when total influence matrix is available

For the case where the measurements of total influence matrix G are provided [44], the relaxed ℓ_1-min formulation can be written as

$$\min ||S||_1 \text{ s.t. } ||S(G + I) - G||_F \leq \mathcal{E}, \tag{3.9}$$

or in vector form as

$$\min_{\boldsymbol{s}_i} ||\boldsymbol{s}_i||_1 \text{ s.t. } ||(G+I)^T\boldsymbol{s}_i - \boldsymbol{g}_i||_2 \leq \varepsilon_i,\ \forall i, \tag{3.10}$$

where $\boldsymbol{g}_i$ is the i^{th} column of G. In order to solve for an accurate estimate of S^0 from Eqs. (3.9) or (3.10) using standard solvers [48, 49], estimation of $\mathcal{E}$ and ε_i are crucial. Specifically, when noisy measurements of the total influence matrix differ from the "true" total influence as $G = G^0 + \Delta G$, the estimated direct influence matrix differs from the true direct influence matrix as $S = S^0 + \Delta S$, and

$$(S^0 + \Delta S)(G+I) = G \tag{3.11}$$

$$\Rightarrow S^0(G+I) - G = -\Delta S G - \Delta S. \tag{3.12}$$

The quantity $||\Delta S G + \Delta S||_F$ is called total perturbation. In vector form, $(||\Delta G \boldsymbol{s}_i^0||_2 + ||\boldsymbol{g}_i - \boldsymbol{g}_i^0||_2)$ can represent the total perturbation for computing row i of S^0. By establishing strong lower bounds for total perturbation and/or $||\Delta S||_F$, we can set the values of $\mathcal{E}$ and ε_i for effective network inference. The two results pertaining to the bound on $||\Delta S||_F$ are represented in the following lemma.

Lemma 1. *$||\Delta S||_F$ can be bounded as*

$$||\Delta S||_F \leq \gamma + O(\delta^2 + \gamma^2 + \delta\gamma), \tag{3.13}$$

according to Feizi et al. [44] where γ and δ are the largest eigenvalues of ΔG and G, respectively satisfy $\gamma \ll 1, \delta < 1$ or

$$||\Delta S||_F \leq \frac{||\Delta G||_F}{(1 - ||G||_F - ||\Delta G||_F)(1 - ||G||_F)}, \tag{3.14}$$

provided

$$1 - ||G||_F - ||\Delta G||_F > 0. \tag{3.15}$$

Proof. From (3.11), it follows that

$$\begin{aligned}
G^0 + \Delta G &= S^0 + S^0G^0 + S^0\Delta G \\
&\quad +\Delta S + \Delta SG^0 + \Delta S\Delta G \\
\Leftrightarrow \Delta G &= S^0\Delta G + \Delta S + \Delta SG^0 + \Delta S\Delta G \\
\Leftrightarrow \Delta G &= G^0(I + G^0)^{-1}\Delta G + \Delta S(I + G^0 + \Delta G) \\
\Rightarrow \Delta S &= ((I + G^0)(I + G^0)^{-1} - G^0(I + G^0)^{-1}) \\
&\quad \Delta G(I + G^0 + \Delta G)^{-1} \\
\Rightarrow \Delta S &= (I + G^0)^{-1}\Delta G(I + G^0 + \Delta G)^{-1} \\
\Rightarrow ||\Delta S||_F &= ||(I + G^0)^{-1}\Delta G(I + G)^{-1}||_F
\end{aligned}$$

$$\begin{aligned}
&= ||(I - (-G^0))^{-1}\Delta G(I - (-G))^{-1}||_F \\
&\overset{a}{\leq} ||(I - (-G^0))^{-1}||_F||\Delta G||_F||(I - (-G))^{-1}||_F \\
&\overset{b}{\leq} \frac{1}{1 - ||(-G)||_F}||\Delta G||_F\frac{1}{1 - ||G||_F} \\
&\overset{c}{\leq} \frac{1}{1 - ||G||_F - ||\Delta G||_F}||\Delta G||_F\frac{1}{1 - ||G||_F}
\end{aligned}$$

We have (a) because of the sub-multiplicative property $||AB||_F \leq ||A||_F||B||_F$. for (b) to hold:

$$||G^0||_F < 1 \tag{3.16}$$

$$||-G||_F < 1 \tag{3.17}$$

Because $||G^0||_F = ||G - \Delta G||_F \leq ||G||_F + ||\Delta G||_F$, sufficient condition for (3.16,3.17) to hold is $||G||_F + ||\Delta G||_F \leq 1$.

We have (c) because

$$\begin{aligned} 1 - ||G^0||_F &\geq 1 - ||G||_F - ||\Delta G||_F > 0 \\ \Rightarrow \frac{1}{1 - ||G^0||_F} &\leq \frac{1}{1 - ||G||_F - ||\Delta G||_F} \end{aligned}$$

Therefore, we have (3.14). □

Note that the restriction (3.15) is reasonable as G can be linearly scaled [44] such that $||G||_F$ is small enough to qualify Eq. (3.15). The following theorem provides bounds on total perturbation based on this lemma.

Theorem 1. *ε_i and $\mathcal{E}$ can be bounded as follows*

$$\varepsilon_i = (||\Delta G \boldsymbol{s}_i^0||_2 + ||\boldsymbol{g}_i - \boldsymbol{g}_i^0||_2)^2 \leq 2(||\boldsymbol{g}_i - \boldsymbol{g}_i^0||_2^2 + ||\Delta G||_F \frac{1}{\sqrt{1-\delta_K}}(||\boldsymbol{g}_i||_2 + ||\boldsymbol{g}_i - \boldsymbol{g}_i^0||_2)^2), \quad (3.18)$$

$$\mathcal{E} = ||\Delta S G + \Delta S||_F \approx \mathcal{E}^{(1)} = (1 + ||G||_F)\gamma \quad (3.19)$$

and

$$\mathcal{E} = ||\Delta S G + \Delta S||_F \leq \mathcal{E}^{(2)} \quad (3.20)$$

where $\mathcal{E}^{(2)} = (1 + ||G||_F)\frac{||\Delta G||_F}{(1-||G||_F - ||\Delta G||_F)(1-||G||_F)}$.

Proof. Apply the Lemma 2 of Herman & Strohmer [50] to $\Phi^0 = G^0 + I$ and K - sparse vector $\boldsymbol{s}_i^0$, we have

$$||(G^0 + I)\boldsymbol{s}_i^0||_2 \geq \sqrt{1 - \delta_K}||\boldsymbol{s}_i^0||_2.$$

Also, by applying the Cauchy Schwarz inequality, we have $||\Delta G \boldsymbol{s}_i^0||_2 \leq ||\Delta G||_F ||\boldsymbol{s}_i^0||_2$.

Therefore,

$$\begin{aligned} \frac{||\Delta G \boldsymbol{s}_i^0||_2}{||(G^0+I)\boldsymbol{s}_i^0||_2} &\leq \frac{||\Delta G||_F ||\boldsymbol{s}_i^0||_2}{\sqrt{1-\delta_K}||\boldsymbol{s}_i^0||_2} \\ \Rightarrow \frac{||\Delta G \boldsymbol{s}_i^0||_2}{||(G^0+I)\boldsymbol{s}_i^0||_2} &\leq \frac{||\Delta G||_F}{\sqrt{1-\delta_K}} \\ \Rightarrow ||\Delta G \boldsymbol{s}_i^0||_2 &\leq \frac{||\Delta G||_F}{\sqrt{1-\delta_K}}||\boldsymbol{g}_i^0||_2 \end{aligned}$$

As a result,

$$\begin{aligned} 2(||\Delta G \boldsymbol{s}_i^0||_2^2 + ||\boldsymbol{g}_i - \boldsymbol{g}_i^0||_2^2) &\leq 2\left(\left(\frac{||\Delta G||_F}{\sqrt{1-\delta_K}}||\boldsymbol{g}_i^0||_2\right)^2 + ||\boldsymbol{g}_i - \boldsymbol{g}_i^0||_2^2\right) \\ &\leq 2\left(\left(\frac{||\Delta G||_F}{\sqrt{1-\delta_K}}(||\boldsymbol{g}_i||_2 + ||\delta \boldsymbol{g}_i||_2\right)^2 + ||\boldsymbol{g}_i - \boldsymbol{g}_i^0||_2^2\right) \end{aligned}$$

On the other hand,

$$2(||\Delta G \boldsymbol{s}_i^0||_2^2 + ||\boldsymbol{g}_i - \boldsymbol{g}_i^0||_2^2) \geq (||\Delta G \boldsymbol{s}_i^0||_2 + ||\boldsymbol{g}_i - \boldsymbol{g}_i^0||_2)^2$$

Therefore, we have (3.18).

Proof of (3.19):

$$\begin{aligned} ||\Delta S G + \Delta S||_F &\leq ||\Delta S G||_F + ||\Delta S||_F \\ &\leq ||\Delta S||_F ||G||_F + ||\Delta S||_F \\ &\approx \gamma(1 + ||G||_F) \end{aligned}$$

as

$$||\Delta S||_F \approx \gamma, \tag{3.21}$$

according to [45].

Proof of (3.20):

$$\begin{aligned} ||\Delta SG + \Delta S||_F &\leq ||\Delta S||_F||G||_F + ||\Delta S||_F \\ &\leq (1 + ||G||_F)\frac{||\Delta G||_F}{(1 - ||G||_F - ||\Delta G||_F)(1 - ||G||_F)} \end{aligned}$$

□

Next we show that S^* obtained based on the foregoing results is a good approximation of S^0.

Theorem 2. *[50] Assume that $\boldsymbol{s}_i^0$ is the sparsest solution of the Problem (3.10) and*

$$\delta_{2K} < \frac{\sqrt{2}}{(1 + \varepsilon_{\Phi^0}^{(2K)})^2} - 1,$$

there exists positive constants C_0, C_1 such that

$$||\boldsymbol{s}_i^* - \boldsymbol{s}_i^0||_2 \leq \frac{C_0}{\sqrt{K}}||\boldsymbol{s}_i^0 - \boldsymbol{s}_i^{(K)}||_2 + C_1\varepsilon_i \tag{3.22}$$

where $\boldsymbol{s}_i^*$ is solution of the ℓ_1-min problem (3.10).

Proof. This is a direct application of Theorem 2 in Herman & Strohmer [50] with $\boldsymbol{x} = \boldsymbol{s}_i^0, \hat{\boldsymbol{b}} = \boldsymbol{g}_i, \boldsymbol{z}^* = \boldsymbol{s}_i^*, \hat{A} = G + I$. Note that C_0, C_1 are constants depending on $\varepsilon_{\Phi^0}^{(2K)}$. □

When the true solution $\boldsymbol{s}_i^0$ has at most K nonzero elements, the result Eq. (3.22) can be further simplified as follows.

Corollary 2. *When $\boldsymbol{s}_i^0$ has at most K nonzero elements,*

$$||\boldsymbol{s}_i^* - \boldsymbol{s}_i^0||_2 \leq C_1\varepsilon_i. \tag{3.23}$$

Proof. When $\boldsymbol{s}_i^0$ is a K - sparse vector, $\boldsymbol{s}_i^0 = \boldsymbol{s}_i^{(K)}$. Eq. (3.22) becomes Eq. (3.23). □

The assumption in this corollary is reasonable since most of real world networks tend to be sparse. The results in Eqs. (3.22,3.23) are formulated for each row of S^0. In terms of the whole matrix, the robustness of computing S^0 can be guaranteed by the following theorem.

Theorem 3. *Let S^* be the solution of the ℓ_1-min formulation (3.9). The error when approximating S^0 by S^* is bounded by*

$$||S^* - S^0||_F^2 \leq C_1 \mathcal{E} \tag{3.24}$$

where $\mathcal{E}$ is bounded as $\mathcal{E} \leq 2\left(\frac{1}{1-\delta_K}||G^0||_F^2 + 1\right)||\Delta G||_F^2$.

Proof. Apply the Corollary 2 to the Problem 3.10 with $\varepsilon_i = 2\left(||\Delta G||_F \frac{1}{\sqrt{1-\delta_K}}||\boldsymbol{g}_i^0||_2\right)^2 + 2||\boldsymbol{g}_i - \boldsymbol{g}_i^0||_2^2$ we have

$$\begin{aligned}
||\boldsymbol{s}_i^* - \boldsymbol{s}_i^0||_2^2 &\leq 2C_1\left(||\Delta G||_F \frac{1}{\sqrt{1-\delta_K}}||\boldsymbol{g}_i^0||_2\right)^2 + 2C_1||\boldsymbol{g}_i - \boldsymbol{g}_i^0||_2^2 \\
\Rightarrow \sum_{i=1}^n ||\boldsymbol{s}_i^* - \boldsymbol{s}_i^0||_2^2 &\leq 2C_1 \sum_{i=1}^n \left(||\Delta G||_F \frac{1}{\sqrt{1-\delta_K}}||\boldsymbol{g}_i^0||_2\right)^2 + 2C_1 \sum_{i=1}^n ||\boldsymbol{g}_i - \boldsymbol{g}_i^0||_2^2 \\
&= 2C_1\left(||\Delta G||_F \frac{1}{\sqrt{1-\delta_K}}\right)^2 \sum_{i=1}^n \left(||\boldsymbol{g}_i^0||_2\right)^2 + 2C_1 \sum_{i=1}^n ||\boldsymbol{g}_i - \boldsymbol{g}_i^0||_2^2 \\
\Rightarrow ||S^* - S^0||_F^2 &\leq 2C_1\left(||\Delta G||_F \frac{1}{\sqrt{1-\delta_K}}\right)^2 ||G^0||_F^2 + 2C_1||\Delta G||_F^2.
\end{aligned}$$

□

Theorems 8, 3 and Corollary 2 taken together guarantee that inference error when estimating S^0 by S^* is at most linear with total perturbation noise. This observation is further verified using numerical investigations presented in the first case study.

The bounds on $\mathcal{E}$ and ε_i are as follows (See Theorem 1 in Supplementary Information):

$$\mathcal{E} \approx \mathcal{E}^{(1)} = (1 + ||G||_F)\gamma, \tag{3.25}$$

$$\mathcal{E} \leq \mathcal{E}^{(2)} = (1 + ||G||_F)\frac{||\Delta G||_F}{(1 - ||G||_F - ||\Delta G||_F)(1 - ||G||_F)}, \tag{3.26}$$

$$\varepsilon_i \leq 2(||\boldsymbol{g}_i - \boldsymbol{g}_i^0||_2^2 + ||\Delta G||_F \frac{1}{\sqrt{1 - \delta_K}}(||\boldsymbol{g}_i||_2 + ||\boldsymbol{g}_i - \boldsymbol{g}_i^0||_2)^2), \tag{3.27}$$

where γ is the largest eigenvalue of ΔG, δ_K is the restricted isometry constant [50] and $||.||_F$ is the Frobenius norm of a matrix. By employing these bounds, we can set the values of $\mathcal{E}$ and ε_i for effective network inference. As subsequent numerical investigations indicate, the performance of the method does not degrade significantly due to the presence of noise, and this is the major advantage of the present approach. It may be noted that our method is designed to provide the sparsest network structure that replicates the measured total influence G within a bound (specified in terms of the allowable total perturbation). This is very important because only a small set of noisy observations are available, for most real world applications. For example, in the case of genetic regulatory networks, only a subset of dynamic regimes (i.e. marked by the active degrees of freedom) of the underlying process are captured. Therefore, identification of true network structure would never be guaranteed by any approach, and among the network structures that can replicate the observed total influence within a specified bound, the sparsest network would be of the most interest. Although sparser than the network derived by ND, ℓ_1-min derived structure might be adequate to uncover the total dynamic couplings of the process captured in the observed data

In real world scenarios, ΔG is not always known. Overestimation of ΔG can lead to network structures that are sparser than the original. However, we show that the effects of under-estimation of noise can be alleviated to a great extent. When noise level is unknown

but multiple realizations of the noisy measurements of G are available, it is possible to further reduce the inference error by combining the estimates with different realizations of G as $\bar{S}^{(N)} = \frac{1}{N}\sum_{r=1}^{N}\hat{S}^{(r)}$

Proposition 1. *Let $\hat{G}^{(1)}, ..., \hat{G}^{(N)}$ be N different measurements or estimates of the total influence matrix G^0. Let $\hat{S}^{(r)}$ be the direct influence matrix computed from $\hat{G}^{(r)}$ using different methods, including ND and ℓ_1-min approach with different bounds. If $Var(\hat{S}^{(r)})$ are bounded then $E||\bar{S}^{(N)} - S^0||^2 \to 0$ as $N \to \infty$, where $\bar{S}^{(N)} = \frac{1}{N}\sum_{r=1}^{N}\hat{S}^{(r)}$.*

Proof. Under perfect reconstruction per ND, $\hat{S} = S^0 + \Delta S^*$ satisfies

$$\hat{S}(G^0 + \Delta G + I) = (G^0 + \Delta G)$$

For the r^{th} realization of ΔG, we have

$$\begin{aligned} \hat{S}_r(G^0 + \Delta G_r + I) &= (G^0 + \Delta G_r) \\ \Rightarrow \hat{S}_r &= (G^0 + \Delta G_r)(G^0 + \Delta G_r + I)^{-1} \end{aligned}$$

As ΔG_r are independent, $\hat{S}_r$ are independent.

$$\begin{aligned} Var(\bar{S}^{(N)} - S^0) &= Var(\frac{\sum_{r=1}^{N}\hat{S}_r}{N} - S^0) \\ &= Var(\frac{\sum_{r=1}^{N}(\hat{S}_r - S^0)}{N}) \\ &= \frac{1}{N^2}Var(\sum_{r=1}^{N}(\hat{S}_r - S^0)) \\ &= \frac{1}{N^2}\sum_{r=1}^{N}Var(\hat{S}_r - S^0) \text{ (As } \hat{S}_r - S^0 \text{ are independent)} \end{aligned}$$

If $Var(\hat{S}_r - S^0)$ is bounded by some constant C for all r,

$$Var(\bar{S}^{(N)} - S^0) \leq \frac{1}{N^2} \sum_{r=1}^{N} C = \frac{C}{N} \to 0 \text{ as } N \to \infty$$

□

This result assumes that $Var(\hat{S}^{(r)})$ is bounded. However, it may be noted that even if $Var(\hat{S}^{(r)})$ is arbitrarily large we find that $\bar{S}^{(N)}$ is at least as good as $\hat{S}^{(r)}$. This averaging procedure allows us to improve the network inference accuracy when multiple measurements of the total influence matrix are available. For example, when the network structure does not change significantly as the system approaches a steady state, the total influence matrices can be measured multiple times, each corresponds to one time window.

3.3 Network inference when the time series under transient conditions are available (total influence matrix not given)

In practice, g_{ij} are often estimated using convenient similarity measures such as correlation or mutual information between the time series $x_i(t)$ and $x_j(t)$ of the nodes i, j as stated in the foregoing section. These estimations have a very low accuracy due to non-stationaries (transient), low sampling rates and sample size limitation; and can not capture the total influence in the system. Also, in most real world applications, only finite samples of time series $\boldsymbol{x}(t)$ are available, and the present NDs can not be employed in these scenarios. To overcome these drawbacks, we have adapted an approach to estimate the direct influence based on multiple time series ensembles obtained by perturbing parameters of the dynamical system Eq. (3.1) [2]. We first modify the perturbation procedure proposed by Sontag *et al*. [2] to make it more robust to numerical error then further improve the accuracy of network inference by introducing a sparse regression formulation and the averaging scheme.

3.3.1 A robust perturbation procedure

According to Sontag *et al.* [2], $s_{ij}(t) = [\frac{\partial f_i(\boldsymbol{x},\boldsymbol{p})}{\partial x_j}]_{i,j=1..n}$ can be derived from the following equation:

$$\Gamma(t) = S(t)R(t), \tag{3.28}$$

where

$$R_{ij}(t) = \frac{\partial x_i}{\partial p_j} \approx \frac{x_i(t, p_j + \Delta p_j) - x_i(t, p_j)}{\Delta p_j}, \Gamma_{ij}(t) = \frac{\partial \dot{x}_i}{\partial p_j} \approx \frac{R_{ij}(t + \Delta t) - R_{ij}(t)}{\Delta t}, \tag{3.29}$$

and

$$i = 1..n, p_k \in P_i = \{p_k \in \boldsymbol{p} : \partial f_i / \partial p_k(\boldsymbol{x}, \boldsymbol{p}) = 0\}. \tag{3.30}$$

Note that Γ plays the role of the total influence matrix G in the previous section. To compute the row i of the matrix S, the parameters p_j to be perturbed are chosen such that $p_j \in P_i$ [2]. As a consequence, changes in p_j indirectly affect x_i, and $\frac{dx_i}{dp_j}$ are much smaller than $\frac{dx_k}{dp_j}$, for $k \neq i$. As a result, the i^{th} column $\left(\frac{dx_i}{dp_j}\right)_{n\times 1}$ in the matrix $\left(\frac{dx_k}{dp_j}\right)_{n\times n}$ is much smaller (2 orders of magnitude smaller as in the Table 3.1 for the network studied in case study 1) compared to other columns when $p_j \in P_i$. A numerical issue this poses can be understood based on the following linear system of equations

$$A\boldsymbol{u} = \boldsymbol{b}.$$

Here, the sensitivity of solution $\boldsymbol{u}$ to the change in A can be quantified as follows [51]

$$\frac{\partial u_i}{\partial a_{jk}} = -c_{ij} \sum_l c_{kl} b_l,$$

where $C = A^{-1}$.Whenever A contains a j column such that $||a_{\cdot j}|| \ll ||a_{\cdot k}||$, $\forall k \neq j$, C

	$r_{.1}$	$r_{.2}$	$r_{.2}$	$r_{.2}$	$r_{.2}$	$r_{.2}$	$r_{.2}$	$\max \lvert r_{.j} \rvert$
$r_{1.}$	-2.868e-4	-7.284e-5	-3.106e-4	-1.578e-4	2.443-e4	-8.315e-5	-4.896e-4	**0.0005**
$r_{2.}$	1.160e-4	0.1050	-4.261e-4	-1.803e-4	6.490e-4	2.261e-4	-2.379e-4	***0.1050***
$r_{3.}$	-1.136e-4	-2.658e-4	0.1179	-2.766e-4	1.370e-4	-2.524e-4	2.776e-4	***0.1179***
$r_{4.}$	-4.431e-4	-4.543e-4	-4.138e-4	0.0961	6.824e-4	6.710e-5	1.609e-4	***0.0961***
$r_{5.}$	-2.397e-4	-4.439e-4	-1.225e-4	-7.024e-4	0.1100	3.256e-4	2.069e-4	***0.1100***
$r_{6.}$	4.053e-4	-3.773e-4	-2.577e-4	-5.065e-5	0.0012	0.1195	4.481e-4	***0.1195***
$r_{7.}$	-1.030e-4	3.312e-5	-2.900e-4	-5.258e-5	0.0100	-1.651e-4	0.0820	***0.0820***

Table 3.1: The matrix R for computing the first row of S is estimated using Sontag *et al.* [2]'s perturbation procedure. The first row/column of R is two orders of magnitude smaller than others, which presents major numerical issues for inferring structures of large networks.

contains a row i such that $||c_{i.}|| \gg ||c_{r.}||, \forall r \neq i$. As a consequence, $\frac{\partial u_i}{\partial a_{jk}}$ becomes several magnitudes larger than other rows. Therefore, the perturbation procedure proposed by Sontag *et al.* [2] is very unrobust to noise or numerical error in x_is.

The following modification to the perturbation procedure addresses the aforementioned issue. Consider the case when $\dot{x}_i$ depends linearly on x_i as in the following system [52]:

$$\dot{x}_i = p_i x_i + \sum_{j=1, j\neq i}^{n} s_{ij}^0 \frac{x_j}{1+x_j}.$$

This system describes popular biochemical reactions when the activity of a chemical species is inhibited by its own concentration [53, 54]. To compute the i^{th} row of the Jacobian, the parameters p_i is also perturbed. Note that

$$\frac{\partial \dot{x}_i}{\partial p_i} = x_i + p_i \frac{\partial x_i}{\partial p_i} + \sum_{j=1, j\neq i}^{n} \frac{\partial f_i(\boldsymbol{x}, \boldsymbol{p})}{\partial x_j} \frac{\partial x_j}{\partial p_i}, \tag{3.31}$$

or

$$\frac{\partial \dot{x}_i}{\partial p_i} - x_i = \sum_{j=1, j\neq i}^{n} \frac{\partial x_j}{\partial p_j} \frac{\partial f_i(\boldsymbol{x}, \boldsymbol{p}_i)}{\partial x_j}, \frac{\partial f_i(\boldsymbol{x}, \boldsymbol{p}_i)}{\partial x_i} = p_i. \tag{3.32}$$

The remaining parameters are perturbed as in Eqs. (3.29, 3.30). Therefore, to compute $\frac{\partial f_i(\boldsymbol{x},\boldsymbol{p}_i)}{\partial x_k}$, we can solve the system of equations (3.28) with

$$P_{ii}(t) = \frac{\partial \dot{x}_i}{\partial p_i} - x_i, R_{ii}(t) = \frac{\partial x_i}{\partial p_i}$$

and other P_{ij}s, R_{ij}s are defined as in (3.29, 3.30).

3.3.2 A robust network identification approach

In addition to the perturbation procedure proposed in Eqs. (3.29-4.15), we present a method to solve Eq. (3.28) that is more robust to the presence of noise. In the present context, the ℓ_1-min formulation of Eq. (3.28) takes the following form:

$$\min ||S||_1 \text{ s.t } ||\Gamma - SR||_F \leq \mathcal{E}, \tag{3.33}$$

or

$$\min ||\boldsymbol{s}_i||_1 \text{ s.t } ||\Gamma_{ik}(t) - \sum_{l=1}^{n} R_{lk}(t)s_{il}(t)|| \leq \varepsilon_i, \forall i, \quad \forall k : p_k \in P_i. \tag{3.34}$$

As noted in the foregoing section, estimation of $\mathcal{E}$ and ε_i based on the noise levels when measuring $\boldsymbol{x}(t)$ is essential to ensure that the solution to Eq. (3.33) serves as a viable estimator of the "true" direct influence S^0.

Lemma 2.

$$(\Delta R)_{ik}(t) = (e_{ik}^{(1)}(t) - e_{ik}^{(2)}(t))/\Delta p_k$$
$$(\Delta \Gamma)_{ik}(t) = \frac{[(e_{ik}^{(1)}(t+\Delta t) - e_{ik}^{(2)}(t+\Delta t)) - (e_{ik}^{(1)}(t) - e_{ik}^{(2)}(t))]}{\Delta t \Delta p_k}$$

where $e_{ik}^{(1)}(t), e_{ik}^{(2)}(t)$ *are the errors incurred when measuring* $x_i^0(t, p_k)$, $x_i^0(t, p_k + \Delta p_k)$, *respectively.*

Proof.

$$
\begin{aligned}
R_{ik}^0(t) &\approx (x_i^0(t, p_k + \Delta p_k) - x_i^0(t, p_k))/\Delta p_k \qquad (3.35)\\
R_{ik}(t) &\approx ((x_i^0(t, p_k + \Delta p_k) + e_{ik}^{(2)}(t)) - (x_i^0(t, p_k) + e_{ik}^{(1)}(t)))/\Delta p_k \\
&= ((x_i^0(t, p_k + \Delta p_k) - x_i^0(t, p_k)) + (e_{ik}^{(2)}(t) - e_{ik}^{(1)}(t)))/\Delta p_k \\
&\approx R_{ik}^0(t) + (e_{ik}^{(2)}(t) - e_{ik}^{(1)}(t))/\Delta p_k \\
\Delta R_{ik}(t) &= (e_{ik}^{(2)}(t) - e_{ik}^{(1)}(t))/\Delta p_k
\end{aligned}
$$

$$
\begin{aligned}
\Gamma_{ik}(t) &\approx (R_{ik}(t + \Delta t) - R_{ik}(t))/\Delta t \\
&= \left[R_{ik}^0(t + \Delta t) + (e_{ik}^{(2)}(t + \Delta t) - e_{ik}^{(1)}(t + \Delta t))/\Delta p_k\right]/\Delta t - \\
&\quad \left[R_{ik}^0(t) + (e_{ik}^{(2)}(t) - e_{ik}^{(1)}(t))/\Delta p_k\right]/\Delta t \\
&= \left[R_{ik}^0(t + \Delta t) - R_{ik}^0(t)\right]/\Delta t + \\
&\quad \left[(e_{ik}^{(2)}(t + \Delta t) - e_{ik}^{(1)}(t + \Delta t)) - (e_{ik}^{(2)}(t) - e_{ik}^{(1)}(t))\right]/(\Delta t \Delta p_k) \\
&= \Gamma_{ik}^0(t) + \left[(e_{ik}^{(2)}(t + \Delta t) - e_{ik}^{(1)}(t + \Delta t)) - (e_{ik}^{(2)}(t) - e_{ik}^{(1)}(t))\right]/(\Delta t \Delta p_k) \\
\Delta\Gamma_{ik}(t) &= \left[(e_{ik}^{(2)}(t + \Delta t) - e_{ik}^{(1)}(t + \Delta t)) - (e_{ik}^{(2)}(t) - e_{ik}^{(1)}(t))\right]/(\Delta t \Delta p_k)
\end{aligned}
$$

□

Based on this lemma, the total perturbation can be estimated by the following theorem.

Theorem 4. *The total perturbation for the problem (3.33) is* $\Gamma - S^0 R = (\Delta S)R$ *and is*

bounded by the following quantity

$$(||\Gamma||_F + ||\Delta\Gamma||_F)\frac{||R^{-1}\Delta R||_F}{1 - ||R^{-1}\Delta R||_F} + ||\Delta\Gamma||_F \tag{3.36}$$

when $||R^{-1}\Delta R||_F < 1$.

Proof.

$$\begin{aligned} \Gamma &= SR \\ \Rightarrow \Gamma &= (S^0 + \Delta S)R \\ \Rightarrow \Gamma - S^0 R &= (\Delta S)R \end{aligned}$$

$(\Delta S)R$ is called total perturbation.

We have

$$A^{-1} - (A + E)^{-1} = \sum_{k=1}^{\infty}(-1)^{k+1}(A^{-1}E)^k A^{-1} \tag{3.37}$$

Apply (3.37) to $A = R, E = \Delta R = R^0 - R$, we have

$$R^{-1} - (R + R^0 - R) = \sum_{k=1}^{\infty}(-1)^{k+1}(R^{-1}\Delta R)^k R^{-1}$$

Also,

$$\Gamma^0 = S^0 R^0 \tag{3.38}$$

$$\Rightarrow S^0 = \Gamma^0 (R^0)^{-1} \tag{3.39}$$

$$S = \Gamma R^{-1} \tag{3.40}$$

$$\Rightarrow \Delta S = \Gamma R^{-1} - \Gamma^0 (R^0)^{-1} \tag{3.41}$$

$$= (\Gamma^0 + \Delta\Gamma)R^{-1} - \Gamma^0 (R^0)^{-1} \tag{3.42}$$

$$
\begin{aligned}
&= \Gamma^0(R^{-1} - (R^0)^{-1}) + \Delta\Gamma R^{-1} && (3.43)\\
&= (\Gamma - \Delta\Gamma)(R^{-1} - (R^0)^{-1}) + \Delta\Gamma R^{-1} && (3.44)\\
(\Delta S)R &= ((\Gamma - \Delta\Gamma)(R^{-1} - (R^0)^{-1}) + \Delta\Gamma R^{-1})R && (3.45)\\
&= (\Gamma - \Delta\Gamma)(R^{-1} - (R^0)^{-1})R + \Delta\Gamma && (3.46)
\end{aligned}
$$

Therefore,

$$
\begin{aligned}
(\Delta S)R &= (\Gamma - \Delta\Gamma)(R^{-1} - (R^0)^{-1})R + \Delta\Gamma\\
&= (\Gamma - \Delta\Gamma)(\sum_{k=1}^{\infty}(-1)^{k+1}(R^{-1}\Delta R)^k R^{-1})R + \Delta\Gamma \text{ (if } ||R^{-1}\Delta R||_F < 1)\\
||(\Delta S)R||_F &\leq (||\Gamma||_F + ||\Delta\Gamma||_F)(\sum_{k=1}^{\infty}(||R^{-1}\Delta R||_F)^k) + ||\Delta\Gamma||_F\\
&= (||\Gamma||_F + ||\Delta\Gamma||_F)\frac{||R^{-1}\Delta R||_F}{1 - ||R^{-1}\Delta R||_F} + ||\Delta\Gamma||_F
\end{aligned}
$$

□

Similar to Theorem 4, the total perturbation ε_i for the problem (3.34) can be estimated by

Theorem 5.

$$
\varepsilon_i = ||((\Delta S)R)'_i|| \;\leq\; \frac{||R^{-1}\Delta R||_F}{1 - ||R^{-1}\Delta R||_F}\,\|[(\Gamma - \Delta\Gamma)']_i\| + \|(\Delta\Gamma')_i\| \qquad (3.47)
$$

or

$$
\varepsilon_i = ||((\Delta S)R)'_i|| \approx ||R^{-1}\Delta R||\,\|[(\Gamma - \Delta\Gamma)']_i\| + \|(\Delta\Gamma')_i\| \qquad (3.48)
$$

The bounds and approximation allow the specification of $\mathcal{E}$ and ε_i can be summarized as follows

$$
\mathcal{E} \;\leq\; (||\Gamma||_F + ||\Delta\Gamma||_F)\frac{||R^{-1}\Delta R||_F}{1 - ||R^{-1}\Delta R||_F} + ||\Delta\Gamma||_F, \qquad (3.49)
$$

$$\varepsilon_i \leq \frac{||R^{-1}\Delta R||_F}{1-||R^{-1}\Delta R||_F}\left\|[(\Gamma-\Delta\Gamma)']_i\right\| + \left\|(\Delta\Gamma')_i\right\|, \tag{3.50}$$

$$\varepsilon_i \approx ||R^{-1}\Delta R||\left\|[(\Gamma-\Delta\Gamma)']_i\right\| + \left\|(\Delta\Gamma')_i\right\|, \tag{3.51}$$

where

$$(\Delta R)_{ik}(t) = (e_{ik}^{(1)}(t) - e_{ik}^{(2)}(t))/\Delta p_k,$$
$$(\Delta\Gamma)_{ik}(t) = \frac{[(e_{ik}^{(1)}(t+\Delta t) - e_{ik}^{(2)}(t+\Delta t)) - (e_{ik}^{(1)}(t) - e_{ik}^{(2)}(t))]}{\Delta t \Delta p_k},$$

and $e_{ik}^{(1)}(t), e_{ik}^{(2)}(t)$ are the errors incurred when measuring $x_i^0(t,p_k)$, $x_i^0(t,p_k+\Delta p_k)$, respectively. As stated in the foregoing, noise level is not known *a priori* in most real world systems. In this situation, the network structure is deduced based on the entries in the estimated $S^0(t)$ that are equal to zero for all t and can be estimated by the entries in as $\bar{S}^{(N)} = \frac{1}{N}\sum_{r=1}^{N}\hat{S}(t_r)$ that converge to zero, where $\hat{S}(t_r)$ is the direct influence matrix computed from $\hat{\Gamma}(t_r)$, and $\hat{\Gamma}(t_r), (r = 1..N)$ are measurements or approximations of the total influence matrix $\Gamma^0(t)$ at time t_r .

Proposition 2. *Let $\hat{G}(t_r), (r = 1..N)$ be a measurement or approximation of the total influence matrix $G^0(t)$ at time t_r. Let $\hat{S}(t_r)$ be the direct influence matrix computed from $\hat{G}(t_r)$ using different methods, including ND or ℓ_1-min formulation with different bounds and $\bar{S}^{(N)} = \frac{1}{N}\sum_{r=1}^{N}\hat{S}(t_r)$. Then $\forall(i,j)$ satisfying $S_{ij}^0(t) = 0, \forall t$, $E|\bar{S}_{ij}^{(N)}|^2 \to 0$ as $N \to \infty$.*

Proof. Under perfect reconstruction per ND, $\hat{S} = S^0 + \Delta S$ satisfies

$$\hat{S}R = \Gamma$$

For the r^{th} realization of $\Delta\Gamma_r$, ΔR_r, we have

$$\begin{aligned} \hat{S}(t_r)(R^0 + \Delta R_r) &= \Gamma_r^0 + \Delta\Gamma_r \\ \Rightarrow \hat{S}(t_r) &= (\Gamma_r^0 + \Delta\Gamma_r)(R^0(t_r) + \Delta R_r)^{-1} \end{aligned} \tag{3.52}$$

As $(\Delta\Gamma_{r_1}, \Delta R_{r_1})$ and $(\Delta\Gamma_{r_2}, \Delta R_{r_2})$ are independent if $r_1 \neq r_2$, $\hat{S}_{r_1}$ and $\hat{S}_{r_2}$ are independent. Therefore,

$$Var((\bar{S}^{(N)})_{ij}) = \frac{1}{N^2} Var(\sum_{r=1}^{N} (\hat{S}(t_r))_{ij}) = \frac{1}{N^2} \sum_{r=1}^{N} Var((\hat{S}(t_r))_{ij})$$

Assume that $Var((\hat{S}(t_r))_{ij})$ are bounded by a constant C, for all r,

$$\begin{aligned} Var((\bar{S}^{(N)})_{ij}) &\leq \frac{1}{N^2} NC = \frac{C}{N} \\ \Rightarrow Var((\bar{S}^{(N)})_{ij}) &\to 0 \text{ as } N \to \infty. \end{aligned}$$

□

This averaging procedure allows us to improve the accuracy to predict the pair of nodes that are not connected when the measurement noise level is not available. As a result, our method ensures low false positive rates on the "arcs". As noted in the context of Proposition 1, network inference with $\bar{S}^{(N)}$ tends to be at least as good as with $\hat{S}(t_r)$ even when $Var(\hat{S}(t_r))$ is arbitrarily large.

3.4 Numerical case studies

We have considered two case studies to validate the theoretical results and evaluate the performance of the ℓ_1-min approach. The first case study contains two simulation scenarios. The first scenario simulates a scale-free network whose structure resembles that of the genetic regulation process of E. Coli species [55]. Here, the challenge is to

estimate the true network structure, i.e., the direct influence matrix S^0 from a noisy total influence matrix G. This scenario is optimal for assessing the closeness of the bounds stated in Eqs. (3.18 - 3.20) relative to the true bounds on the constraints $\mathcal{E}^{(0)} = ||(G + I)^T S^0 - G||_F$, and comparing the performance of the ℓ_1-min formulation relative to the recent ND methods in terms of inference error and sparsity. The next scenario simulates a system of Hill-type differential equations modeling a gene interaction network. Here, the challenge is to estimate the true network structure from noisy and transient time series data. The second case study is an application of our method to infer genetic regulatory networks (GRNs) from empirical data in the context of DREAM5 challenge [56]. This challenge is a standard framework for evaluating GRN inference methods.

3.4.1 Case I: simulation studies

Inferring direct influence networks from total influence network

First, we adapted the procedure specified by Muchnik [57] to generate 500 random realizations of scale-free networks consisting of $n = 100$ nodes, with a degree exponent of 2.2. In each realization, the weights of the true direct influence network, s^0_{ij} follow the distribution $\mathcal{N}(\mu_{S^0}, \sigma^2_{S^0})$ with $\mu_{S^0} \sim \mathcal{N}(0, 0.04)$, and $\sigma_{S^0} \sim \mathcal{N}(0, 0.04)$. The true total influence matrix G^0 was obtained as $G^0 = S^0(I - S^0)^{-1}$. The noisy total influence matrix was generated as $G = G^0 + \Delta G$, where the contaminated noise ΔG was considered in two cases: (1) proportional, i.e., $(\Delta G)_{ij} = \alpha\mathcal{N}(\mu_{S^0}, \sigma^2_{S^0})$ and (2) independent, i.e., $(\Delta G)_{ij} = \mathcal{N}(0, \sigma^2_{S^0})$. We considered cases where the measurement noise level $||\Delta G||_F$ is known as well as those where there is uncertainty in estimating the measurement noise level.

We first compare the "true" bound $\mathcal{E}^{(0)}$ (computed using S^0) and the bounds for $\mathcal{E}$ estimated based on Eqs. (3.19-3.20). In the presence of noise, the bounds appear to be in the same order of magnitude for all simulated networks (Table 3.2). The results also

Formula	Mean
$\mathcal{E}^{(0)} = \|\|(G+I)^T S^0 - G\|\|_F$	9.79×10^{-3}
$\mathcal{E}^{(1)}$ (Eq. 3.19)	8.89×10^{-3}
$\mathcal{E}^{(2)}$ (Eq. 3.20)	8.61×10^{-2}

Table 3.2: Comparison of bounds on total perturbation obtained using Eq. (3.19) and Eq. (3.20) suggests that Eq. (3.19) provides a good approximation and Eq. (3.20) serves as an upper bound of $\mathcal{E}^{(0)}$.

suggest that the bound specified in Eq. (3.19) closely matches the "true" bound and can be used to approximate the feasible region when $\mathcal{E}^{(0)}$ is unknown with high accuracy. Although the bound in Eq. (3.20) tends to be loose, it can be used as an upper bound for $\mathcal{E}^{(0)}$.

We next compared the performance of ND and ℓ_1-min approaches (using our bounds Eq. (3.19) and Eq. (3.20)) in terms of inference error defined as $\rho = \frac{||\hat{S}-S^0||_F}{||S^0||_F}$, where $\hat{S}$ is computed using the different methods being compared. The ℓ_1-min approach with "true" constraint bound $\varepsilon_i = \varepsilon_i^{(0)}$ significantly improves the ND (the mean and the variance of the estimated ρ were reduced by 45% and 99%, respectively) (Fig. 4.2). Employing $\varepsilon_i = \varepsilon_i^{(1)} = \mathcal{E}^{(1)}/\sqrt{n}$ (based on Eq. (3.19)), the ℓ_1-min approach performs much better than ND (the mean and variance of ρ are reduced by 33.5% and 87.5%, respectively). More importantly, the inference error of ℓ_1-min approaches were concentrated around of 0.15 within ± 0.05, while those of ND were spread over a larger range, from 0.3 to 0.6. This suggests that ℓ_1-min approach using our bound in Eq. (3.19) is more robust than ND to noise and approximation error incurred when measuring the total influence matrix.

We also compared the sparsity of the recovered networks measured in terms of Hoyer sparsity measure [58] defined as follows

$$Hoyer(S) = \frac{n - (\sum_{i,j=1}^{n} |s_{ij}|)/\sqrt{\sum_{i,j=1}^{n} s_{ij}^2}}{n-1}.$$

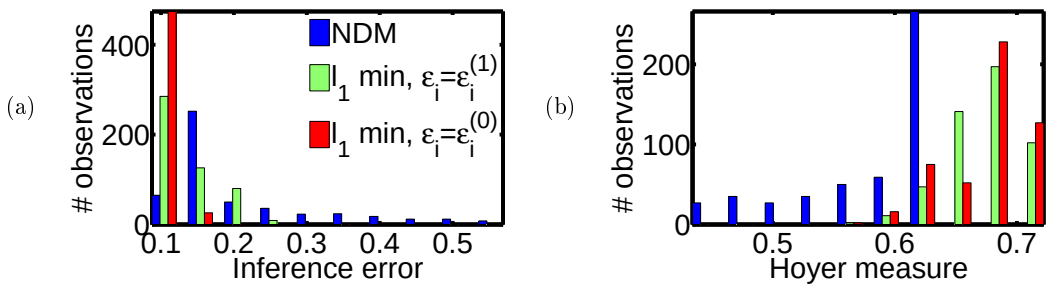

Figure 3.2: Histograms summarizing the relative performance of ND and ℓ_1-min approaches for the benchmark numerical case in terms of (a) inference error that quantifies the accuracy and (b) Hoyer measure that quantifies the sparsity of the solution. The solution from the ℓ_1-min approach is more precise and sparser than ND: compared to NDs, the mean and the variance of the inference error are reduced by 45% and 99%, respectively, when using ℓ_1-min with $\varepsilon_i = \varepsilon_i^{(0)}$; 33.5% and 87.5%, respectively when using ℓ_1-min with $\varepsilon_i = \varepsilon_i^{(1)}$; the mean of Hoyer measure is increased by 16.38% and variance reduced by 69% when using the ℓ_1-min with $\varepsilon_i = \varepsilon_i^{(0)}$, and is increased by 15.90% in mean, reduced by 75.69% in variance when using $\varepsilon_i = \varepsilon_i^{(1)}$.

Note that $Hoyer(S) \in [0, 1]$. The closer it is to 1, the sparser S is. In terms of this measure, the solution of the ℓ_1-min approach is much sparser (mean is 16.38% larger, variance is 69% smaller when using the true bound $\varepsilon_i = \varepsilon_i^{(0)}$, and mean is 15.90% larger, variance is 75.69% smaller when using the approximated bound $\varepsilon_i = \varepsilon_i^{(1)}$) than solution of ND (Fig. 4.2b). Also, the Hoyer measure of the ℓ_1-min approach is concentrated more around a much higher value (sparse matrices) than that of ND indicating that the ℓ_1-min approach using our bound gives a significantly sparser solution than ND. As a result, this gives a more interpretable connection structure without the loss of performance.

We also studied the effects of the bounds of ℓ_1-min formulation on inference error to verify Eq. (3.24) numerically. When $\varepsilon_i/\varepsilon_i^{(0)} > 1$, the inference error trends almost linearly with ε_i (see Fig. 3.3). This confirms the conclusion of Theorem 3. Also, when $\varepsilon_i/\varepsilon_i^{(0)} < 1$ and tends toward 0, the inference error increases. This shows an evidence of over-fitting. Subsequently, we studied the effect of averaging (Proposition 1) in the context of the ℓ_1-

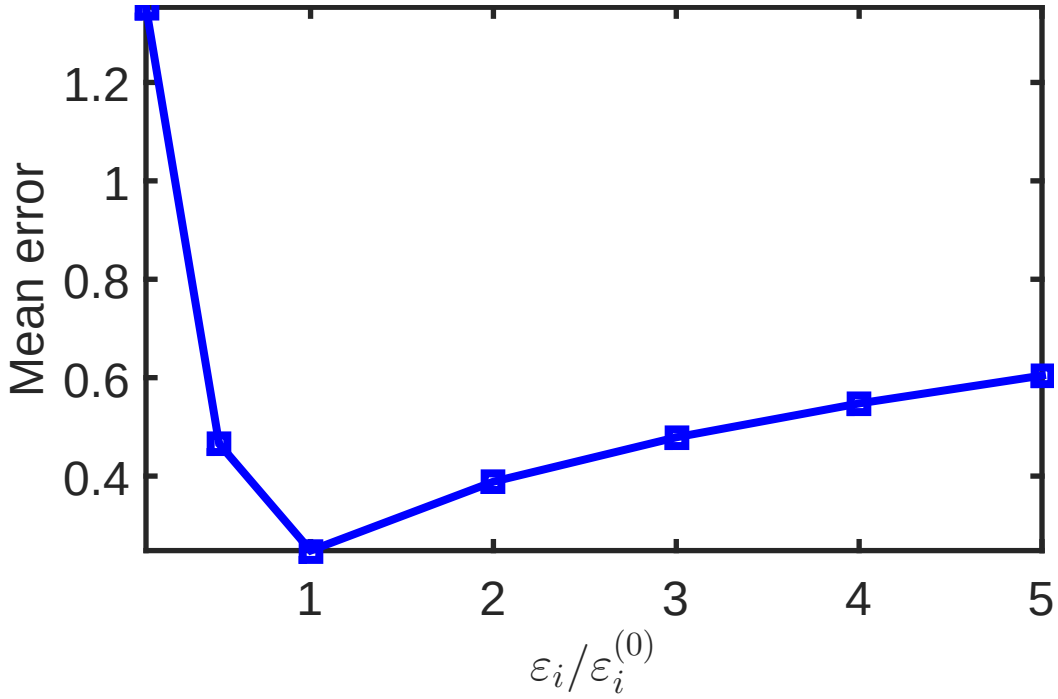

Figure 3.3: Variation of inference error with total perturbation bound ε_i. The inference error attains a minimum near the true bound $\varepsilon_i^{(0)}$, and it trends almost linearly with ε_i as it is increased beyond $\varepsilon_i^{(0)}$. As $\varepsilon_i \to 0$, the inference error increases exponentially, which is an evidence of over fitting.

min and ND methods. We conducted N =40 simulations, in each of which, S^0, G^0 and ΔG were generated as stated in the foregoing . We used the inference error without $\rho^{(N)}$ and with averaging $\bar{\rho}$ as measures for comparison from each simulation defined as follows:

$$\rho^{(N)} = \frac{1}{N}\sum_{k=1}^{N} ||(\hat{S}^{(k)} - S^0)||_F / ||S^0||_F, \tag{3.53}$$

$$\bar{\rho} = ||\bar{S}^{(N)} - S^0||_F / ||S^0||_F, \tag{3.54}$$

where $S^{(k)}(k = 1, ..., N)$ is the k^{th} realization of $S^{(k)}$ and $\bar{S}^{(N)}$ is estimated as stated in Proposition 1. The results suggest that averaging reduces the inference error of both methods by about 8 times in all cases, thus supporting the validity of Proposition 1 (Fig. 3.4). The inference errors were almost the same between ND and ℓ_1-min with $\varepsilon_i = \varepsilon^{(1)}$.

3.4.2 Inferring direct influence network structure from multiple time series under transient conditions

In this section we represent the performance of ℓ_1-min approach in inferring network structure from transient time series with an unknown noise level. In this study we used Michaelis-Menten dynamic system given by [45]:

$$\dot{x}_i = p_i x_i + \sum_{j=1, j\neq i}^{n} s_{ij}^0 \frac{x_j}{1 + x_j}, \tag{3.55}$$

where the "true" network defined by (s_{ij}^0) is a scale-free network [55] generated randomly with degree exponent $\gamma = 2.2$ consisting of $n = 40$ nodes with about 70 edges, whose weights s_{ij}^0 follow the distribution $\mathcal{N}(5, 0.25)$.

We obtained 30 different variants of this network. For each of these invariants (trials), a perturbed network was obtained by changing (perturbing) the parameters according to Eqs. (3.30 - 3.32). Every solution $\boldsymbol{x}(t)$, $t \in [0, 1]$, obtained from an initial condition

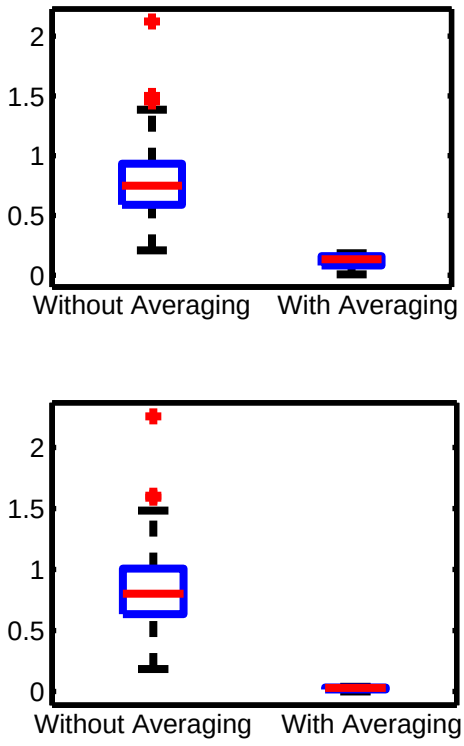

Figure 3.4: Box plots summarizing the effects of averaging on (a) ND and (b) ℓ_1-min with $\varepsilon_i = \varepsilon^{(1)}$. The inference errors were almost unchanged with ℓ_1-min compared to ND. Averaging (light/red) reduced inference error further by about 8 times compared to without averaging (dark/blue). The $\bar{\rho}$ values were 0.1196 with ND and 0.0259 with ℓ_1-min (p-values of the paired t-tests between the inference error without and with averaging were $\leq 10^{-5}$ in all cases).

$\boldsymbol{x}(0)$ was contaminated with noise of the form $\mathcal{N}(0, \sigma^2)$ to simulate a noisy measurement $\hat{\boldsymbol{x}}(t)$. Here σ^2 was chosen to be 10^{-4}. The direct influence matrix $\hat{S}(t_k)$ were estimated using Sontag *et al.*'s [2] method, as well as ℓ_1-min formulations, with different values of bounds. Next, $\bar{S}^{(N)}$ was estimated as in Proposition 2 by averaging over 30 time samples $t_k \in [0, 1], k = 1..30$ chosen randomly. For performance evaluation, we used the inference error without $\rho^{(N)}$ and with averaging $\bar{\rho}$, given by

$$\rho^{(N)} = \sqrt{\frac{1}{N}\sum_{k=1}^{N}\sum_{i,j}(1 - \mathcal{H}(|s_{ij}^0|))(\hat{s}_{ij}(t_k))^2}, \tag{3.56}$$

$$\bar{\rho} = \sqrt{\sum_{i,j}(1 - \mathcal{H}(|s_{ij}^0|))(\bar{s}_{ij}^{(N)})^2}, \tag{3.57}$$

where $\mathcal{H}(.)$ is Heaviside function. These error measures quantify the number of absent links ($s_{ij}^0 = 0$) that are correctly identified.

As summarized in Fig. 3.5, the ℓ_1-min approach performs better than Sontag *et al.*'s [2] method in all cases tested. In fact, $\rho, \bar{\rho}$ were reduced by 10^5 times. The poor performance of Sontag *et al.*'s [2] method is attributed to the numerical issues noted in the earlier section. A further 30% reduction in inference error resulted from averaging for both cases. Next, the cases (c) and (d) were designed to simulate the real situations where the noise magnitude is unknown. We considered cases where the noise levels are under or overestimated by 1 order of magnitude. While Sontag *et al.*'s [2] method would not be applicable in such cases, ℓ_1-min without averaging was found to lead to suboptimal inference. Under underestimation $\varepsilon_i < \varepsilon_i^{(0)}/10$, averaging was found to further reduce the inference error by about 70%, and the inference error $\bar{\rho}$s were of the same level as one would obtain when the noise level is known. This result is consistent with and is a clear verification of Proposition 2. When the noise level is overestimated, the resulting network tends to be highly sparse, offering excellent specificity in identifying the absence of direct coupling. The inference

errors are therefore low even without averaging by default. In this case averaging reduces the inference errors by 5%. The p-values of the paired t-tests between the inference error with and without averaging were below 0.0282 in all cases suggesting that averaging helps improve network inference.

Case II: Application to empirical genetic regulatory network inference

Next, we applied our method to infer real world GRNs and compare its performance with other methods including ND [44], Bayesian network inference, Pearson and Spearman correlation networks [8] using the framework presented in DREAM5 challenge. Here, the Pearson and Spearman correlations were considered as they are the most widely used methods for network inference and can provide a reasonable estimation of the total influence matrix [44, 45]. In addition, ND has been most effective in inferring network topology when the total influence matrix G is estimated using Person and Spearman correlations. Therefore, these serve as the challenging test cases to evaluate the performance of ℓ_1-min where ND is already effective. The DREAM5 challenge contains gene-expression microarray data of three species including an *in silico* benchmark, a prokaryotic model organism (E. coli) and a eukaryotic model organism (S. cerevisiae). Beside ρ and Hoyer metrics, we employed the following score, which was used in earlier works [8] to assess the performance of a network inference method for recovering the structure underlying these data sets:

$$\xi = -\frac{\log(p_{ROC}) + \log(p_{PR})}{2}, \tag{3.58}$$

where p_{ROC} and p_{PR} are p-values computed from AUROC (area under receiver operating characteristic curve) and AUPR (area under precision-recall curve).

The results of the performance evaluation are summarized in Fig. 4.1. We note that for computing the performance metrics we first generated 30 different G matrices with Pearson correlation, 30 others with Spearman correlation and another 30 with Mutual In-

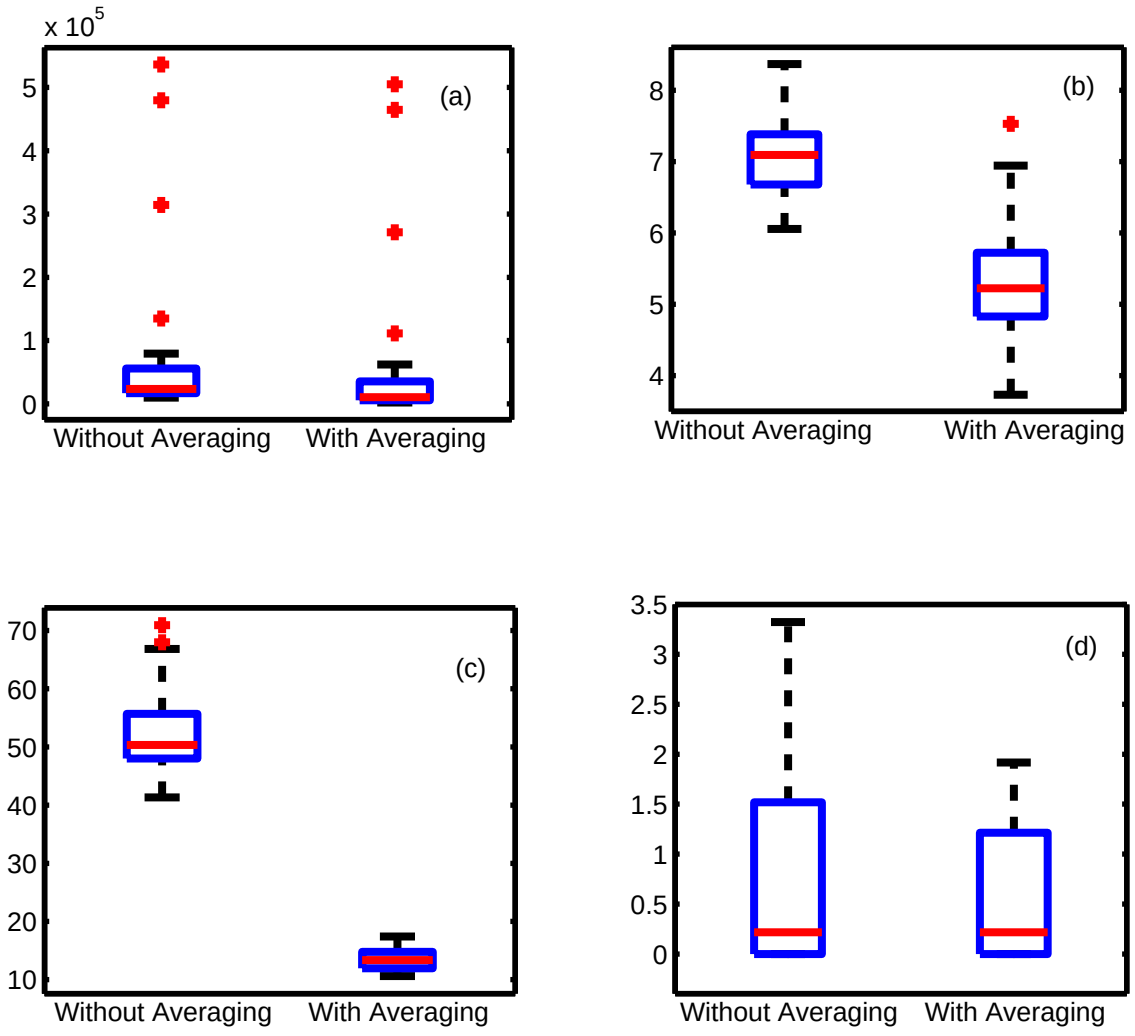

Figure 3.5: Box plots summarizing the inference errors without (light/red) and with (dark/blue) averaging for: (a) Sontag *et al.*'s [2] method ($\rho = 7.58 \times 10^4, \bar{\rho} = 5.87 \times 10^4$); (b) ℓ_1-min with noise magnitude given ($\rho = 7.11, \bar{\rho} = 5.32$), (c) ℓ_1-min with noise magnitude underestimated as 10% the actual ($\rho = 52.50, \bar{\rho} = 13.40$), and (d) ℓ_1-min with noise magnitude overestimated as 10 times the actual ($\rho = 0.80, \bar{\rho} = 0.60$). The inference error was reduced by 10^5 times with ℓ_1-min approach (3.33, 3.34), compared to Sontag *et al.*'s [2] method. Averaging further reduced inference error by at least 30% in all cases (p-values of the paired t-tests were consistently below 0.0282).

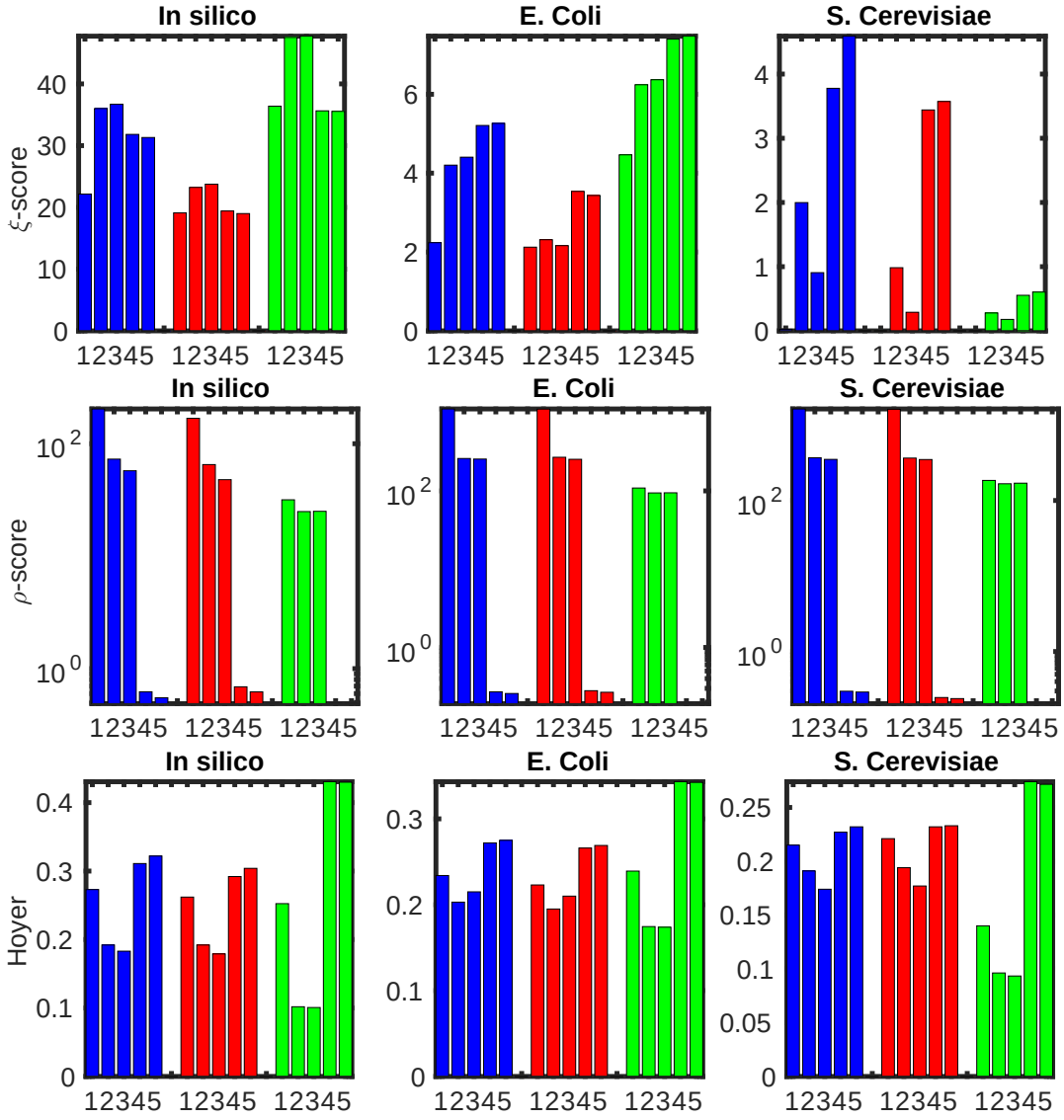

Figure 3.6: Performance comparison of (1) original G matrix, (2) ND, (3) ND with averaging, (4) ℓ_1-min and (5) ℓ_1-min with averaging for the DREAM5 challenge datasets. The total influence G matrix is estimated by Pearson correlation (blue/dark) and Spearman correlation (red/ dark light) and Mutual Information (green/light). Compared to ND, the prediction scores with ℓ_1-min are increased by 23.94% (for G from Pearson correlation), 53.03% (for G from Spearman correlation) & 18.53% (for G from Mutual Information) for E. coli, 89.09%, 249.7% & 116.74% for Cerevisiae, respectively; the inference errors ρ (Eq. (3.56)) are reduced by 2 to 3 orders of magnitude in all cases; Hoyer measures are increased by 34%, 36.41% & 322.91% for E. Coli, 18.85%, 19.59% & 96.65% for Cerevisiae, respectively. For *in silico* data, ND gives a solution with 11% higher prediction score but 33% less sparse than ℓ_1-min approach. Averaging slightly improves the performance of all methods ($< 10\%$).

formation for each data set. The G matrix in each case was estimated using samples of size 75% of the data set. The averaging procedure considers the S matrices estimated from these G matrices using different methods. In terms of ξ-score (Eq. (3.58)), which quantifies how well—in terms of having low false negative rates (FNR, related to sensitivity), and low false positive rates (FRN, related to specificity), the true positive rate (TPR) and true negative rate (TNR)—the estimated $\hat{S}$ captures S^0, ℓ_1-min approach yields $\hat{S}$ with at least 18.53% higher than with ND in all cases tested except the *in silico* case (see Fig. 4.1). Both ND and ℓ_1-min performed better than Bayesian network approach whose ξ-scores were 14.891, 0.029, 0.0001, respectively, for the three data sets [8]. In terms of ρ-score (Eq. (3.56)), which quantifies the false positive rates i. e., the specificity, ℓ_1-min approach reduces ρ by 2-3 orders compared to ND in all cases. These results provide a strong evidence for the relevance of the ℓ_1-min approach for network structure inference. In terms of sparsity, ℓ_1-min approach increased the Hoyer measure by about 20% in most cases, and were much closer to the Hoyer measures of the gold-standard network, compared to ND.

As noted earlier for *in silico* data, although the ρ-score with ℓ_1-min was at least 1160% lower (i.e., higher specificity) and Hoyer was 33% higher (i.e., higher sparsity), the ξ-score was slightly (~10%) lower than with ND. The lower ξ-score for ℓ_1-min is perhaps a consequence of the method being susceptible to over-specification of the noise level. In this context, it must be noted that the solutions from both ND and ℓ_1-min can replicate the observed total influence G within a specified bound (as total perturbation). However, the solutions from ℓ_1-min tend to be much sparser and have lower false positive rate. Given that there were only 805 sample measurements to reconstruct G matrices for 1643 nodes in the *in silico* network, it is highly likely that several dynamic modes (degree of freedom) are not observable from the data. Therefore, ℓ_1-min generated a much sparser network which, by formulation is guaranteed to be adequate to capture the observed modes of the dynamics within the specified total perturbation limits. The ND derived networks for *in silico* and

other cases that have higher ξ-score, intriguingly, were consistently found to have much lower Hoyer score (hence sparsity) even compared to the specified total influence matrix. Thus, ℓ_1-min-generated solutions provide significant improvement in specificity, although the sensitivity at times were found to be slightly lower than with ND.

Averaging improves the ξ-scores (Eq. (3.58)) with all methods by at most 10%. This is perhaps due to the near-stationarity of the total influence matrix G, when computed using data over long time windows that smooths out various higher order transient effects. Also, one may note that the averaging makes the network inferred from ND less sparse than without averaging. This is because under noise, transients and data sparsity, ND yields vastly different network topologies depending on the samples employed. Averaging over these vastly different networks causes a reduction in sparsity. These results, taken together suggest that the ℓ_1-min approach is perhaps the best known means to provide specificity for network inference from transient and noisy data. The utility of the approach would be to provide a minimal set of arcs (dynamic couplings or direct influences) to be considered for further network dynamics reconstruction applications.

3.5 Discussion and Concluding remarks

In this chapter, we have investigated a method to robustly infer the structure of a network representing a sparse dynamical system from noisy, transient time series data. When the noise level is known, the ℓ_1-min formulation employing our theoretical formula for the bound on total perturbation improves the recently reported NDs in terms of both accuracy and sparsity. When the noise level is unknown, we have shown that by averaging the networks inferred from different time points or conditions, the inference of network structure of real world processes becomes highly plausible.

Pertinently, for most real world processes, the total influence is not known a priori; only the time series ensembles gathered under transient conditions are available (e.g., gene

expression microarray data [8, 59], protein-protein interaction data [60] as in the case of Michaelis-Menten dynamics). It has been noted that most of the earlier approaches present severe accuracy, noise sensitivity and/or numerically stability issues for such realistic scenarios. To overcome these limitations, we have investigated the ℓ_1-min approach with a novel perturbation procedure for time series based network inference. Averaging over the solutions estimated at different time windows has been shown to allow inference of the structure for complex real world networks, especially when the noise levels are unknown or cannot be accurately estimated.

Next, we have applied our method to three benchmark systems: a sparse scale-free network [61] with a specified noise level and the total influence between any two nodes given, a genetic regulatory network model formulated in terms of a system of Hill-type differential equations [45], and GRNs of DREAM5 challenge [56]. These analyses suggest that our proposed bounds on the constraints for the ℓ_1-min formulation, extracted from a few time series samples acquired under transient conditions, are of the same order (i.e., they closely envelop) with the constraints estimated based on the full knowledge of the noise level. The ℓ_1-min formulation reduces the inference errors defined in (3.58) and (3.56) by 18.53% and 2 to 3 orders of magnitude, respectively, and improves the sparsity of the solution (measured in terms of Hoyer sparsity measure) by 15.9%, in comparison with conventional approaches including various versions of dynamic Bayesian approaches for network inference as well as ND. If instead of the total influence, only the time series gathered under transient conditions is provided, such as in the case of Michaelis-Menten dynamics, ℓ_1-min approach achieves a 4 order reduction in inference error compared to MRA. These theoretical and and numerical studies suggest that our proposed method can be employed to effectively infer the presence of dynamic coupling (i.e., arc set or the direct influence in a dynamic network) based on sparse samples.

As with any network reconstruction approach, the method assumes that the time se-

ries realizations taken together can adequately mirror the salient dynamic regimes of the underlying process, and as noted earlier, the approach is restricted to ensuring high levels of specificity and not sensitivity in identifying the direct influences. Additionally, while the approach is fairly robust to the presence of noise, the estimates $\hat{s}_{ij}$ from the averaging procedure for the arcs with $s_{ij}^0 = 0$ is guaranteed to converge to zero only in the presence of additive noise. More specifically, one of the following conditions need to hold for the approach to be applicable: (1) the governing equation of the process dynamics is specified, so that $G(t)$ or $R(t)$ can be constructed; (2) one or more realizations of $G(t)$ (based on ND or silencing method) or $R(t)$ (based on MRA) are given. In our experience, 30 realizations ensured the convergence of the averaging method; (3) one realization of a $n-$dimensional time series is available for estimating $G(t)$ using various alternative methods outlined in [44] or n^2 time series realizations with the same initial condition are available for estimating $R(t)$ using Eq. (3.29). Note that Scenario 1 is useful only for applications such as to investigate if there exists a more compact (sparser) network representation to capture the specified process dynamics. In Scenarios 2 and 3, we assume that the noise level or its lower limit is known, and adequate number of realizations are available to ensure convergence of the averaging method. In scenario 3, Eq. (3.29) yields a finite space-time approximation of the partial derivatives $\frac{\partial x_i}{\partial p_j}, \frac{\partial \dot{x}_i}{\partial p_j}$. They are estimated by perturbing the parameters p_j and keeping the initial condition the same for two time series signals. The length of the time series in this case can be really small, or it can just be samples taken over multiple (roughly 30), short (can be even 2 samples) time windows. However, the time steps (or sampling interval) in each time window must be small enough to ensure that $R(t)$ values locally converge. Sensitivity of the network inference performance to time step size, however, needs further investigation.

Efforts are underway to address some of the ℓ_1-min aforementioned limitations. We are investigating a two-stage approach to recover local nonlinear dynamics from sparse

time series data. For future research, we will consider a more realistic scenario where not all state variables can be measured. In GRN inference, for example, only the outputs/activations of only those genes that have been discovered are measured. However, unknown genes might have significant influence on the network structure. Removing the effects of unmeasured variables, when combined with the method proposed in this chapter, will lead to a more advanced network inference method.

4. DETECTING CHANGES IN TRANSIENT COMPLEX SYSTEMS VIA DYNAMIC NETWORK INFERENCE

In this chapter, we present an approach based on spectral graph theory to detect changes in complex dynamic systems using a single realization of time series data collected under specific, common types of transient conditions, such as intermittency. We introduce a statistic, γ_k, based on the spectral content of the inferred graph. We show that γ_k statistic under high dimensional dynamics converges to a normal distribution, and employ the parameters of this distribution to construct a procedure to detect qualitative changes in the coupling structure of a dynamical system. The method is applied to problem of seizure detection using EEG signals.

4.1 Introduction

With recent growth in the Internet of Things (IoT) [62–64], wearable health systems/sensors technologies [65, 66], and social networks [67–69], detection of anomalies in complex large dimensional systems is beginning to evoke keen interest [70]. Detecting changes is essential to discerning the transition of a system into an anomalous state, such as from an in-control to an undesirable out-of-control state in a manufacturing process, or from a healthy to a pathological state in a human physiological process. Failure to detect changes might lead to catastrophes. For example, in a human physiological process, failure to detect neurological disorders early, as in epileptic seizures, leads to about 189,000 lives lost each year [71]. In the automotive manufacturing industry, failure to detect faulty components can be costly. For example, in 2014, General Motors incurred over $2.4 billion in costs of car recalls resulting from a faulty switch. This was 85% of the company's total income that year [72]. While human healthcare, manufacturing, and other industrial environments have become data-rich, the following issues limit the applicability of current

approaches to detecting changes in these complex systems:

- **High dimensionality**: A real-world system such as a human brain contains billions of neurons, each executing its internal processes [9]. Therefore, specification of the state of human brain physiology and of other real-world complex systems requires a large set (from several hundreds to millions) of variables to capture the system dynamics, incurring enormous computational and inference issues.

- **Interconnectivity:** Most real-world systems are known to manifest as complicated, albeit sparse, interconnected structures [73, 74]. For example, the human brain has about 10^{11} neurons, and each neuron has on an average 7,000 synaptic connections to other neurons, which totals about 10^{15} connections [9]. As the structure of the interconnection in a system defines its dynamics [6], the system dynamics cannot be understood by superposing the decoupled dynamics of the individuals or subsets of state variables [7].

- **Transience:** The structure of active interconnections and the strength of those couplings vary over time, i.e., the coupling structure among the system state variables is not constant. As an illustration, the functional structure of a human brain network depends on the momentary mental condition. According to Picchioni *et al.* [10], brain connectivity is strong during resting wakefulness, decreases during stage N2 of NREM sleep, further decreases during stage N3 of NREM sleep and possibly increases during REM sleep. Thus, the dynamics are often transient.

- **Nonlinearity:** The evolution of a state variable depends nonlinearly on the values of other state variables, i.e., the resulting behavior can not be expressed as a mere linear combination (or superposition) of the state variables [11]. For example, in a brain network, the response of a given neuron to presynaptic input from another

neuron depends on multiplicative interactions among the synaptic inputs from several other neurons. This type of multiplicative mechanism raises issues of how to define couplings locally in the state space and compactly capture the underlying relationships [12, 13].

Also, for real-world systems, the equations representing system dynamics are unknown. What is available is a noisy multivariate time series output from state variables. Conventionally, there are many methods for detecting changes in high-dimensional systems from time series, including multivariate CUSUM charts [75, 76], multivariate EWMA charts [77, 78], (multiscale) PCA [79–81], and multivariate control charts [82, 83]. However, these approaches suffer from the same drawback, i.e., the effects of changes in the coupling structure of a system are not guaranteed to be directly identified with a high degree of sensitivity and specificity. Therefore, one reasonable approach to addressing this drawback and these challenges is to develop a change detection statistic based on the structure of the interactions of these systems. This approach is in its early stage [84–86]; most of the studies reported in the literature have certain limitations, including that the distribution of the statistic is unknown, high sensitivity to extraneous noise, and an inability to capture qualitative structural instabilities.

In this chapter, we first introduce an approach to infering the temporal network structure from a single transient multivariate time series. The network inference approach we developed here is suitable for studying many systems, such as brain networks (using data collected from EEG electrodes or fMRI) and cyber-manufacturing systems (using data collected from sensors embedded in the machines). Second, we present a novel spectral-graph-based statistic to detect major changes in multidimensional time series. These contributions together create a novel framework for change detection in multidimensional transient processes. The rest of this chapter is organized as follows. In Section 4.2, we

provide background and related literature on network inference and change detection. Section 4.3 contains our approach to inferring the network structure from a single time series realization and extracting the change detection statistic γ_k. Numerical and real world case studies to validate the method are presented in Section 4.4. The chapter concludes in Section 4.5.

4.2 Graph representation and change detection in complex systems

Directed graphs offer a convenient means to represent the dynamics of high-dimensional, interconnected systems (see Fig. 4.1). Here, the nodes x_i represent the state variables (and capture the intrinsic dynamics) and arcs s_{ij} represent the (instantaneous) strengths of the coupling, i.e., the influence of a state variable on the evolution of other state variables. In many cases, the network needs to be inferred from the measured time series outputs of state variables. The most common approach for inferring a network from a multivariate time series is to use similarity quantifiers, such as correlation or mutual information [86–91]. However, networks inferred using the estimates of such conventional statistical dependency measures often contain spurious links due to the transitivity of influences among the nodes [44].

Several alternative approaches have been reported to address this issue [38–44, 52, 92, 92–97]. However, the current methods have certain limitations. For example, the global silencing method [52] works only when the system operates close to a steady state and assumes that such a state exists, and ignores the noise effects. The network deconvolution method [44] requires the network to be linear time invariant. Bayesian methods [38–43] require the directed graph to have no cycles. There are approaches to infer a directed acyclic graph from data; however, they are often very computationally expensive. Methods that are based on estimating partial correlation [92] or Granger causality [93–97] require stationarity and linearity of the underlying dynamics and do not aim to recover the cou-

plings that capture the physical causal chains. The molecular response analysis (MRA) method [2] can address some of these drawbacks. However, it requires n^2 realizations of the time series. This requirement makes MRA impractical as collecting different time series realizations is very expensive or impossible. MRA also suffers from numerical instability issues and its performance degrades sharply in the presence of noise. Recently we reported an approach [98] to solving these technical limitations by reducing the number of perturbations required to be an order of n and introducing a perturbation procedure to solve the numerical instability issue. This method was able to reduce inference error, often by 5 orders of magnitude over the MRA method in numerical case studies. However, our method needs to be further improved to be suitable for real world change detection applications, where only a single time series realization is available for inferring the network and hence the coupling structure. Therefore, a new method to infer the network from a single multivariate time series realization is necessary.

According to recent studies [6, 86, 99–103], qualitative changes that are known to cause anomalous behaviors, such as crises [104, 105] and pathologies [84, 85, 106], are due to major changes in the interconnectivity and not changes in the intrinsic dynamics of the individual state variables [101–103]. Therefore, it is necessary to develop a statistic to detect changes in the structure of the interactions of these systems. Graph representation provides a convenient approach to detecting these structural changes in the dynamics of complex real world systems. It provides not just the points in time where changes occur but also insights into the causes and structural pathways of the changes.

Currently, detecting anomalies and changes in complex systems employing graph representation is in the early stages [84–86]. Most related studies in the literature are based on applying a control chart to the quantifiers of graph topology, such as centrality, clustering coefficient, connectivity, density, scan statistics, degree distribution, and diameter [107–111]. Algebraic approaches based on extracting the spectral quantifiers from

an adjacency matrix of the graph by employing decomposition techniques such as singular value decomposition, compact matrix decomposition, and CUR matrix approximation have also been investigated [88]. Recently, the inner product between major eigen directions of the adjacency matrix of the graph representations at different time points has been used as a feature for detecting changes [69, 112].

However, these features have significant limitations: (a) the statistical distributions of many of these features remain unknown, and hence change detection approaches based on these features use arbitrary thresholds and limits that are not based on achieving specified sensitivity (beta error) and specificity (alpha error) levels, (b) other features with specified distributions tend to be highly sensitive to extraneous noise and hence do not serve as an effective feature for change detection (as illustrated in the case study in Sec. 4.4.1), and (c) more pertinently, they are not developed to capture qualitative structural instabilities (i.e., a major change such as a drop in dimensionality of the coupling structure) in the dynamics underlying the specified graph representation. These methods literally breakdown in detecting major events such as seizures which are characterized by a drop in the dimensionality of the system. The present inference method as well as the γ_k statistic which is based on capturing the active degrees of freedom based on the graph spectra aim to address this current gap.

4.3 Methodology

In this section, we first address the challenge of reconstructing the network from a single time series realization assuming completely deterministic dynamics (noise free) in Sec 4.3.1 and discuss key numerical procedure in Sec 4.3.2. Next, we extend this approach to noisy time series in Section 4.3.3. In Sec. 4.3.4, we introduce a statistic that captures the spectral characteristics of the inferred network for change detection.

4.3.1 Inferring the coupling structure based on perturbing initial conditions

In this section, we consider a noise-free case. In general, a real-world complex system can be modeled by the following dynamical system

$$\dot{x}_i(t) = f_i(\mathbf{x}, \boldsymbol{p}_i, t), i = 1..n \tag{4.1}$$

$$x_i(0) = a_i, \tag{4.2}$$

where $\boldsymbol{p}_i$ are system parameters, $\mathbf{x}$ is a state vector, $\mathbf{a}$ is the initial condition. This dynamical system has the coupling structure, i.e., the direct influence network representation, as in Fig. 4.1. Here a node i represents a state variable x_i ($i = 1, ..., n$). The weight on an edge (i, j) connecting nodes i and j is given by

$$s_{ij}(t) = \frac{\partial f_j(\mathbf{x}(t), \mathbf{p}_j, t)}{\partial x_i}.$$

Intuitively, $s_{ij}(t)$ quantifies how much node j changes in response to an infinitesimal

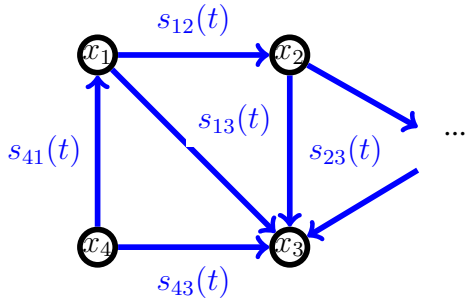

Figure 4.1: Direct influence network representation

change in node i when keeping all other nodes unchanged, i.e., at the current state. Therefore, it represents the direct influence from node i on node j. Note that $s_{ij}(t) = 0$ when

there is no direct influence from node i on node j, i.e., there is no dynamic coupling between the current state of nodes i and j. Thus, $S(t) = (s_{ij}(t))_{n\times n}$ captures the local physical coupling structure of the system (4.1,4.2). In the following paragraphs, we explain how to estimate $(s_{ij}(t))_{n\times n}$ from time series $\mathbf{x}(t)$. First, by taking partial derivative on both sides of Eq. (4.1) w.r.t some parameter α_k,we have:

$$\begin{aligned}\frac{\partial \dot{x}_i(t)}{\partial \alpha_k} &= \frac{\partial f_i(\mathbf{x}, \boldsymbol{p}_i)}{\partial \alpha_k} \\ &= \sum_{l=1}^{n} \frac{\partial f_i(\mathbf{x}, \boldsymbol{p}_i)}{\partial x_l} \frac{\partial x_l}{\partial \alpha_k} + \sum_{l=1, p_l \in \boldsymbol{p}_i}^{|\boldsymbol{p}_i|} \frac{\partial f_i}{\partial p_l}(\mathbf{x}, \boldsymbol{p}_i) \frac{\partial p_l}{\partial \alpha_k}, \end{aligned} \tag{4.3}$$

where $|\boldsymbol{p}_i|$ is dimension of $\boldsymbol{p}_i$. Intuitively, $\frac{\partial \dot{x}_i(t)}{\partial \alpha_k}$ quantifies how $\dot{x}_i(t)$, the instantaneous rate of change of node i with respect to time, responds to an infinitesimal change in the system parameter α_k. It follows from (4.3) that

$$\frac{\partial \dot{x}_i(t)}{\partial \alpha_k} - \sum_{l=1, p_l \in \boldsymbol{p}_i}^{|\boldsymbol{p}_i|} \frac{\partial f_i}{\partial p_l}(\mathbf{x}, \boldsymbol{p}_i) \frac{\partial p_l}{\partial \alpha_k} = \sum_{l=1}^{n} \frac{\partial f_i(\mathbf{x}, \boldsymbol{p}_i)}{\partial x_l} \frac{\partial x_l}{\partial \alpha_k}.$$

In an earlier work, Sontag [2] used $\alpha_k := p_k \in \boldsymbol{p}_j$, $j \neq i$. This setting necessitates multiple time series, each at a different value of parameter $p_l \in \mathbf{p}_k$ (for some $k \in \{1..n\}$ and some $l \in \{1..|\mathbf{p}_k|\}$) while keeping all other parameters unchanged. This approach is very restricted and is hard to implement in real practice for two reasons. First, for most real world applications, the structure of $f(.)$, and hence $\mathbf{p}_k$ are not defined or known a priori. Second, the procedures for keeping all other parameters unchanged are hard to execute. To overcome the first critical gap, we investigate the setting $\alpha_k := a_k$. The second gap is addressed in Sec. 4.3.2. When $\alpha_k := a_k$, we have

$$\sum_{l=1, p_l \in \boldsymbol{p}_i}^{|\boldsymbol{p}_i|} \frac{\partial f_i}{\partial p_l}(\mathbf{x}, \boldsymbol{p}_i) \frac{\partial \boldsymbol{p}_i}{\partial \alpha_k} = 0.$$

As a result, (4.3) becomes

$$\begin{aligned}\frac{\partial \dot{x}_i(t)}{\partial a_k} &= \frac{\partial f_i(\mathbf{x}, \boldsymbol{p}_i)}{\partial a_k} \\ &= \sum_{l=1}^{n} \frac{\partial f_i(\mathbf{x}, \boldsymbol{p}_i)}{\partial x_l} \frac{\partial x_l}{\partial a_k}.\end{aligned} \tag{4.4}$$

Note here that, intuitively, $\frac{\partial f_i(\mathbf{x}, \boldsymbol{p}_i)}{\partial x_l}$ quantifies the direct influence from node l on node i. $\frac{\partial x_l}{\partial a_k}$ quantifies the response of node l with respect to changes. As a result, Eq. (4.4) can be interpreted as follows. The response of the evolution rate of node i to change, $\frac{\partial \dot{x}_i(t)}{\partial a_k}$, is the sum of the responses of all other nodes l ($l = 1..n$) to change $\frac{\partial x_l}{\partial a_k}$ through the direct influence from other nodes on node i, $\frac{\partial f_i(\mathbf{x}, \boldsymbol{p}_i)}{\partial x_l}$. Gathering all equations of type (4.4) with $i = 1..n, k = 1..n$, we have:

$$\left(\frac{\partial \dot{x}_i}{\partial a_k}\right)_{n\times n} = \left(\frac{\partial x_i}{\partial a_k}\right)_{n\times n} \left(\frac{\partial f_i(\mathbf{x}, \boldsymbol{p})}{\partial x_l}\right)_{n\times n} \tag{4.5}$$

Remark 1. From Eq. (4.5), it follows that $\left(\frac{\partial f_i(\mathbf{x}, \boldsymbol{p})}{\partial x_l}\right)_{n\times n} = \left[\left(\frac{\partial x_i}{\partial a_k}\right)_{n\times n}\right]^{-1} \left(\frac{\partial \dot{x}_i}{\partial a_k}\right)_{n\times n}$, or we can keep track of the system's Jacobian matrix, which captures how the system coupling structure evolves over time, if we can keep track of how the system responds when the initial condition of each variable changes.

Remark 2. In most real-world complex systems, including both natural (biological and biomedical) and engineering (manufacturing, enterprises, and social network) systems, the perturbation procedure corresponding to Eq. (4.5) is easier to implement than the procedure proposed by Sontag *et. al.* [2] because changing the initial concentration of a state variable (e.g., chemical species, genes, buffer level) a_k is much more tenable than changing the reaction parameters, p_k.

Remark 3. It is possible to employ the idea of compressed sensing [1] to reduce the num-

ber of experiments required to solve for the Jacobian matrix when the underlying causal structure is sparse. The authors are currently investigating this aspect, which promises to further enhance the applicability of the proposed approach.

4.3.2 Estimating $\left(\frac{\partial x_i}{\partial a_j}\right)_{n\times n}$, $\left(\frac{\partial \dot{x}_i}{\partial a_j}\right)_{n\times n}$

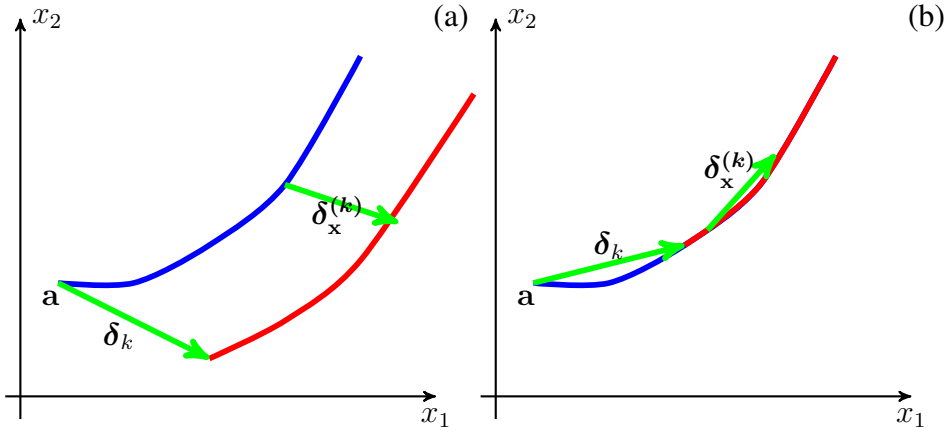

Figure 4.2: Perturbation studies (a) $\boldsymbol{\delta}_k = (\delta_k^{(1)}, ..., \delta_k^{(n)})$, (b) $\boldsymbol{\delta}_k = \mathbf{x}(t_0 + k\Delta t) - \mathbf{x}(t_0)$

In this subsection, we introduce a procedure to infer $\left(\frac{\partial x_i}{\partial a_j}\right)_{n\times n}$, $\left(\frac{\partial \dot{x}_i}{\partial a_j}\right)_{n\times n}$ and hence, $\left(\frac{\partial f_i(\mathbf{x},\boldsymbol{p})}{\partial x_l}\right)_{n\times n}$. We consider two approaches: (1) a general procedure to simultaneously perturb multiple parameters in Theorem 6, and (2) a method to infer $\left(\frac{\partial f_i(\mathbf{x},\boldsymbol{p})}{\partial x_l}\right)_{n\times n}$ from a single time series realization in Corollary 3. First, we write the solution to Eqs. (4.1,4.2) and its derivative as $x_i(t,\boldsymbol{a})$ and $\dot{x}_i(t,\boldsymbol{a})$, respectively. With this notation, we have the following first order approximation:

$$x_i(t,\boldsymbol{a}+\boldsymbol{\delta}_k) - x_i(t,\boldsymbol{a}) \approx \sum_{j=1}^{n} \frac{\partial x_i(t,\boldsymbol{a})}{\partial a_j}\delta_k^{(j)} \tag{4.6}$$

$$\dot{x}_i(t,\boldsymbol{a}+\boldsymbol{\delta}_k) - \dot{x}_i(t,\boldsymbol{a}) \approx \sum_{j=1}^{n} \frac{\partial \dot{x}_i(t,\boldsymbol{a})}{\partial a_j}\delta_k^{(j)}, \tag{4.7}$$

for any perturbation vector $\boldsymbol{\delta}_k = (\delta_k^{(1)}, ..., \delta_k^{(n)})$. The approximations (4.6,4.7) are illustrated in Fig. 4.2a. In this figure, the original trajectory $\mathbf{x}(t, \boldsymbol{a})$ is shown as the dark (blue) line, the perturbed trajectory as a light (red) line; the perturbation vector $\boldsymbol{\delta}_k$ and deviation vector $\boldsymbol{\delta}_{\mathbf{x}}^{(k)} = \mathbf{x}(t, \boldsymbol{a} + \boldsymbol{\delta}_k) - \mathbf{x}(t, \boldsymbol{a} + \boldsymbol{\delta}_k)$ are in green. Gathering all equations of type (4.6) for $k = 1..n$, we have

$$\begin{pmatrix} x_i(t, \boldsymbol{a} + \boldsymbol{\delta}_1) - x_i(t, \boldsymbol{a}) \\ x_i(t, \boldsymbol{a} + \boldsymbol{\delta}_2) - x_i(t, \boldsymbol{a}) \\ \vdots \\ x_i(t, \boldsymbol{a} + \boldsymbol{\delta}_k) - x_i(t, \boldsymbol{a}) \end{pmatrix} = \boldsymbol{\Delta} \begin{pmatrix} \frac{\partial x_i(t,\boldsymbol{a})}{\partial a_1} \\ \frac{\partial x_i(t,\boldsymbol{a})}{\partial a_2} \\ \vdots \\ \frac{\partial x_i(t,\boldsymbol{a})}{\partial a_n} \end{pmatrix}, \tag{4.8}$$

where

$$\boldsymbol{\Delta} = \begin{pmatrix} \delta_1^{(1)} & \delta_1^{(2)} & ... & \delta_1^{(n)} \\ \delta_2^{(1)} & \delta_2^{(2)} & ... & \delta_2^{(n)} \\ \vdots & \vdots & \vdots & \vdots \\ \delta_n^{(1)} & \delta_n^{(2)} & ... & \delta_n^{(n)} \end{pmatrix}$$

Consequently,

$$\begin{pmatrix} x_1(t, \boldsymbol{a} + \boldsymbol{\delta}_1) - x_1(t, \boldsymbol{a}) & ... & x_n(t, \boldsymbol{a} + \boldsymbol{\delta}_1) - x_n(t, \boldsymbol{a}) \\ x_1(t, \boldsymbol{a} + \boldsymbol{\delta}_2) - x_1(t, \boldsymbol{a}) & ... & x_n(t, \boldsymbol{a} + \boldsymbol{\delta}_2) - x_n(t, \boldsymbol{a}) \\ \vdots & & \vdots \\ x_1(t, \boldsymbol{a} + \boldsymbol{\delta}_k) - x_1(t, \boldsymbol{a}) & ... & x_n(t, \boldsymbol{a} + \boldsymbol{\delta}_k) - x_n(t, \boldsymbol{a}) \end{pmatrix} = \boldsymbol{\Delta} \begin{pmatrix} \frac{\partial x_1(t,\boldsymbol{a})}{\partial a_1} & \frac{\partial x_2(t,\boldsymbol{a})}{\partial a_1} & ... & \frac{\partial x_n(t,\boldsymbol{a})}{\partial a_1} \\ \frac{\partial x_1(t,\boldsymbol{a})}{\partial a_2} & \frac{\partial x_2(t,\boldsymbol{a})}{\partial a_2} & ... & \frac{\partial x_n(t,\boldsymbol{a})}{\partial a_2} \\ \vdots & \vdots & ... & \vdots \\ \frac{\partial x_1(t,\boldsymbol{a})}{\partial a_n} & \frac{\partial x_2(t,\boldsymbol{a})}{\partial a_n} & ... & \frac{\partial x_n(t,\boldsymbol{a})}{\partial a_n} \end{pmatrix}. \tag{4.9}$$

This leads to

$$\begin{pmatrix} \frac{\partial x_1(t,\boldsymbol{a})}{\partial a_1} & \frac{\partial x_2(t,\boldsymbol{a})}{\partial a_1} & ... & \frac{\partial x_n(t,\boldsymbol{a})}{\partial a_1} \\ \frac{\partial x_1(t,\boldsymbol{a})}{\partial a_2} & \frac{\partial x_2(t,\boldsymbol{a})}{\partial a_2} & ... & \frac{\partial x_n(t,\boldsymbol{a})}{\partial a_2} \\ \vdots & \vdots & ... & \vdots \\ \frac{\partial x_1(t,\boldsymbol{a})}{\partial a_n} & \frac{\partial x_2(t,\boldsymbol{a})}{\partial a_n} & ... & \frac{\partial x_n(t,\boldsymbol{a})}{\partial a_n} \end{pmatrix} = \boldsymbol{\Delta}^{-1} \begin{pmatrix} x_1(t, \boldsymbol{a} + \boldsymbol{\delta}_1) - x_1(t, \boldsymbol{a}) & ... & x_n(t, \boldsymbol{a} + \boldsymbol{\delta}_1) - x_n(t, \boldsymbol{a}) \\ x_1(t, \boldsymbol{a} + \boldsymbol{\delta}_2) - x_1(t, \boldsymbol{a}) & ... & x_n(t, \boldsymbol{a} + \boldsymbol{\delta}_2) - x_n(t, \boldsymbol{a}) \\ \vdots & \vdots & \vdots \\ x_1(t, \boldsymbol{a} + \boldsymbol{\delta}_k) - x_1(t, \boldsymbol{a}) & ... & x_n(t, \boldsymbol{a} + \boldsymbol{\delta}_k) - x_n(t, \boldsymbol{a}) \end{pmatrix}. \tag{4.10}$$

Similarly, we can derive from (4.7) that

$$\begin{pmatrix} \frac{\partial \dot{x}_1(t,\boldsymbol{a})}{\partial a_1} & \frac{\partial \dot{x}_2(t,\boldsymbol{a})}{\partial a_1} & \dots & \frac{\partial \dot{x}_n(t,\boldsymbol{a})}{\partial a_1} \\ \frac{\partial \dot{x}_1(t,\boldsymbol{a})}{\partial a_2} & \frac{\partial \dot{x}_2(t,\boldsymbol{a})}{\partial a_2} & \dots & \frac{\partial \dot{x}_n(t,\boldsymbol{a})}{\partial a_2} \\ \vdots & \vdots & \dots & \vdots \\ \frac{\partial \dot{x}_1(t,\boldsymbol{a})}{\partial a_n} & \frac{\partial \dot{x}_2(t,\boldsymbol{a})}{\partial a_n} & \dots & \frac{\partial \dot{x}_n(t,\boldsymbol{a})}{\partial a_n} \end{pmatrix} = \boldsymbol{\Delta}^{-1} \begin{pmatrix} \dot{x}_1(t,\boldsymbol{a}+\boldsymbol{\delta}_1) - \dot{x}_1(t,\boldsymbol{a}) & \dots & \dot{x}_n(t,\boldsymbol{a}+\boldsymbol{\delta}_1) - \dot{x}_n(t,\boldsymbol{a}) \\ \dot{x}_1(t,\boldsymbol{a}+\boldsymbol{\delta}_2) - \dot{x}_1(t,\boldsymbol{a}) & \dots & \dot{x}_n(t,\boldsymbol{a}+\boldsymbol{\delta}_2) - \dot{x}_n(t,\boldsymbol{a}) \\ \vdots & \vdots & \vdots \\ \dot{x}_1(t,\boldsymbol{a}+\boldsymbol{\delta}_k) - \dot{x}_1(t,\boldsymbol{a}) & \dots & \dot{x}_n(t,\boldsymbol{a}+\boldsymbol{\delta}_k) - \dot{x}_n(t,\boldsymbol{a}) \end{pmatrix}. \tag{4.11}$$

Replacing Eqs. (4.11,4.10) with Eq. (4.5), we achieve the following theorem to estimate $\left(\frac{\partial f_i(\mathbf{x},\boldsymbol{p})}{\partial x_l}\right)_{n\times n}$:

Theorem 6. *$\left(\frac{\partial f_i(\mathbf{x},\boldsymbol{p})}{\partial x_l}\right)_{n\times n}$ can be estimated by the following formula*

$$\begin{pmatrix} \dot{x}_1(t,\boldsymbol{a}+\boldsymbol{\delta}_1) - \dot{x}_1(t,\boldsymbol{a}) & \dots & \dot{x}_n(t,\boldsymbol{a}+\boldsymbol{\delta}_1) - \dot{x}_n(t,\boldsymbol{a}) \\ \dot{x}_1(t,\boldsymbol{a}+\boldsymbol{\delta}_2) - \dot{x}_1(t,\boldsymbol{a}) & \dots & \dot{x}_n(t,\boldsymbol{a}+\boldsymbol{\delta}_2) - \dot{x}_n(t,\boldsymbol{a}) \\ \vdots & \vdots & \vdots \\ \dot{x}_1(t,\boldsymbol{a}+\boldsymbol{\delta}_k) - \dot{x}_1(t,\boldsymbol{a}) & \dots & \dot{x}_n(t,\boldsymbol{a}+\boldsymbol{\delta}_k) - \dot{x}_n(t,\boldsymbol{a}) \end{pmatrix} = \begin{pmatrix} x_1(t,\boldsymbol{a}+\boldsymbol{\delta}_1) - x_1(t,\boldsymbol{a}) & \dots & x_n(t,\boldsymbol{a}+\boldsymbol{\delta}_1) - x_n(t,\boldsymbol{a}) \\ x_1(t,\boldsymbol{a}+\boldsymbol{\delta}_2) - x_1(t,\boldsymbol{a}) & \dots & x_n(t,\boldsymbol{a}+\boldsymbol{\delta}_2) - x_n(t,\boldsymbol{a}) \\ \vdots & \vdots & \vdots \\ x_1(t,\boldsymbol{a}+\boldsymbol{\delta}_k) - x_1(t,\boldsymbol{a}) & \dots & x_n(t,\boldsymbol{a}+\boldsymbol{\delta}_k) - x_n(t,\boldsymbol{a}) \end{pmatrix} \left(\frac{\partial f_i(\mathbf{x},\boldsymbol{p})}{\partial x_l}\right)_{n\times n}. \tag{4.12}$$

Note that if we can collect multiple time series realizations of a process, each corresponds to one initial condition $\boldsymbol{a}+\boldsymbol{\delta}_k$ of $\mathbf{x}(0)$, and equation Eq. (4.12) can be established to solve for $\left(\frac{\partial f_i(\mathbf{x},\boldsymbol{p})}{\partial x_l}\right)_{n\times n}$. If we can collect only one single time series of the process, we can choose $\boldsymbol{\delta}_k = \mathbf{x}(t_0+k\Delta t) - \mathbf{x}(t_0)$. The perturbed initial condition $\boldsymbol{a}+\boldsymbol{\delta}_k = \mathbf{x}(t_0+k\Delta t)$ will lie on the system trajectory and the perturbed trajectory can be obtained by shifting the original trajectory by k time steps (Fig. 4.2b). As a result, $S(t)$ can be estimated from a single time series $\mathbf{x}(t)$ as in the following corollary.

Corollary 3. *When $\boldsymbol{\delta}_k = \mathbf{x}(t_0+k\Delta t) - \mathbf{x}(t_0)$, $S(t)$ can be estimated from one time series realization of $\mathbf{x}(t)$ based on Eq. (4.12).*

Remark 4. It is more practical to conduct experiments when multiple parameters can be perturbed together as in (4.64.7) than when all other parameters are controlled and only one parameter is changed, as proposed by Sontag *et. al.* [2].

4.3.3 Direct influence inference when the data contains noise

The foregoing formulations ignore the presence of noise in real world systems. Uncertainties exist in both extraneous and intrinsic influences on the essential process dynamics, and these are captured using additive and multiplicative noise terms in the governing equation (4.12). In addition to the presence of noise, the coupling structures of most real world complex systems tend to be sparse, i.e., $S(t)$ is a sparse matrix. Under this very realistic condition, the method developed in our previous work [98] can be extended to infer the network structure. Specifically, $S(t)$ can be estimated by solving the following sparse regression problem

$$\min ||S(t)||_1 \text{ s.t } ||\Gamma(t) - S(t)R(t)||_F \leq \mathcal{E}, \tag{4.13}$$

where $R(t) = \left(\frac{\partial x_i(t)}{\partial a_k}\right)^T_{n\times n}, \Gamma(t) = \left(\frac{\partial \dot{x}_j(t)}{\partial a_k}\right)^T_{n\times n}$, $||.||_F$ is the Frobenius norm of a matrix and $\mathcal{E}$ is bounded as follows

Theorem 7. *[98]*

$$\mathcal{E} \leq (||\Gamma||_F + ||\Delta\Gamma||_F)\frac{||R^{-1}\Delta R||_F}{1 - ||R^{-1}\Delta R||_F} + ||\Delta\Gamma||_F, \tag{4.14}$$

where

$$\begin{aligned}(\Delta R)_{ik}(t) =& \frac{(e_{ik}(t) - e_{ik}(t+\Delta t))}{\delta_k},\\ (\Delta\Gamma)_{ik}(t) =& \frac{(e_{ik}(t+\Delta t) - e_{ik}(t+2\Delta t))}{\Delta t\delta_k} - \frac{(e_{ik}(t) - e_{ik}(t+\Delta t))}{\Delta t\delta_k}\end{aligned}$$

and $e_{ik}(t)$ is the error incurred when measuring $x_i(t)$.

The formulation in Eq. (4.13) with $\mathcal{E}$ estimated as in Eq. (4.14) can be solved using standard optimization packages. Our approach was designed to optimize for sparsity, which as noted earlier, is an essential characteristic of many natural and engineering systems

such as brain physiology, genetic regulatory processes, manufacturing systems, and social networks.

We compared the performance of this method using benchmark data sets from Marbach *et. al.* [8] based on the following performance measures:

1. ρ-metric: it captures the number of absent links ($s^0_{ij} = 0$) that are correctly identified as follows

$$\rho = \sqrt{\frac{1}{n}\sum_{k=1}^{n}\sum_{i,j}(1 - \mathcal{H}(|S^0_{ij}|))(\hat{S}_{ij}(t_k))^2}, \tag{4.15}$$

   where $\mathcal{H}(.)$ is the Heaviside function defined as follows

$$\mathcal{H}(\theta) = \begin{cases} 0 & \text{if } \theta \leq 0 \\ 1 & \text{if } \theta > 0 \end{cases}.$$

   The lower the value of ρ, the better.

2. ξ-metric: it captures the true predictive power of the inference scheme as

$$\xi = -\frac{\log(p_{_{ROC}}) + \log(p_{_{PR}})}{2}, \tag{4.16}$$

   where $p_{_{ROC}}$ and $p_{_{PR}}$ are p-values computed from the area under the reciever operating characteristics curve (AUROC) and the area under the precision-recall curve (AUPR). The higher the value of ξ, the better.

3. Hoyer - metric: it captures the sparsity of the inferred network as follows

$$Hoyer(S) = \frac{n - (\sum_{i,j=1}^{n}|s_{ij}|)/\sqrt{\sum_{i,j=1}^{n} s^2_{ij}}}{n-1},$$

   Note here that $Hoyer(S) \in [0, 1]$. A higher $Hoyer(S)$ means a sparser S.

Our benchmark tests suggest that our approach reduces ρ by 2 orders of magnitude when the noise is underestimated as 10% of the actual, and by 5 orders of magnitude when the noise is over estimated as 10 times the actual. When the underlying network is assumed to be time invariant, compared to other network inference methods [44, 86, 90], ξ evaluated on networks inferred using our approach are increased by 18.53% to 53.03% and 89.09% to 249.7% for networks inferred from E. Coli and Cerevisiae data sets, respectively [98]. The inference error ρ (Eq. (4.15)) is reduced by 2 to 3 orders of magnitude in all cases while the Hoyer measure is increased by 34% to 322.91% and 18.85% to 96.65% for networks inferred from an E. coli data set and Cerevisiae data set, respectively. These results suggest that from our method we are able to infer a sparser network structure with smaller inference error.

4.3.4 Spectral statistic for change detection

As noted earlier, qualitative changes in the dynamics of a complex system are due to structural instabilities. Such qualitative changes can be quantitatively characterized in terms of bifurcations [21]. Mathematically speaking, for a complex system modeled by Eqs. (4.1,4.2), bifurcations are known to take place at parameter setting $\mathbf{p}_i$ if even a small change (perturbation) in the parameter values leads to a qualitative change in the system trajectories, such as a transition from a periodic to an aperiodic or chaotic behavior. Many bifurcations are associated with significant changes in the system's Jacobian matrix $(\frac{\partial f_{ij}}{\partial x_j})_{n\times n}$, such as a drastic reduction in the rank and/or a major change/shift in the eigen system of the matrix.

In this section, we develop a network-based statistic to detect the onset of a structural instability in a process. Most related works in the literature are based on applying control charts to features extracted from the network such as centrality, clustering coefficient, connectivity, density, scan statistics, degree distribution, and diameter [107–111]. Other researchers

extract features from an adjacency matrix by employing decomposition techniques such as singular value decomposition, compact matrix decomposition, or CUR matrix approximation [88]. Recently, Idé *et. al.* [112] have introduced a quantifier for detecting changes based on the inner product between major directions of the current matrix and of the matrix in previous steps defined as follows:

$$\zeta = 1 - \mathbf{u}(t)\boldsymbol{r}(t-1), \tag{4.17}$$

where $\mathbf{u}(t)$ is the eigen vector with the largest eigenvalue of $S(t)$ and $\boldsymbol{r}(t) = \frac{1}{w}\sum_{\tau=t-w+1}^{t}\mathbf{u}(\tau)$. According to Idé *et. al.* [112], $\zeta \propto \exp[-\frac{z}{2\Sigma}]z^{\frac{n-1}{2}-1}$ where Σ is a constant parameter, called the angular variance. Intuitively, ζ captures the change in the main direction of the system trajectory. Here we note that if there is no transient and not much nonlinearity or noise, $\mathbf{u}$ should not change over time and $\zeta \approx 0$. However, as noted in many earlier works, e.g., [113], complex real-world systems, including the brain exhibit significant nonlinearity and are often transient even when no input or stimulus is present. Consequently, ζ exhibits significant variation over time, even under "normal" conditions. Therefore, it fails to differentiate between a normal variation (in the main direction) and a major event like a change in system dimensions. The ζ statistic would identify many false alarms which are not differentiable from major events such as seizures. However, none of the methods employs the degrees of freedom of the system. For events such as seizures, the degree of freedom, the number of independent vectors needed to represent the system, is an important feature because during a seizure, the neurons synchronize, resulting in a drop in the degree of freedom. The degrees of freedom can be captured by a spectral-graph-based statistic, γ_k, defined as follows:

$$\gamma_k := g(\boldsymbol{\lambda}) = \frac{\sum_{i=k}^{n}\lambda_i(t)}{\sum_{i=1}^{n}\lambda_i(t)}, \tag{4.18}$$

where $\lambda_1(t) \geq \lambda_2(t) \geq ... \geq \lambda_n(t)$ are the singular values of $S(t)$. The intuition as to why this statistic captures the degree of freedom is as follows. If γ_k is close to 0, the system trajectory can be captured using a vector space spanned by at most $k-1$ principal components. When the size of the system trajectory is much larger compared to the noise variance [114], γ_k values tend sharply to zero if the system dimensionality decreases from k to below $k-1$. This occurs because if the system trajectory can be captured using at most $k-1$ principal components, γ_k will be almost zero, and its value becomes significantly larger when it takes at least k eigen directions to capture the system dynamics. Therefore, γ_k intuitively captures the dimension of the system trajectory and can be used as an indicator to capture the change in the effective degree of freedom of the system dynamics.

As a dynamic coupling or a direct influence between a pair of nodes in a network representation of a real-world system is often an aggregation of interactions between many sub-processes within each node pair, it is reasonable to assume that each column of S follows a multivariate normal distribution. Particularly, if one rescales the variables, one can reduce each column of S to follow $MVN(\mathbf{0}, \Sigma_0)$, as considered in earlier works [115, 116]. Consequently, the covariance matrix of S follows a Wishart distribution, $W_n(\Sigma_0, n)$ [117].

Related results on the distribution of γ_k in the literature include the Tracy Wisdom distribution on the largest eigenvalue [118], distribution of the smallest eigenvalues [119], and joint distribution of the eigenvalues [120, 121] of a random matrix. However, to the best of our knowledge, there is no such result for the distribution of γ_k in finite cases. To address this gap, we first derive supporting results in Lemmas 3 - 5. Lemma 3 provides the basic structure of the distribution of a linear combination of eigenvalues needed to derive the distribution of the various components that comprise γ_k in Eq. (4.18). Lemmas 4 and 5 provide the expression for the distribution of these components, namely,

$\lambda_i, i \leq p-2, \beta_{p-1} = \sum_{i=k}^{p} \lambda_i, \beta_p = \sum_{i=1}^{p} \lambda_i$ and $(\sum_{i=k}^{n-1} \lambda_i, \sum_{i=1}^{n} \lambda_i)$. Based on these lemmas, we attempt to express the distribution of γ_k in terms of these elemental distributions.

Lemma 3. *Let* $\mathbf{A}(\mathbf{x})$ *be a* $p \times p$ *matrix with the* $(i,j)^{\text{th}}$ *element denoted by* $a_i(x_j)$ *is* x_j^{i-1} *and matrix* A *satisfies* $\mathbf{x} = A^{-1}\mathbf{y}$. $|\mathbf{A}(A^{-1}\mathbf{y})|$ *can be represented as the sum of the products of terms of the form* $y_k^{\alpha_k}$

Proof. According to [121],

$$|\mathbf{A}(\mathbf{x})| = \sum_{n_1=1}^{p} \sum_{n_2=1, n_2 \neq n_1}^{p} sgn(\boldsymbol{n})(a_{n_2}(x_{p-1})a_{n_1}(x_p))|s\tilde{\mathbf{A}}^{(\boldsymbol{n})(2)}(\mathbf{x})|, \tag{4.19}$$

where $\boldsymbol{n} = (n_1, n_2)$, $sgn(\boldsymbol{n}) = sgn(n_1, n_2) = (-1)^{2+i_{n_1}+i_{n_2}}$ where i_{n_l} is the position of the element n_l in the ordered set $\{1, ..., p\} \backslash n_{l-1}$, and $\tilde{\mathbf{A}}^{(\boldsymbol{n})(2)}(\mathbf{x})$ is obtained from $\mathbf{A}(\mathbf{x})$ by deleting the last 2 columns and the rows n_1, n_2. Applying Eq. (4.19) to $\mathbf{x} = (A^{-1}\mathbf{y})$, we have

$$|\mathbf{A}(A^{-1}\mathbf{y})| = \sum_{n_1=1}^{p} \sum_{n_2=1, n_2 \neq n_1}^{p} sgn(\boldsymbol{n})(a_{n_2}(x_{p-1})a_{n_1}(x_p))|\tilde{\mathbf{A}}^{(\boldsymbol{n})(2)}(A^{-1}\mathbf{y})|. \tag{4.20}$$

Note that as $\mathbf{x} = A^{-1}\mathbf{y}$ and the element $(i,j)^{th}$ of $\mathbf{A}(\mathbf{x})$ has the form $a_i(x_j)$,

$$\tilde{\mathbf{A}}^{(\boldsymbol{n})(2)}(A^{-1}\mathbf{y}) = \tilde{\mathbf{A}}^{(\boldsymbol{n})(2)}(\mathbf{y}).$$

Therefore,

$$|\mathbf{A}(A^{-1}\mathbf{y})| = \sum_{n_1=1}^{p} \sum_{n_2=1, n_2 \neq n_1}^{p} sgn(\boldsymbol{n})(a_{n_2}(x_{p-1})a_{n_1}(x_p))|\tilde{\mathbf{A}}^{(\boldsymbol{n})(2)}(\mathbf{y})|. \tag{4.21}$$

Also, as $a_i(x_j) = x_j^{i-1}$ and x_j is a linear combination of y_ks, $a_{n_2}(x_{p-1})$ and $a_{n_1}(x_p)$ can

be written as the sum of the products of terms of the form $y_k^{\alpha_k}$. □

Lemma 4. *The density distribution function $f_{\boldsymbol{\beta}}(\mathbf{y})$ of $\boldsymbol{\beta}$, where $\beta_i = \lambda_{i+1}, i \leq p-2, \beta_{p-1} = \sum_{i=k}^{p} \lambda_i, \beta_p = \sum_{i=1}^{p} \lambda_i$ can be represented as follows:*

$$f_{\boldsymbol{\beta}}(\mathbf{y}) = \frac{1}{det(A)} K |\boldsymbol{\Phi}(A^{-1}\mathbf{y})| . |\boldsymbol{\Psi}(A^{-1}\mathbf{y})| \Pi_{l=1}^{p-2} \xi(y_l) \left(e^{y_{p-1}} \Pi_{i=k}^{p-2} e^{-y_i} e^{y_p} e^{-y_{p-1}} \Pi_{i=1}^{k-1} e^{-y_i} \right).$$

Proof. According to Chiani *et. al.* [120], the joint probability distribution function of the ordered eigenvalues of a Wishart matrix can be written as

$$f_{\boldsymbol{\lambda}}(\mathbf{x}) = K |\boldsymbol{\Phi}(\mathbf{x})| . |\boldsymbol{\Psi}(\mathbf{x})| \Pi_{l=1}^{p} \xi(x_l), \tag{4.22}$$

where $\boldsymbol{\Phi}(\mathbf{x}), \boldsymbol{\Psi}(\mathbf{x}), K$ and $\xi(x_l)$ are defined as in Table 4.1 and $\mathbf{V}_1(\mathbf{x})$ denotes the Vandermonde matrix whose $(i,j)^{\text{th}}$ element is x_j^{i-1}. Consider the transformation $\beta_i = \lambda_{i+1}, i \leq p-2, \beta_{p-1} = \sum_{i=k}^{p} \lambda_i, \beta_p = \sum_{i=1}^{p} \lambda_i$ or $\boldsymbol{\beta} = A\boldsymbol{\lambda}$, where

$$A = \begin{bmatrix} 0 & 1 & & & & & \\ 0 & 0 & 1 & & & & \\ & 0 & \ddots & 1 & & & \\ & 1 & 1 & 1 & \dots & 1 & 1 \\ 1 & 1 & 1 & 1 & \dots & 1 & 1 \end{bmatrix}.$$

By applying the theorem on the distribution of the function of a random vector [122], $f_{\boldsymbol{\beta}}(\mathbf{y})$ can be written as follows:

$$f_{\boldsymbol{\beta}}(\mathbf{y}) = \frac{1}{det(A)} f_{\boldsymbol{\lambda}}(A^{-1}\mathbf{y})$$

$$=\frac{1}{det(A)}K|\mathbf{\Phi}(A^{-1}\mathbf{y})|.|\mathbf{\Psi}(A^{-1}\mathbf{y})|\Pi_{l=1}^{p-2}\xi(y_l)\left(e^{y_{p-1}}\Pi_{i=k}^{p-2}e^{-y_i}e^{y_p}e^{-y_{p-1}}\Pi_{i=1}^{k-1}e^{-y_i}\right), \tag{4.23}$$

where $\mathbf{x}=A^{-1}\mathbf{y}$. □

	K	$\Phi(\mathbf{x})$	$\Psi(\mathbf{x})$	$\xi(x)$
uncorrelated central	$K_{uc}=\left[\Pi_{i=1}^{q}(p-i)!\Pi_{j=1}^{q}(q-j)!\right]^{-1}$	$V_1(\mathbf{x})$	$V_1(\mathbf{x})$	$x^{p-q}e^{-x}$
uncorrelated noncentral	$K_{un}=\frac{\Pi_{i=1}^{q}e^{-\mu_i}}{[(p-q)!]^q\lvert V_1(\boldsymbol{\mu})\rvert}$	$V_1(\mathbf{x})$	$F(\mathbf{x},\mu)$	$x^{p-q}e^{-x}$
correlated central	$K_{cc}=K_{uc}\Pi_{i=1}^{q}(i-1)!\frac{\lvert\Sigma\rvert^{-p}}{\lvert V_2(\boldsymbol{\sigma})\rvert}$	$V_1(\mathbf{x})$	$E(\mathbf{x},\sigma)$	x^{p-q}

Table 4.1: Constants and Matrices in Eq. (4.22) for Uncorrelated Central, Uncorrelated Noncentral and Correlated Central Wishart

Lemma 5. $(\beta_{p-1},\beta_p)=(\sum_{i=k}^{n-1}\lambda_i(t),\sum_{i=1}^{n}\lambda_i(t))$ *follows the distribution of the form*

$$f_{\beta_{p-1},\beta_p}(y_{p-1},y_p)=\sum_{n_1,n_2,n_3,n_4=1,n_1\neq n_2,n_3\neq n_4}^{p}H_{n_1,n_2,n_3,n_4}e^{-y_{p-1}}\psi_{n_2}(y_{p-1})\phi_{n_3}(y_{p-1})\xi(y_{p-1})e^{y_p}\psi_{n_1}(y_p)\phi_{n_4}(y_p)\xi(y_p) \tag{4.24}$$

Proof. The probability distribution function $f_{\beta_{p-1},\beta_p}(y_{p-1},y_p)$ can be computed as follows

$$\begin{aligned}f_{\beta_{p-1},\beta_p}(y_{p-1},y_p)&=\int\frac{1}{det(A)}K|\mathbf{\Phi}(A^{-1}\mathbf{y})|.|\mathbf{\Psi}(A^{-1}\mathbf{y})|\Pi_{l=1}^{p-2}\xi(y_l)\\&\quad\left(e^{y_{p-1}}\Pi_{i=k}^{p-2}e^{-y_i}e^{y_p}e^{-y_{p-1}}\Pi_{i=1}^{k-1}e^{-y_i}\right)dy_1...dy_{p-2}\\&=\int(\psi_{n_2}(x_{p-1})\psi_{n_1}(x_p))|\tilde{\mathbf{\Psi}}^{(\boldsymbol{n})(2)}(\mathbf{y})|(\phi_{n_3}(x_{p-1})\phi_{n_4}(x_p))|\tilde{\mathbf{\Phi}}^{(\boldsymbol{n})(2)}(\mathbf{y})|\\&\quad\Pi_{i=k}^{p-2}e^{-y_i}e^{y_p}e^{-y_{p-1}}\Pi_{i=1}^{k-1}e^{-y_i}dy_1...dy_{p-2}.\end{aligned} \tag{4.25}$$

Using the representation of $\psi_{n_2}(x_{p-1}),\psi_{n_1}(x_p),\phi_{n_3}(x_{p-1}),\phi_{n_4}(x_p)$ in Table 4.1, Eq. (4.25) can be estimated in terms of the multiplication of integrations of the form

$$\int\phi_i(x)\psi_j(x)\tilde{\xi}(x)dx, \tag{4.26}$$

where $\tilde{\xi}(x)$ is the modification of $\xi(x)$ to accommodate the terms $(-y_i)^{\alpha_j}$. The multiplication of these integrations is a factor H_{n_1,n_2,n_3,n_4} or (4.25) become

$$f_{\beta_{p-1},\beta_p}(y_{p-1},y_p) = e^{y_p}e^{-y_{p-1}} \sum_{n_1,n_2,n_3,n_4=1,n_1\neq n_2,n_3\neq n_4}^{p} H_{n_1,n_2,n_3,n_4}\psi_{n_2}(y_{p-1})\psi_{n_1}(y_p)\phi_{n_3}(y_{p-1})\phi_{n_4}(y_p)\xi(y_{p-1})\xi(y_p)$$
$$= \sum_{n_1,n_2,n_3,n_4=1,n_1\neq n_2,n_3\neq n_4}^{p} H_{n_1,n_2,n_3,n_4}e^{-y_{p-1}}\psi_{n_2}(y_{p-1})\phi_{n_3}(y_{p-1})\xi(y_{p-1})e^{y_p}\psi_{n_1}(y_p)\phi_{n_4}(y_p)\xi(y_p).$$

□

Theorem 8. *γ_k follows the distribution of the form*

$$f_{\gamma_k}(x) = -x^{-2}\int z_1 f_{\beta_{p-1},\beta_p}(z_1, z_1/x)dz_1 \tag{4.27}$$

where $f_{\beta_{p-1},\beta_p}(x,y)$ is defined as in Eq. (4.24).

Proof. Consider the transformation $z_1 = y_1, z_2 = y_1/y_2$. $y_1 = z_1, y_2 = z_1/z_2$. $J(z_1,z_2) = \begin{vmatrix} 1 & 0 \\ 1/z_2 & -z_1/z_2^2 \end{vmatrix} = -z_1/z_2^2$. The distribution function $g(z_1,z_2)$ can be computed as follows

$$g(z_1,z_2) = f_{\beta_{p-1},\beta_p}(z_1, z_1/z_2)(-z_1/z_2^2).$$

Therefore, $f(y_1/y_2)$ or $g(z_2)$ can be estimated from $f(y_1, y_1/y_2)$ as follows:

$$\begin{aligned} g(z_2) &= \int g(z_1,z_2)dz_1 \\ &= \int f_{\beta_{p-1},\beta_p}(z_1, z_1/z_2)(-z_1/z_2^2)dz_1 \\ &= -z_2^{-2}\int z_1 f_{\beta_{p-1},\beta_p}(z_1, z_1/z_2)dz_1. \end{aligned}$$

□

The result in Eq. (4.27) guarantees that γ_k follows a distinct distribution, and can therefore be employed to establish control charts to detect changes in the system dynamics.

However, computing this function is not straightforward. It involves computing multiple integrations of the form in Eq. (4.26). Therefore, an approximation expression will be very useful in practice. In a finite case, Fig 4.3 shows the distribution of γ_k based on

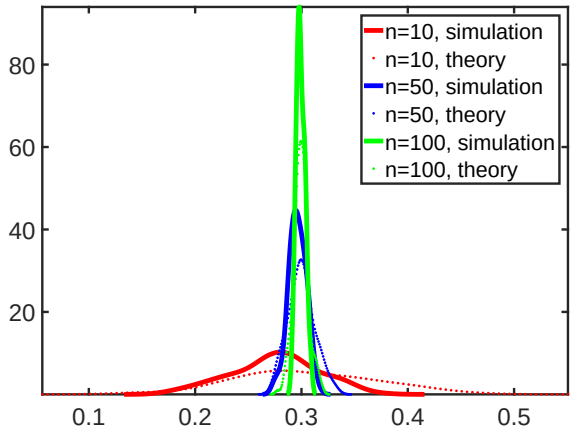

Figure 4.3: Distribution of γ_k using simulation (solid line) and using Theorem 9 for different values of n

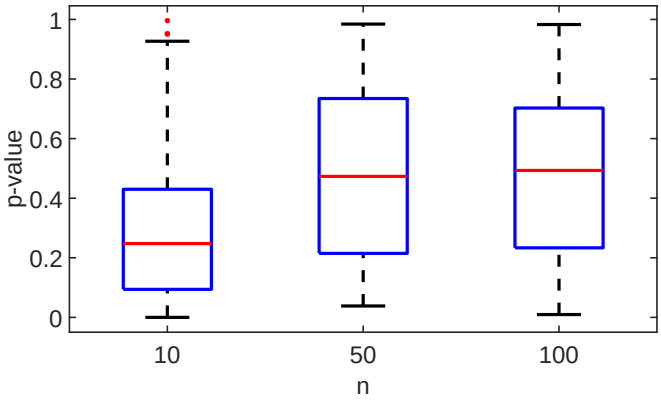

Figure 4.4: Distribution of $p-$value of χ^2 normality test of γ_k

a simulation and as predicted by Theorem 9 when $n = 10$, 50 and 100, respectively.

As shown in this figure, as n increases, the distribution of γ_k converges to the normal distribution as predicted by Theorem 9. The corresponding $p-$values of the χ^2 normality test of γ_k for these cases, shown in Fig. 4.4, is about 0.4 on average when n is greater than 50 and more than 0.2 when $n = 10$. More generally, when n is large, we have the following result.

Theorem 9. *When n is large enough, γ_k computed from the covariance matrix of $S_{n\times n}$ follows the distribution $N(\mu_{\gamma_k}, \sigma^2_{\gamma_k})$ where $\sigma^2_{\gamma_k} = 2\Phi'\Sigma_0\Phi$, $\Phi = \frac{\partial f(\boldsymbol{\lambda})}{\partial \boldsymbol{\lambda}}|_{\boldsymbol{\lambda}=\boldsymbol{l}}$, and $l_1 \geq l_2 \geq ... \geq l_n$ are singular values of S.*

Proof. According to Theorem 13.5.1 [122], when n is large, $\sqrt{n}(\lambda_i - l_i)$ are independent and $\sqrt{n}(\lambda_i - l_i) \sim N(0, 2l_i^2)$. Applying Theorem 4.2.3 [122] to $f(\boldsymbol{\lambda}) = \frac{\sum_{i=k}^{n} \lambda_i(t)}{\sum_{i=1}^{n} \lambda_i(t)}$, we have $\sqrt{n}(\gamma_k - f(\boldsymbol{l})) \sim N(0, \sigma^2_{\gamma_k})$, where $\sigma^2_{\gamma_k} = 2\Phi'\Sigma_0\Phi$, $\Phi = \frac{\partial f(\boldsymbol{\lambda})}{\partial \boldsymbol{\lambda}}|_{\boldsymbol{\lambda}=\boldsymbol{l}}$. Therefore, $\gamma_k \sim N(f(\boldsymbol{l}), \frac{\sigma^2_{\gamma_k}}{n})$, □

From this result, it follows that the γ_k statistic can be employed in a change detection chart. In this chapter, we used a Shewhart chart; however, other types of control charts such as CUSUM and EWMA charts can also be employed.

4.4 Implementation details and results

In this section we report the results oftwo case studies. The first case study considers detecting switches in a time series simulated from a piecewise linear system. In the second case study, we apply our method to the problem of seizure detection using EEG signals. The performance of our change detection statistic, γ_k, is compared with the benchmark ζ-statistic [112] defined in Eq. (4.17).

4.4.1 Numerical case study

The aim of this case study is twofold: First, to evaluate the performance of our network inference method in Eq. (4.12) when applied to the time series outputs of a known

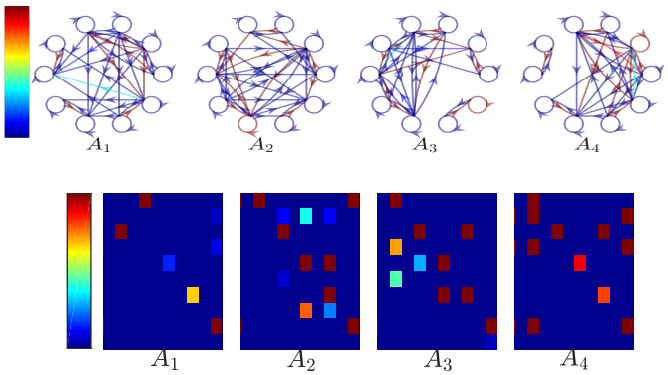

Figure 4.5: Network representation of A_is in the first 4 pieces

interconnected dynamic system and second, to assess the performance of γ_k in detecting the switches. Here, we consider a network represented by a 10 - dimensional piecewise linear system composed of 40 pieces, each of which has the following form:

$$\dot{\mathbf{x}} = A_i\mathbf{x}, T_i \leq t < T_{i+1}, i = \{1, 2, ..., 40\} \tag{4.28}$$

$$T_i = 3(i-1), \tag{4.29}$$

where the initial condition $\mathbf{x}(0) = \mathbf{a}$ is generated randomly from $N(0, 1)$ and the Jacobians A_i are generated randomly with eigenvalues $-2 + j, -2 - j$, $-3, -4, ...,-12$, where $j^2 = -1$. Note here that if Eq. (4.28) is written in the form of Eq. (4.1), we have $S(t) = A_i$ when $T_i \leq t < T_{i+1}$. The network representations of A_i in the first four pieces ($i = 1, 2, 3, 4$, and $t \leq 12$) are shown in Fig 4.5 (top row) and the color maps of the corresponding adjacency matrix A_i are shown in the bottom row. The color in the top row represents the weight on the edges where red is being the highest and blue is being the lowest. The color in the bottom row represents the magnitude of the weights on edges, where blue represents 0 and red represents the maximum value. As shown in the bottom row of the figure, the blue color is dominant, as we focus on simulating a case in which adjacency matrices are sparse, which is an expected characteristic of many real-

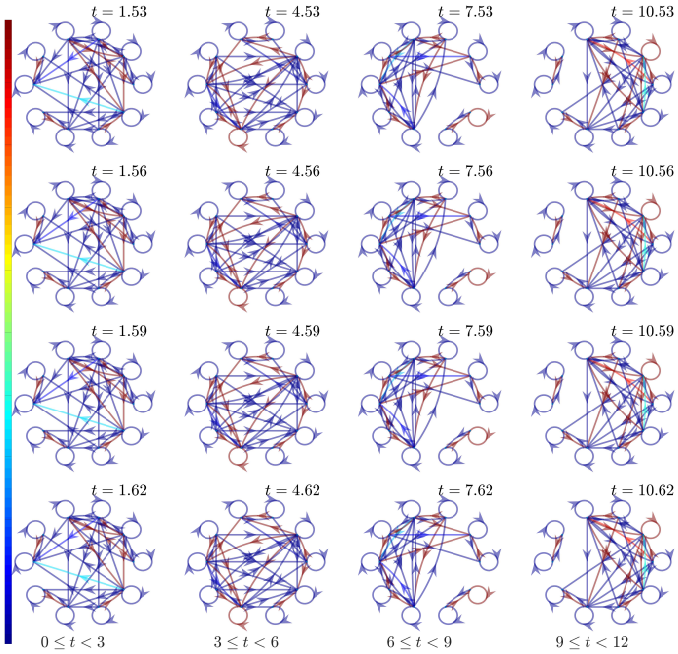

Figure 4.6: $\hat{A}_i$ in the first 4 pieces

world systems [73, 74]. System (4.28) simulates a scenario where the network switches connections every three time units.

In a noise free case, i.e., $\hat{\mathbf{x}}(t) = \mathbf{x}(t)$, by applying Eq. (4.12) to the time series output $\hat{\mathbf{x}}(t)$, $\hat{A}_i$ are computed with the error $||A_i - \hat{A}_i||$ in the order of 10^{-11}. Fig. 4.6 shows the networks reconstructed at different time points in the first 4 pieces ($t \leq 12$). As shown in this figure, the reconstructed networks are the same in each piece and are identical to the ground truth networks in Fig. 4.5, verifying that our network inference method works well in this case.

Next, we consider an additive noise case, $\hat{\mathbf{x}}(t) = \mathbf{x}(t) + \varepsilon(t)$ where $\varepsilon(t) \sim N(0, \sigma^2)$ and σ^2 are set to be 0.1%, 1%, and 10% of the variance of $\mathbf{x}(t)$. We first reconstruct network $\hat{A}_i$ from $\hat{\mathbf{x}}(t)$, then compute γ_k to detect the switches. The performance of γ_k in detecting the switches is evaluated using a modified receiver operating characteristic

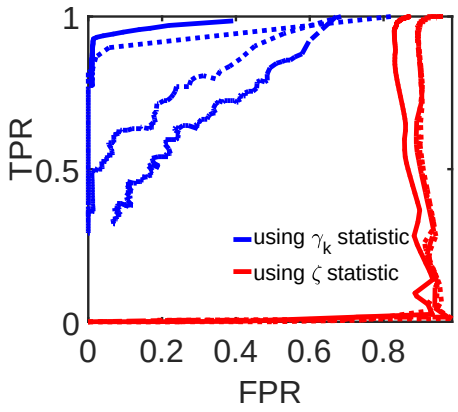

Figure 4.7: Modified ROC curves without measurement noise (—), with simulated measurement noise of 0.1%(·····), 1% (- -) and 10% (—·) of the magnitude of the time series, respectively.

curve (mROC) analysis [123] with a false positive rate (FPR) and true positive rate (TPR) defined as follows:

$$FPR = \frac{\text{\# alarms} - \text{\# change points correctly detected}}{\text{\# alarms}}, \tag{4.30}$$

$$TPR = \frac{\text{\# change points correctly detected}}{\text{\# change points}}. \tag{4.31}$$

Fig 4.7 shows the mROC curves of the γ_k statistic and the ζ statistic in detecting the switches for different cases. As shown in this figure, the mROC curves of γ_k (blue) are always above those of the ζ statistic (red). This suggests that γ_k performs better than ζ in all cases. Here, we notice a "non-standard" trend in the mROC curves, which is due to the fact that our switch detection problem is not a standard binary classification problem, as pointed out in [123]. Quantitatively, the modified area under the curve (mAUC) values for comparison are reported in Table 4.2. mAUC values for the γ_k statistic are close to 1 in most cases, while those values for the ζ statistic are approximately zero. These results indicate that the γ_k statistic works well while the ζ statistic is not able to detect the

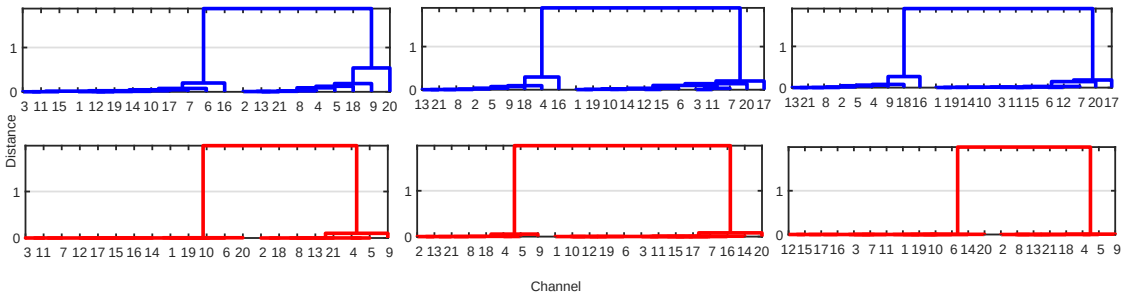

Figure 4.8: Columns of $S(t)$ generated from data of patient 1 can be grouped into clusters of similar patterns non-seizure (blue) and seizure (red).

switches.

Statistic \ Noise level	No noise	0.1%	1%	10%
γ_k statistic	0.96	0.94	0.80	0.63
ζ statistic	0.15	0.071	0.070	0.068

Table 4.2: Modified AUC values

4.4.2 Graph-based seizure detection using EEG signals

Epilepsy is one of the most common neurological diseases, affecting about 50 million people worldwide [124]. This disease, which is caused by excessive or synchronous neuronal activities in the brain, often causes a patient to lose control and can lead to serious injuries or death. Early detection of epilepsy seizures using EEG signals is therefore necessary for preventing these consequences. A challenging problem in this context is to identify a sensitive, seizure detection statistic [125].

To demonstrate the effectiveness of our proposed spectral-based statistic in detecting seizures, we use a data set of 21 EEG signals, sampled at 256 Hz [106, 126]. First, the network capturing the influence of one channel on others, represented by the adjacency

matrix $S(t)$, is inferred using Eqs. (4.12 - 4.14). Here, a node represents an EEG channel or the corresponding region of the brain where the electrode is placed. The weight on the edge from node i to node j, given by $S_{ij}(t)$, quantifies the direct influence from channel i to channel j. Second, γ_k is estimated from $S(t)$, and the control chart is constructed at confidence level $\alpha = 0.05$.

The analysis of $S(t)$ for a representative subject is reported in Figs 4.8-4.10. In each figure, the plots are generated from consecutive samples immediately before and after a seizure occurs. Specifically, Fig. 4.8 shows the hierarchical cluster tree of the influence of one network node or EEG channel on others during non-seizure (blue) and during seizure (red) conditions. In this tree, each leaf represents a node or an EEG channel. The influence of one node on other nodes is quantified by its outgoing weight vector. The distance measure to quantify the similarity of the influence of any two nodes is estimated by the correlation between the corresponding outgoing weight vectors. As shown in this figure, there are roughly two clusters of similar influence patterns for both seizure and non-seizure stages. This indicates that on a large scale, different parts of the brain influence each other in similar ways. The dynamics of the human brain is actually a low-dimensional process and probably can be controlled by two degrees of freedom. Using a small distance threshold (e.g. 0.1), the number of clusters of influence patterns drops from 5 during a non-seizure to 2 during a seizure, suggesting that the number of influence patterns is smaller during a seizure stage than during a non-seizure stage.

To further understand the dimension of the dynamics of brain activity, we analyze the principal components of $S(t)$. The results of this analysis are reported in Fig. 4.9. In each plot, the horizontal axis, k, represents the index of principal components and the vertical axis represents the percentage of variation in $S(t)$ captured by the principal components. As shown in the bottom plots of Fig. 4.9, during a seizure, the first principal component of $S(t)$ captures most of the variation in $S(t)$ while during a non-seizure, more principal

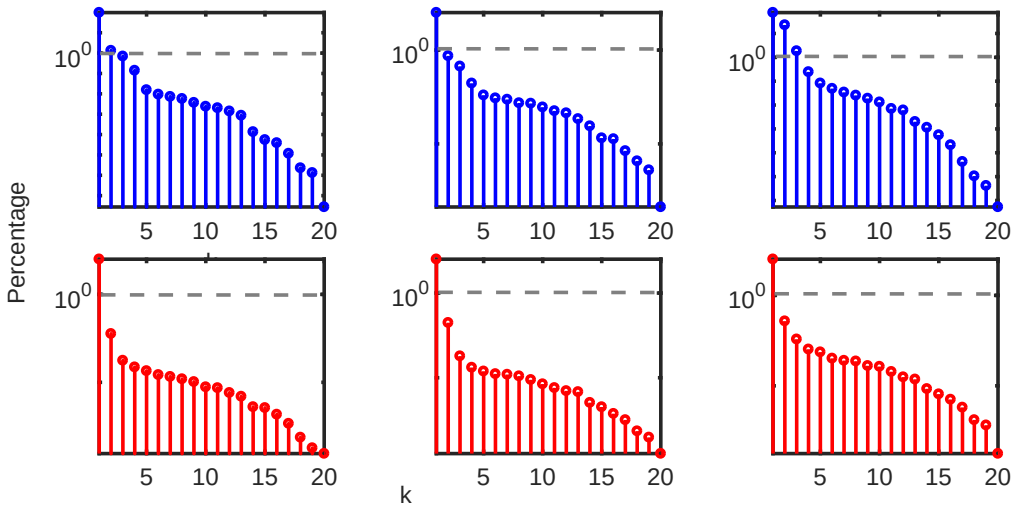

Figure 4.9: The trend of the percentage variance of $S(t)$ captured by each principal component during non-seizure (blue) and seizure (red).

components are required to represent $S(t)$; that is, a higher dimension space is required to represent $S(t)$ during a non-seizure than during a seizure. This matches well with the physiology of the process, as during a seizure, signals emitted from neurons are highly synchronized [127, 128]. As a result, the degree of freedom of the system dynamics is expected to decrease.

Fig. 4.10 shows the similarity in the influence of the nodes before a seizure occurs (top row) and after a seizure occurs (bottom row). In each plot, the horizontal and vertical axes represent the node index and the color represents the similarity between the outgoing weight vectors of the nodes, with red representing maximal similarity. The similarity in the influence of the nodes is more homogeneous (fewer colors) during a seizure than a non-seizure. Hence, the influence of brain regions on each other is more homogeneous during a seizure than a non-seizure. In addition, as shown in this figure, the network structure changes slightly from one sample to another. This change might be due to the fact that brain networks change topology during both seizures and non-seizures [129]. In other

words, brain networks tend to switch connections while maintaining the total number of connection patterns during a healthy stage.

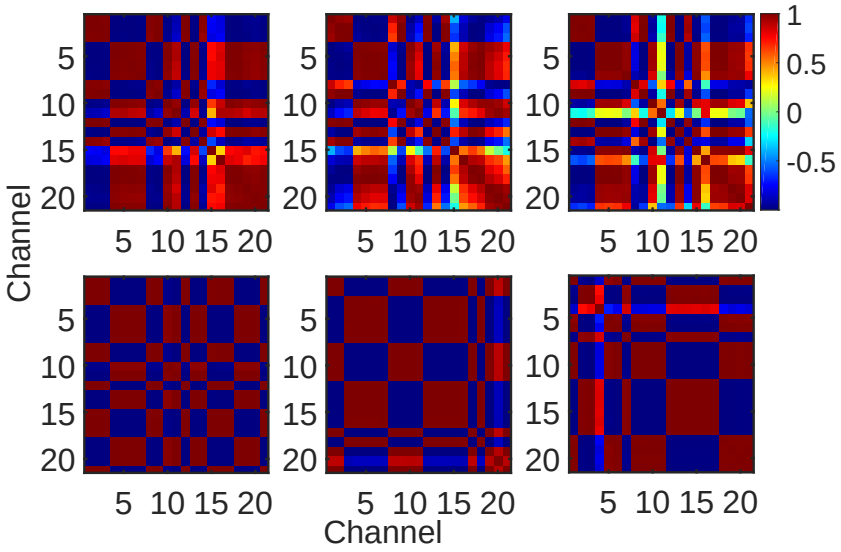

Figure 4.10: Similarity of influence of one channel to others during non-seizure (top row) and seizure (bottom row).

Fig. 4.11 reports the seizure detection rate among all patients at $\alpha = 0.05$ using γ_k with $k = 4$ and using ζ statistics. γ_k can detect seizures with a detection rate of more than 60% in about 40% of the patients while ζ [112] does not detect any seizures. The overall detection rate of the γ_k statistic is 37.59%, compared to 0% using the ζ statistic.

Last, we study the effect of the γ_k feature when employed with other seizure detection methods in the literature. As a demonstration, we consider the random forest model with the features including mean, variance, skewness, kurtosis, line length, and power spectrum in the bands alpha, beta, and gamma and the power spectrum ratio extracted from each EEG signal. Random forest was chosen as it has been shown to perform among the best seizure detection methods [130] while these features were chosen because they capture

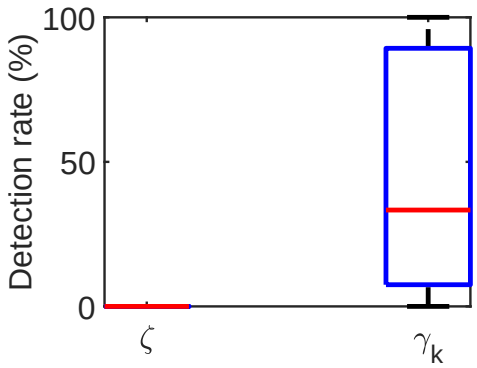

Figure 4.11: Seizure detection rate using γ_k and ζ statistics

the physiology of the process. Specifically, for each patient, two types of random forests are constructed: the orginal one [130] and the one augmented by the γ_k feature. All random forests are composed of 1000 trees and were trained using 80% of the data and tested using 20% of the data. Fig. 4.12 compares the testing error of the random forest model employing the γ_k feature with the original random forest model. The horizontal axis represents patient index and the vertical axis represent the seizure detection rate. As shown in this figure,γ_k improves the testing error by more than 5% in 35% of the cases while maintaining the detection accuracy in most other cases. On average, the detection rate is improved by about 1%. Note that as the random forest model implemented in [130] is among the best models in seizure detection, reducing its generalization error rate is a challenging problem. In this context, the improvement of 5% that the γ_k feature provides is very useful. Thus, the γ_k feature can be employed to improve the accuracy of seizure detection methods such as the random forest.

This analysis suggests that the inferred network $S(t)$ and the γ_k statistic can capture the physiology of an EEG signal while maintaining a good seizure detection rate in many cases. Therefore, γ_k can be used in addition to current statistics for seizure detection. The advantage of this statistic is that it provides insights into causes due to structural changes,

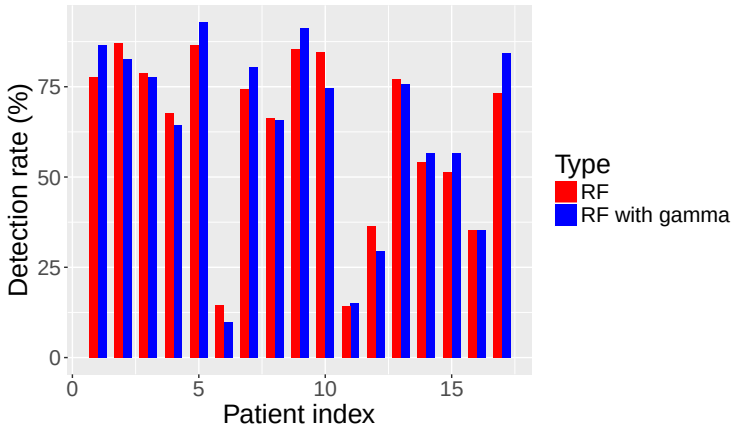

Figure 4.12: Performance comparison of random forest and random forest with γ_k feature added

e.g., which neural connections change during a seizure.

4.5 Conclusions

In this chapter, we have addressed the problem of identifying a sensitive change detection statistic in multivariate time series. Our contributions are twofold. First, we have developed a method to infer a dynamic causal network from a single transient multivariate time series. Second, we have introduced a spectral-graph-based statistic, γ_k, to detect changes in system dynamics. We have also devised closed form and approximation formulas for the distributions of γ_k, which are the foundation for developing quality control charts. In a simulation, when there is no measurement noise, the AUCs are 0.96 and 0.15 for the γ_k statistic and the benchmark ζ statistic, respectively. AUCs when using γ_k for the signal with 0.1%, 1%, and 10% noise are 0.94, 0.80, and 0.63, respectively while the AUC when using the ζ statistic is about 0.07 in all cases. In detecting seizures using EEG signals, the γ_k statistic by itself is able to detect seizure with detection rate of 38% while the ζ statistic is not able to detect any seizures. These results together with the analysis of the network structure $S(t)$ inferred from data from a representative patient show that

our method can capture the physiology of EEG signals while maintaining a good change detection rate. They suggest that the γ_k statistic can be added to the current set of features to improve the performance of current seizure detection methods. The γ_k statistic can identify the time when the changes occur and can also specify the underlying coupling structure that corresponds to the change.

5. CONCLUSIONS

This dissertation studied the problem of modeling the coupling dynamics in real-world systems from three different perspectives. On small-scale, we considered modeling the coupling dynamics between degeneration and regeneration processes, which are the dynamics of an individual node in a network. On large-scale or network level, we considered modeling the coupling dynamics exists in the form of direct influence from one node to another. Finally, we developed a change detection statistic based on the inferred network model. In the following subsections, we summarize our findings and suggest future research directions.

5.1 Summary

The major contributions of this study are as follows:

- In the first problem, we introduced a model that captures the coupled dynamics between regeneration and regeneration processes. Interactions between breakdown and repair dynamics that influence downtime distributions in manufacturing systems were explicitly considered, and dependencies beyond correlations between the time between failures (TBF) and the time to repair (TTR) were captured. The periodic solutions of the model capture the progressive evolution of long time-scale failure and repair patterns. The distribution of short time-scale failure–repair cycles can be captured by providing a class of random perturbations to certain model parameters. We provided sufficient conditions for the existence and stability of the resulting non-linear stochastic differential equation (n-SDE) model solutions that mimic the breakdown and repair patterns observed in many real-world manufacturing systems, namely, fairly regular (periodic) large breakdown and repair cycles, interspersed with highly right skewed distributions of short cycles. We also defined the basin

of attraction for the periodic orbit. The n-SDE model was parametrized using real-world datasets acquired from an automotive manufacturing assembly line segment, and the model solutions were compared with actual observations of TBF and TTR patterns, as well as the performance of the process. Our approach reduced the computation time by about 25% when compared to a discrete-event simulation model, which uses conventional TBF and TTR distributions, implemented on a commercial platform. Experimental investigations also suggested that the model can capture the correlations and non-linear coupled dynamics that exist in real-world operations among TBF and TTR, which are typically ignored in traditional approaches.

- In the second problem of modeling coupled dynamics at the network/system level, we reported a sparse regression (referred to as the ℓ_1-min) approach with theoretical bounds on the constraints on the allowable perturbation to recover the network structure that guarantees sparsity and robustness to noise. We also introduced averaging and perturbation procedures to further enhance prediction scores (i.e., reduce inference errors), and the numerical stability of ℓ_1-min approach. Extensive investigations have been conducted with multiple benchmark simulated genetic regulatory network and Michaelis-Menten dynamics, as well as real-world datasets from DREAM5 challenge. These investigations suggested that our approach can significantly improve, often times by 5 orders of magnitude over the methods reported previously for inferring the structure of dynamic networks, such as Bayesian network, network deconvolution, silencing and modular response analysis methods based on optimizing for sparsity, transients, noise and high dimensionality issues.

- In the third problem, we developed a network-based change detection method for multivariate time series. In particularly, we presented an approach based on spectral graph theory to detect changes in complex dynamic systems that are high di-

mensional and noisy using a single realization of time series data collected under specific types of common transient condition such as intermittency. In this problem, the method developed in problem 2 was extended to apply to the case when only one time series is available. A spectral statisticγ_k was introduced to detect change in system dynamics. We showed that under certain conditions, the statistic follows a normal distribution and it can be employed to construct a change detection procedure to detect qualitative changes in the coupling structure of the dynamic system. Experimental investigations suggested that γ_k statistic by itself is able to detect changes with modified area under curve (mAUC) equal to 0.96 (in simulation) and detect seizures from EEG signal with detection rate of about 40%. Therefore, γ_k can serve as an effective feature to detect change.

5.2 Future research

In the future, we planed to extend the research in the following directions:

1. In this problem, we are interested in controling the heat propagation process inside a fuel cell. Fuel cell is an ideal source of energy. It is both environmental friendly and efficient. The only by-product from combining hydrogen and oxygen in a fuel cell is water, so fuel cells do not emit gas.They are also twice as efficient as internal combustion engine. Fuel cells can be used to converts the chemical energy in the fuel to electricity with efficiencies of up to 60%. In addition, fuel cells are quiet when operating. However, the current issue with fuel cells is their high cost caused by the total lost when a cell breaks down. The main reason why a fuel cell breaks down is that certain internal regions of the cell is overheated. Developing a method to monitor and control internal temperature of a fuel cell is therefore necessary in manufacturing a cost effective fuel cell. Mathematically, the heat propagation pro-

cess inside a fuel cell can be modeled by the following equation:

$$\dot{x}_i(t) = f_i(\mathbf{x}, \boldsymbol{p}_i, \mathbf{u}, t), i = 1..n \tag{5.1}$$

$$x_i(0) = a_i, \tag{5.2}$$

where $\mathbf{u}$ is a control input. The challenge here is that $\mathbf{f}(\mathbf{x}, \boldsymbol{p}_i, \mathbf{u}, t)$ is unknown and difficult to identify from data. Here, we propose a network-based method, which is an extension of the method developed in Section 4, to model and control the heat propagation process inside a fuel cell. A node in this network represents the position of an in situ sensor located inside the cell. The weight on an edge represents the rate at which the heat propagates from one node to another, defined as $s_{ij}(t) = \frac{\partial f_j}{\partial x_i}$. Physically, $(s_{ij}(t))$ estimates the Jacobian of $\mathbf{f}(\mathbf{x}, \boldsymbol{p}_i, \mathbf{u}, t)$. The challenge here is that $(s_{ij}(t))$ can not be inferred by directly applying the method developed in Section 4 because of the existence of control input $\mathbf{u}$. In addition, we also need to estimate the coeficients associated with the input vector $\mathbf{u}$.

2. In the second project, we will apply the network inference method and the change detection statistic introduced in Section 4 to fMRI dataset to develop a network representation of human brain. According to the NSF BRAIN initiative, understanding how individual cells or parts of human brains interact is the key in solving many challenging problems, including treating and preventing brain disorders, and understanding the mechanism under which a human body record and process vast amount of information in very short time. The network model developed from this research direction can be used to detect onset of diseases such as brain cancer and other nervous system disorders or traumatic brain injury. In addition, It can be used facilitate other study on brain-inspired smart technologies to meet societal needs in the future.

REFERENCES

[1] E. J. Candes, J. K. Romberg, T. Tao, Stable signal recovery from incomplete and inaccurate measurements, Communications on Pure and Applied Mathematics 59 (8) (2006) 1207–1223.

[2] E. Sontag, A. Kiyatkin, B. N. Kholodenko, Inferring dynamic architecture of cellular networks using time series of gene expression, protein and metabolite data, Bioinformatics 20 (12) (2004) 1877–1886.

[3] V. S. Kouikoglou, Y. A. Phillis, Hybrid Simulation Models of Production Networks, Kluwer Academic, New York, 2001.

[4] S. Kachani, G. Perakis, Fluid dynamics models and their applications in transportation and pricing, European Journal of Operational Research 170 (2) (2006) 496 – 517.

[5] V. G. Kulkarni, Fluid models for single buffer systems, in: J. H. Dshalalow (Ed.), Frontiers in queueing, Vol. 7, CRC Press, Inc., Boca Raton, FL, USA, 1997, pp. 321–338.

[6] D. J. Watts, S. H. Strogatz, Collective dynamics of 'small-world' networks, nature 393 (6684) (1998) 440–442.

[7] A. Pogromsky, H. Nijmeijer, Cooperative oscillatory behavior of mutually coupled dynamical systems, IEEE Transactions on Circuits and Systems I: Fundamental Theory and Applications 48 (2) (2001) 152–162.

[8] D. Marbach, J. C. Costello, R. Küffner, N. M. Vega, R. J. Prill, D. M. Camacho, K. R. Allison, M. Kellis, J. J. Collins, G. Stolovitzky, et al., Wisdom of crowds for robust gene network inference, Nature Methods 9 (8) (2012) 796–804.

[9] D. A. Drachman, Do we have brain to spare?, Neurology 64 (12) (2005) 2004–2005.

[10] D. Picchioni, J. H. Duyn, S. G. Horovitz, Sleep and the functional connectome, Neuroimage 80 (2013) 387–396.

[11] C. Cheng, A. Sa-Ngasoongsong, O. Beyca, T. Le, H. Yang, Z. J. Kong, S. T. Bukkapatnam, Time series forecasting for nonlinear and non-stationary processes: a review and comparative study, IIE Transactions 0 (0) (2015) 1–19.

[12] F. S. Chance, L. Abbott, A. D. Reyes, Gain modulation from background synaptic input, Neuron 35 (4) (2002) 773–782.

[13] E. Salinas, P. Thier, Gain modulation: a major computational principle of the central nervous system, Neuron 27 (1) (2000) 15–21.

[14] U. Mittal, H. Yang, S. T. S. Bukkapatnam, L. G. Barajas, Dynamics and performance modeling of multi-stage manufacturing systems using nonlinear stochastic differential equations, in: CASE IEEE International Conference on Automation Science and Engineering, 2008, pp. 498–503.

[15] J. P. Kharoufeh, S. M. Cox, M. E. Oxley, Reliability of manufacturing equipment in complex environments, Annals of Operations Research 209 (1) (2013) 231–254.

[16] L. Cui, W. Kuo, H. T. Loh, M. Xie, Optimal allocation of minimal and perfect repairs under resource constraints, IEEE Transactions on Reliability 53 (2) (2004) 193–199.

[17] E. A. Elsayed, An optimum repair policy for the machine interference problem, Journal of the Operational Research Society 32 (9) (1981) 793–801.

[18] Q. Zheng, X. Hong, S. Ray, Nonlinear resource allocation in restoration of compromised systems, in: IEEE International Conference on Communications, Vol. 1, Istanbul, 2006, pp. 429–434.

[19] S. Han, K. G. Shin, Efficient spare-resource allocation for fast restoration of real-time channels from network component failures, in: The 18th IEEE Real-Time Systems Symposium, San Francisco, CA, 1997, pp. 99–108.

[20] Y. H. Kim, L. C. Thomas, Repair strategies in an uncertain environment: Markov decision process approach, Journal of the Operational Research Society 57 (8) (2006) 957–964.

[21] H. K. Khalil, J. Grizzle, Nonlinear systems, Vol. 3, Prentice hall Upper Saddle River, 2002.

[22] J. M. Gonçalves, Regions of stability for limit cycle oscillations in piecewise linear systems, IEEE Transactions on Automatic Control 50 (11) (2005) 1877–1882.

[23] G. Davrazos, N. T. Koussoulas, A review of stability results for switched and hybrid systems, in: Proceedings of 9th Mediterranean Conference on Control and Automation, 2001.

[24] A. H. Jazwinski, Stochastic Processes and Filtering Theory, Academic Press, New York, 1970.

[25] A. Papoulis, S. U. Pillai, Probability, Random Variables, and Stochastic Processes, McGraw-Hill, New York, NY, 2002.

[26] S. M. Ross, Introduction to Probability Models, Academic Press, San Diego, CA, 2009.

[27] S. Bukkapatnam, M. Malshe, P. Agrawal, L. Raff, R. Komanduri, Parametrization of interatomic potential functions using a genetic algorithm accelerated with a neural network, Physical Review B 74 (22) (2006) 224102.

[28] D. Elliott, Sigmoidal transformations and the trapezoidal rule, ANZIAM Journal 40 (1998) 77–137.

[29] B. I. Yun, An extended sigmoidal transformation technique for evaluating weakly singular integrals without splitting the integration interval, SIAM Journal on Scientific Computing 25 (1) (2003) 284–301.

[30] J. H. Holland, Adaptation in Natural and Artificial Systems: An Introductory Analysis with Applications to Biology, Control, and Artificial Intelligence, MIT Press, Cambridge, MA, 1992.

[31] R. R. Inman, Empirical evaluation of exponential and independence assumptions in queueing models of manufacturing systems, Production and Operations Management 8 (4) (1999) 409–432.

[32] H. Yang, S. T. S. Bukkapatnam, L. G. Barajas, Local recurrence-based performance prediction and prognostics in the nonlinear and nonstationary systems, Pattern Recognition 44 (8) (2011) 1834–1840.

[33] N. Marwan, R. M. Carmen, M. Thiel, J. Kurths, Recurrence plots for the analysis of complex systems, Physics Reports 438 (5) (2007) 237–329.

[34] T. Chen, H. L. He, G. M. Church, et al., Modeling gene expression with differential equations., in: Pacific Symposium on Biocomputing, Vol. 4, 1999, p. 4.

[35] D. Napoletani, T. D. Sauer, Reconstructing the topology of sparsely connected dynamical networks, Physical Review E 77 (2) (2008) 026103.

[36] W.-X. Wang, R. Yang, Y.-C. Lai, V. Kovanis, M. A. F. Harrison, Time series based prediction of complex oscillator networks via compressive sensing, EPL (Europhysics Letters) 94 (4) (2011) 48006.

[37] W.-X. Wang, R. Yang, Y.-C. Lai, V. Kovanis, C. Grebogi, Predicting catastrophes in nonlinear dynamical systems by compressive sensing, Physical review letters 106 (15) (2011) 154101.

[38] A. Chiuso, G. Pillonetto, A bayesian approach to sparse dynamic network identification, Automatica 48 (8) (2012) 1553–1565.

[39] N. Friedman, M. Linial, I. Nachman, D. Pe'er, Using bayesian networks to analyze expression data, Journal of Computational Biology 7 (3-4) (2000) 601–620.

[40] N. Friedman, Inferring cellular networks using probabilistic graphical models, Science 303 (5659) (2004) 799–805.

[41] M. Zou, S. D. Conzen, A new dynamic bayesian network (dbn) approach for identifying gene regulatory networks from time course microarray data, Bioinformatics 21 (1) (2005) 71–79.

[42] W. C. Young, A. E. Raftery, K. Y. Yeung, Fast bayesian inference for gene regulatory networks using scanbma, BMC Systems Biology 8 (1) (2014) 47.

[43] S. M. Hill, Y. Lu, J. Molina, L. M. Heiser, P. T. Spellman, T. P. Speed, J. W. Gray, G. B. Mills, S. Mukherjee, Bayesian inference of signaling network topology in a cancer cell line, Bioinformatics 28 (21) (2012) 2804–2810.

[44] S. Feizi, D. Marbach, M. Médard, M. Kellis, Network deconvolution as a general method to distinguish direct dependencies in networks, Nature Biotechnology 31 (8) (2013) 726–733.

[45] B. Barzel, A.-L. Barabási, Network link prediction by global silencing of indirect correlations, Nature Biotechnology 31 (8) (2013) 720–725.

[46] B. N. Kholodenko, A. Kiyatkin, F. J. Bruggeman, E. Sontag, H. V. Westerhoff, J. B. Hoek, Untangling the wires: a strategy to trace functional interactions in signaling and gene networks, Proceedings of the National Academy of Sciences 99 (20) (2002) 12841–12846.

[47] S. Boccaletti, V. Latora, Y. Moreno, M. Chavez, D.-U. Hwang, Complex networks: Structure and dynamics, Physics Reports 424 (4) (2006) 175–308.

[48] E. Candes, J. Romberg, l_1-magic : Recovery of sparse signals via convex programming @ONLINE (2005).
URL `http://users.ece.gatech.edu/~justin/l1magic/`

[49] I. Gurobi Optimization, Gurobi optimizer reference manual (2014).
URL `http://www.gurobi.com`

[50] M. A. Herman, T. Strohmer, General deviants: An analysis of perturbations in compressed sensing, IEEE Journal of Selected Topics in Signal Processing 4 (2) (2010) 342–349.

[51] R. A. Horn, C. R. Johnson, Matrix Analysis, Cambridge University Press, 1985.

[52] B. Barzel, A.-L. Barabási, Network link prediction by global silencing of indirect correlations, Nature Biotechnology 31 (8) (2013) 720–725.

[53] G. Karlebach, R. Shamir, Modelling and analysis of gene regulatory networks, Nature Reviews Molecular Cell Biology 9 (10) (2008) 770–780.

[54] U. Alon, An Introduction to Systems Biology: Design Principles of Biological Circuits, CRC press, 2006.

[55] H. Jeong, B. Tombor, R. Albert, Z. N. Oltvai, A.-L. Barabási, The large-scale organization of metabolic networks, Nature 407 (6804) (2000) 651–654.

[56] G. Stolovitzky, D. Monroe, A. Califano, Dialogue on reverse-engineering assessment and methods, Annals of the New York Academy of Sciences 1115 (1) (2007) 1–22.

[57] L. Muchnik, Complex networks package for matlab (version 1.6) (2013).
URL `http://www.levmuchnik.net/Content/Networks/Complex\NetworksPackage.html`

[58] P. O. Hoyer, Non-negative matrix factorization with sparseness constraints, The Journal of Machine Learning Research 5 (2004) 1457–1469.

[59] M. N. Arbeitman, E. E. Furlong, F. Imam, E. Johnson, B. H. Null, B. S. Baker, M. A. Krasnow, M. P. Scott, R. W. Davis, K. P. White, Gene expression during the life cycle of drosophila melanogaster, Science 297 (5590) (2002) 2270–2275.

[60] P. Pagel, S. Kovac, M. Oesterheld, B. Brauner, I. Dunger-Kaltenbach, G. Frishman, C. Montrone, P. Mark, V. Stümpflen, H.-W. Mewes, et al., The mips mammalian protein–protein interaction database, Bioinformatics 21 (6) (2005) 832–834.

[61] A.-L. Barabási, R. Albert, Emergence of scaling in random networks, science 286 (5439) (1999) 509–512.

[62] H.-S. J. Min, W. Beyeler, T. Brown, Y. J. Son, A. T. Jones, Toward modeling and simulation of critical national infrastructure interdependencies, IIE Transactions 39 (1) (2007) 57–71.

[63] R. Gao, L. Wang, R. Teti, D. Dornfeld, S. Kumara, M. Mori, M. Helu, Cloud-enabled prognosis for manufacturing, CIRP Annals-Manufacturing Technology 64 (2) (2015) 749–772.

[64] L. Atzori, A. Iera, G. Morabito, The internet of things: A survey, Computer Networks 54 (15) (2010) 2787–2805.

[65] N. Z. Gebraeel, M. A. Lawley, R. Li, J. K. Ryan, Residual-life distributions from component degradation signals: A bayesian approach, IIE Transactions 37 (6) (2005) 543–557.

[66] A. H. Elwany, N. Z. Gebraeel, Sensor-driven prognostic models for equipment replacement and spare parts inventory, IIE Transactions 40 (7) (2008) 629–639.

[67] W. H. Woodall, M. J. Zhao, K. Paynabar, R. Sparks, J. D. Wilson, An overview and perspective on social network monitoring, IISE Transactions (2016) 1–12.

[68] W. K. V. Chan, C. Hsu, When human networks collide: the degree distributions of hyper-networks, IIE Transactions 47 (9) (2015) 929–942.

[69] N. Zou, J. Li, Modeling and change detection of dynamic network data by a network state space model, IISE Transactions 49 (1) (2017) 45–57.

[70] Grand challenge.
URL http://www.debs2017.org/call-for-grand-challenge-sol\
utions/

[71] O. Devinsky, T. Spruill, D. Thurman, D. Friedman, Recognizing and preventing epilepsy-related mortality a call for action, Neurology 86 (8) (2016) 779–786.

[72] Gm reports q4 2014 net income of $1.1 billion.
URL http://media.gm.com/media/us/en/gm/news.detail.html\/content/Pages/news/emergency_news/2015/0204-4th-qtr-ear\nings.html

[73] A.-L. Barabási, R. Albert, Emergence of scaling in random networks, science 286 (5439) (1999) 509–512.

[74] A.-L. Barabasi, Z. N. Oltvai, Network biology: understanding the cell's functional organization, Nature Reviews Genetics 5 (2) (2004) 101–113.

[75] J. J. Pignatiello, G. C. Runger, Comparisons of multivariate CUSUM charts, Journal of Quality Technology 22 (3) (1990) 173–186.

[76] W. H. Woodall, M. M. Ncube, Multivariate CUSUM quality-control procedures, Technometrics 27 (3) (1985) 285–292.

[77] S. S. Prabhu, G. C. Runger, Designing a multivariate EWMA control chart, Journal of Quality Technology 29 (1) (1997) 8.

[78] H. G. Kramer, L. Schmid, EWMA charts for multivariate time series, Sequential Analysis 16 (2) (1997) 131–154.

[79] L. I. Kuncheva, W. J. Faithfull, Pca feature extraction for change detection in multi-dimensional unlabelled streaming data, in: IEEE 21st International Conference on Pattern Recognition (ICPR), 2012, pp. 1140–1143.

[80] B. R. Bakshi, Multiscale pca with application to multivariate statistical process monitoring, AIChE journal 44 (7) (1998) 1596–1610.

[81] M. Misra, H. H. Yue, S. J. Qin, C. Ling, Multivariate process monitoring and fault diagnosis by multi-scale pca, Computers & Chemical Engineering 26 (9) (2002) 1281–1293.

[82] A. Lung-Yut-Fong, C. Lévy-Leduc, O. Cappé, Robust changepoint detection based on multivariate rank statistics, in: IEEE International Conference on Acoustics, Speech and Signal Processing (ICASSP), IEEE, 2011, pp. 3608–3611.

[83] A. Kalgonda, S. Kulkarni, Multivariate quality control chart for autocorrelated processes, Journal of Applied Statistics 31 (3) (2004) 317–327.

[84] M. Bola, C. Gall, C. Moewes, A. Fedorov, H. Hinrichs, B. A. Sabel, Brain functional connectivity network breakdown and restoration in blindness, Neurology 83 (6) (2014) 542–551.

[85] M. Filippi, F. Agosta, Structural and functional network connectivity breakdown in alzheimer's disease studied with magnetic resonance imaging techniques, Journal of Alzheimer's Disease 24 (3) (2011) 455–474.

[86] I. Barnett, J.-P. Onnela, Change point detection in correlation networks, Scientific Reports 6.

[87] A. Aue, S. Hörmann, L. Horváth, M. Reimherr, et al., Break detection in the covariance structure of multivariate time series models, The Annals of Statistics 37 (6B) (2009) 4046–4087.

[88] L. Akoglu, H. Tong, D. Koutra, Graph based anomaly detection and description: a survey, Data Mining and Knowledge Discovery 29 (3) (2015) 626–688.

[89] P. Preuss, R. Puchstein, H. Dette, Detection of multiple structural breaks in multivariate time series, Journal of the American Statistical Association 110 (510) (2015) 654–668.

[90] M. Müller, G. Baier, A. Galka, U. Stephani, H. Muhle, Detection and characterization of changes of the correlation structure in multivariate time series, Physical Review E 71 (4) (2005) 046116.

[91] S. Ranshous, S. Shen, D. Koutra, S. Harenberg, C. Faloutsos, N. F. Samatova, Anomaly detection in dynamic networks: a survey, Wiley Interdisciplinary Reviews: Computational Statistics 7 (3) (2015) 223–247.

[92] A. De La Fuente, N. Bing, I. Hoeschele, P. Mendes, Discovery of meaningful associations in genomic data using partial correlation coefficients, Bioinformatics 20 (18) (2004) 3565–3574.

[93] A. K. Seth, A matlab toolbox for granger causal connectivity analysis, Journal of Neuroscience Methods 186 (2) (2010) 262–273.

[94] S. Basu, A. Shojaie, G. Michailidis, Network granger causality with inherent grouping structure, Journal of Machine Learning Research 16 (2015) 417–453.

[95] A. Bolstad, B. D. Van Veen, R. Nowak, Causal network inference via group sparse regularization, IEEE Transactions on Signal Processing 59 (6) (2011) 2628–2641.

[96] S. Haufe, G. Nolte, K.-R. Müller, N. Krämer, Sparse causal discovery in multivariate time series, JMLR W&CP 6 (2010) 97–106.

[97] A. C. Lozano, N. Abe, Y. Liu, S. Rosset, Grouped graphical granger modeling for gene expression regulatory networks discovery, Bioinformatics 25 (12) (2009) i110–i118.

[98] H. M. Tran, S. T. Bukkapatnam, Inferring sparse networks for noisy transient processes, Scientific reports 6 (2016) 21963.

[99] C. J. Honey, R. Kötter, M. Breakspear, O. Sporns, Network structure of cerebral cortex shapes functional connectivity on multiple time scales, Proceedings of the National Academy of Sciences 104 (24) (2007) 10240–10245.

[100] D. Centola, The spread of behavior in an online social network experiment, science 329 (5996) (2010) 1194–1197.

[101] M. M. Shafi, M. B. Westover, M. D. Fox, A. Pascual-Leone, Exploration and modulation of brain network interactions with noninvasive brain stimulation in combination with neuroimaging, European Journal of Neuroscience 35 (6) (2012) 805–825.

[102] H. S. Mayberg, A. M. Lozano, V. Voon, H. E. McNeely, D. Seminowicz, C. Hamani, J. M. Schwalb, S. H. Kennedy, Deep brain stimulation for treatment-resistant depression, Neuron 45 (5) (2005) 651–660.

[103] W. W. Lytton, Computer modelling of epilepsy, Nature Reviews Neuroscience 9 (8) (2008) 626–637.

[104] L. Zhao, K. Park, Y.-C. Lai, Attack vulnerability of scale-free networks due to cascading breakdown, Physical Review E 70 (3) (2004) 035101.

[105] R. Cohen, K. Erez, D. Ben-Avraham, S. Havlin, Breakdown of the internet under intentional attack, Physical Review Letters 86 (16) (2001) 3682.

[106] A. Shoeb, J. Guttag, Application of machine learning to epileptic seizure detection, in: Proceedings of the Twenty-Seventh International Conference on Machine Learning (ICML 2010), 2010.

[107] I. McCulloh, K. M. Carley, Social network change detection, Available at SSRN 2726799.

[108] C. E. Priebe, J. M. Conroy, D. J. Marchette, Y. Park, Scan statistics on enron graphs, Computational & Mathematical Organization Theory 11 (3) (2005) 229–247.

[109] Y. Park, C. E. Priebe, A. Youssef, Anomaly detection in time series of graphs using fusion of graph invariants, IEEE Journal of Selected Topics in Signal Processing 7 (1) (2013) 67–75.

[110] J. Neil, C. Hash, A. Brugh, M. Fisk, C. B. Storlie, Scan statistics for the online detection of locally anomalous subgraphs, Technometrics 55 (4) (2013) 403–414.

[111] D. Marchette, Scan statistics on graphs, Wiley Interdisciplinary Reviews: Computational Statistics 4 (5) (2012) 466–473.

[112] T. Idé, H. Kashima, Eigenspace-based anomaly detection in computer systems, in: Proceedings of the tenth ACM SIGKDD international conference on Knowledge discovery and data mining, ACM, 2004, pp. 440–449.

[113] M. D. Fox, M. E. Raichle, Spontaneous fluctuations in brain activity observed with functional magnetic resonance imaging, Nature Reviews Neuroscience 8 (9) (2007) 700–711.

[114] A. S. Pikovsky, J. Kurths, Coherence resonance in a noise-driven excitable system, Physical Review Letters 78 (5) (1997) 775.

[115] C. F. Cadieu, K. Koepsell, Phase coupling estimation from multivariate phase statistics, Neural Computation 22 (12) (2010) 3107–3126.

[116] T. Stankovski, V. Ticcinelli, P. V. McClintock, A. Stefanovska, Coupling functions in networks of oscillators, New Journal of Physics 17 (3) (2015) 035002.

[117] C. R. Rao, Linear statistical inference and its applications, Vol. 22, John Wiley & Sons, 2009.

[118] C. A. Tracy, H. Widom, Distribution functions for largest eigenvalues and their applications (2002).

[119] T. Tao, V. Vu, Random matrices: The distribution of the smallest singular values, Geometric And Functional Analysis 20 (1) (2010) 260–297.

[120] M. Chiani, M. Z. Win, A. Zanella, On the capacity of spatially correlated mimo rayleigh-fading channels, IEEE Transactions on Information Theory 49 (10) (2003) 2363–2371.

[121] A. Zanella, M. Chiani, M. Z. Win, On the marginal distribution of the eigenvalues of wishart matrices, IEEE Transactions on Communications 57 (4) (2009) 1050–1060.

[122] T. W. Anderson, An introduction to multivariate statistical analysis. 3rd ed. T.W. Anderson., Wiley series in probability and statistics, Hoboken, N.J. : Wiley-Interscience, 2003.

[123] Y. Kawahara, M. Sugiyama, Sequential change-point detection based on direct density-ratio estimation, Statistical Analysis and Data Mining 5 (2) (2012) 114–127.

[124] Epilepsy.
URL http://www.who.int/mediacentre/factsheets/fs999/en/

[125] S. Ramgopal, S. Thome-Souza, M. Jackson, N. E. Kadish, I. S. Fernández, J. Klehm, W. Bosl, C. Reinsberger, S. Schachter, T. Loddenkemper, Seizure detection, seizure prediction, and closed-loop warning systems in epilepsy, Epilepsy & Behavior 37 (2014) 291–307.

[126] Physionet database.

URL https://physionet.org/cgi-bin/atm/ATM

[127] G. P. Krishnan, G. Filatov, M. Bazhenov, Dynamics of high-frequency synchronization during seizures, Journal of Neurophysiology 109 (10) (2013) 2423–2437.

[128] K. Majumdar, P. D. Prasad, S. Verma, Synchronization implies seizure or seizure implies synchronization?, Brain Topography 27 (1) (2014) 112–122.

[129] S. P. Burns, S. Santaniello, R. B. Yaffe, C. C. Jouny, N. E. Crone, G. K. Bergey, W. S. Anderson, S. V. Sarma, Network dynamics of the brain and influence of the epileptic seizure onset zone, Proceedings of the National Academy of Sciences 111 (49) (2014) E5321–E5330.

[130] C. Donos, M. Dümpelmann, A. Schulze-Bonhage, Early seizure detection algorithm based on intracranial EEG and random forest classification, International Journal of Neural Systems 25 (05) (2015) 1550023.